
Efficient creation of multipartite entanglement for superconducting quantum computers

Johannes Ferber



München 2005

Efficient creation of multipartite entanglement for superconducting quantum computers

Johannes Ferber

Diplomarbeit
an der Fakultät für Physik
der Ludwig-Maximilians-Universität
München

vorgelegt von
Johannes Ferber
aus München

München, den 23.8.2005

Erstgutachter: PD Frank K. Wilhelm
Zweitgutachter: Prof. Dr. Harald Weinfurter

Contents

0	Overview	1
1	Introduction	3
1.1	Quantum computation	3
1.2	Implementation schemes	3
1.3	Superconducting qubits	4
1.4	Flux qubit	6
1.5	Decoherence	9
1.6	Coherent manipulation	9
1.7	Coupling of three qubits	10
1.8	Measurement	10
2	Coupling strength	11
2.1	Coupling via a common loop	11
2.2	Coupling via shared junctions–qubit triangle	16
2.3	Measurement design	19
3	Eigenstates of the system	21
3.1	Hamiltonian	21
3.2	No coupling	23
3.3	Weak antiferromagnetic coupling	25
3.4	Strong antiferromagnetic coupling	28
4	Preparing states in the degenerate subspaces	31
4.1	Quantizing the electromagnetic field and the interaction Hamiltonian	32
4.2	Preparing given states in the degenerate subspaces	33
5	Entanglement properties	39
5.1	Tripartite entanglement	40
5.2	Bell inequalities	44
5.3	Robustness to limited measurement fidelity	46
6	Pulse shaping	51
6.1	Laplace transform	52
6.2	LTI-Systems and transfer functions	52
6.3	Circuit synthesis theory	54

6.4	Approximation and results	57
	Conclusions	61
	Acknowledgments	63
A	Three-spin basis	65
B	Eigenenergies and eigenstates of the doublets	67
C	Structure of the eigenstates	69
D	Entanglement measures	73
	D.1 3-tangle	73
	D.2 Global entanglement	73
E	Driving propagators	75
F	Network synthesis	77
	F.1 Important time functions and their Laplace transforms	77
	F.2 Construction of networks	77
G	Publication	81
	List of Figures	87
	List of Tables	89
	Bibliography	91

Chapter 0

Overview

We propose a design based on flux qubits which is capable of creating tripartite entanglement in a natural, controllable and stable way.

In chapter 1, we describe the basic concepts of quantum computation and superconducting qubit devices. After having determined the character and the strength of the interaction between the flux qubits in our design in chapter 2, we concentrate on the properties of the eigenstates in chapter 3. Besides their natural benefits of easy preparation and stability to pure dephasing processes, the eigenstates are found to exhibit strong tripartite entanglement for an appropriate choice of parameters. Moreover, symmetries of the system lead to the formation of energetically degenerate subspaces that show a particular robustness. In chapter 4, we demonstrate the preparation of given, maximally entangled states in these subspaces by means of external microwave fields. In chapter 5, we cover the entanglement properties in more detail and identify both generic kinds of tripartite entanglement –the W type and the GHZ type entanglement– among the eigenstates. We furthermore discuss the violation of Bell inequalities in this system and present the impact of a limited measurement fidelity on the detection of entanglement and quantum nonlocality.

Chapter 6 finally features an approach to the shaping of short pulse sequences by filter networks of passive circuit elements. Its application is not limited to the presented flux-qubit design but also complies to the requirements of other solid state systems, as shown for the example of a quantum gate implementation in a system of two coupled charge qubits.

Chapter 1

Introduction

1.1 Quantum computation

Unlike classical computers, quantum computers store and process information represented by quantum variables. Typically, these variables consist of two-state quantum systems (although in principle, larger Hilbert spaces can be used), called quantum bits or *qubits*. Different from a classical bit, such a qubit can be prepared in a superposition of its basis states $|\psi\rangle = \alpha|0\rangle + \beta|1\rangle$. Moreover, interactions between qubits provide other intrinsic quantum mechanical resources unknown in classical physics and information technology such as entanglement. States of composite systems are called entangled if they are not separable into the states of the subsystems, such as $|\psi\rangle = (1/\sqrt{2})(|0\rangle|1\rangle + |1\rangle|0\rangle)$. Performing operations on these variables and making use of these resources while preserving the quantum character of the system allows for the solution of computational tasks practically infeasible for any conventional information technology. Various quantum algorithms have been developed that provide significant speedups over classical computation schemes [1, 2, 3, 4].

Crucial properties of a quantum computer are the capability to prepare the qubits in a desired initial state, the coherent manipulation of the states, and the possibility to couple qubits with each other, as well as read out their state at the end of the operation [5]. For the coherent manipulation, the qubits have to be isolated well enough to keep them free from interactions that induce noise and decoherence.

1.2 Implementation schemes

A number of possible two-state systems has been examined both theoretically and experimentally, and qubits have been physically implemented in a variety of systems as different as ions in an electromagnetic trap [6], nuclear spins, optical photon [7], and solid state realizations. All these efforts aim at developing a highly coherent and scalable set of quantum bits which can be isolated, controlled, coupled and measured. Realizations based on Nuclear Magnetic Resonance (NMR) [8, 9, 10] have been used to carry out small quantum algorithms [11], thereby proving the feasibility of a working quantum computer.

Although qubits based on NMR and other microscopic systems are the most advanced experimental realization available nowadays, it can hardly be imagined how to scale these systems up to large sizes, where quantum computers would beat conventional computers in real-world applications. Solid state implementations [12, 13] such as quantum dots or superconducting

qubits on the other hand side can –due to the available advanced lithographic methods developed in the context of conventional integrated electronics– be scaled up easily. Moreover, the layout of these system and the values of the parameters and couplings are determined by the designer. Along with this great flexibility, however, one has to deal with fabrication drawbacks, uncertain tolerances and the problem of decoherence. Whereas microscopic qubits such as ions are identical by nature, the manufacturing variability in artificial systems must be taken into account and being compensated for.

Here, we want to focus on superconducting designs.

1.3 Superconducting qubits

When quantizing the electromagnetic field, one finds that flux and charge are canonically conjugate variables [12]

$$[\hat{\Phi}, \hat{Q}] = i\hbar. \quad (1.1)$$

Both charge and flux quantization effects arise in superconducting circuits, both being capable of letting the system act as qubit. By tuning the system near a degeneracy point of the two basis states of the chosen degree of freedom (gate charge $n_g = 1/2$ for a charge qubit, external flux $\Phi_x = \Phi_0/2$ for a flux qubit), we can have the coupling mix the basis states and modify the energy of the eigenstates, Fig. 1.5. In the vicinity of these points the system effectively reduces to a two-state quantum system and quantum computation can be performed. The basis states in qubits based on the charge degree of freedom differ in the number of Cooper pairs on an island ($|n\rangle \equiv |0\rangle$, $|n+1\rangle \equiv |1\rangle$), while the states in flux qubits exhibit oppositely circulating supercurrents (and therefore two different fluxes).

Experimental investigations have demonstrated several quantum phenomena in both designs. On flux qubits, Rabi, Ramsey and echo-type sequences have been successfully performed [14, 15, 16], whereas in charge qubits even a CNOT gate has been realized [17, 18].

In the following, we describe the basic building blocks of superconducting qubits. Besides the fact that dissipation, meaning electrical resistance, should be avoided, and therefore use of superconductors is made, the phenomena associated with the quantum nature of superconductivity provide more interesting features for the design of such a qubit.

1.3.1 Josephson junction

A Josephson junction consists of two pieces of superconductor separated by a small insulating barrier. Cooper pairs on the superconducting electrodes on either side of the junction can tunnel through the barrier.

According to the first Josephson equation, the supercurrent through the barrier is given by [19]

$$I_S = I_C \sin \varphi, \quad (1.2)$$

where I_C is the critical current through the junction and φ the phase difference between the Cooper pair wavefunctions left and right

$$\Psi_L = |\Psi_1| e^{i\varphi_1}, \quad \Psi_R = |\Psi_2| e^{i\varphi_2}$$

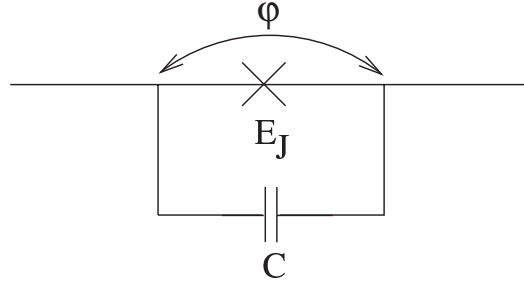


Figure 1.1: Equivalent circuit diagram of a Josephson junction. The junction itself is represented by a cross, associated with a Josephson energy E_J . The geometrical capacitance between the electrodes is given by C . φ is the phase difference across the junction.

with

$$\varphi = \varphi_1 - \varphi_2 . \quad (1.3)$$

If the current through the junction exceeds the critical current, a voltage V will drop across the junction and the phase will vary with time according to the second Josephson equation,

$$\dot{\varphi} = \frac{2eV}{\hbar} . \quad (1.4)$$

The dependence of the voltage on the time derivative of the phase (and hence the current) allows for associating a (nonlinear) inductance for the linear response of the junction, the Josephson inductance

$$L_J = \frac{\Phi_0}{2\pi I_C \cos \varphi} . \quad (1.5)$$

Using (1.2) and (1.4), one gets the free energy of the junction

$$F = \int V I_S dt = \text{const.} - E_J \cos \Delta\varphi \quad (1.6)$$

with the Josephson energy

$$E_J = \frac{\hbar I_C}{2e} . \quad (1.7)$$

Whereas the quadratic potentials provided by capacitances and inductances don't allow for the selective addressing of certain transitions due to their equal level spacing, this nonlinear potential will turn out to be a crucial ingredient for the construction of potentials beyond and gives rise to the desired double well constituting the qubit.

Since the junction geometry forms a parallel plate capacitor, there is, in addition to the junction itself, a capacitance C associated with the junction (see figure 1.1). The junction is therefore characterized by its Josephson energy E_J and its single-electron charging energy

$$E_C = \frac{e^2}{2C_J} . \quad (1.8)$$

1.3.2 Fluxoid quantization

If we put superconductors and Josephson junctions into a closed loop, the magnetic flux through the area enclosed by the loop is restricted. This is a result the single-valuedness of the Cooper pair wavefunction phase γ after one circulation around the loop,

$$\gamma = \sum_i \varphi_i + \frac{2\pi}{\Phi_0} \oint \mathbf{A} \cdot d\mathbf{s} . \quad (1.9)$$

Here, A denotes the vector potential of the magnetic field, the sum goes over all junctions, and the line integral goes once around the loop. By applying Stokes theorem we obtain

$$\sum_i \varphi_i + \frac{2\pi\Phi_{\text{tot}}}{\Phi_0} = 0 . \quad (1.10)$$

This relation is called fluxoid quantization [19]. The magnetic flux quantum in a superconductor reads

$$\Phi_0 = \frac{h}{2e} . \quad (1.11)$$

1.4 Flux qubit

We want to describe qubits based on the flux degree of freedom, called *flux qubits* or *persistent current qubits*.

In order to make persistent, dissipationless currents possible, we consider superconducting ring geometries. In addition, these rings shall be intersected by one or more Josephson junctions. The simplest design is a RF-SQUID, formed by a loop with one junction. Fluxoid quantization relates the phase across the junction to the magnetic flux enclosed by the loop, $\varphi = -\frac{2\pi\Phi_{\text{tot}}}{\Phi_0}$. The Hamiltonian includes the charging energy of the junction and its Josephson energy as well as the energy contained in the magnetic field created by the current in the loop [12],

$$\mathbf{H} = \frac{Q^2}{2C_J} - E_J \cos\left(2\pi\frac{\Phi_{\text{tot}}}{\Phi_0}\right) + \frac{(\Phi_{\text{tot}} - \Phi_x)^2}{2L} , \quad (1.12)$$

where L is the self-inductance of the loop, and Φ_x is the externally applied bias flux. For a bias $\Phi_x \approx (n + 1/2)\Phi_0$, the cosine potential and the quadratic potential of the third term can form a double well potential. The states in the bottoms of the two wells then correspond to two Φ expectation values $\Phi = n\Phi_0$ and $\Phi = (n + 1)\Phi_0$. The first term depends on the charge Q , the canonically conjugate variable of Φ and can therefore be considered to be the kinetic energy of the *particle* in the double well with mass C_J . However, in order to form a suitable double well potential, the Josephson energy E_J of the junction as well as the self inductance L of the loop have to be large. The first restriction requires a large junction with a large capacitance C_J , which suppresses tunneling. A high self inductance calls for large loops, making the system very sensitive to external noise.

These shortcomings can be overcome by using a smaller loop with three junctions [20], see figure 1.2 and 1.3.

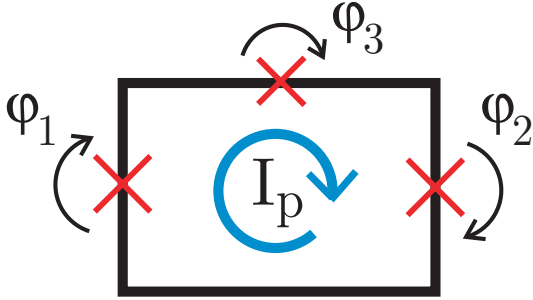


Figure 1.2: Circuit diagram of a three-junction flux qubit. Junction 3 is slightly smaller than the junctions 1 and 2.

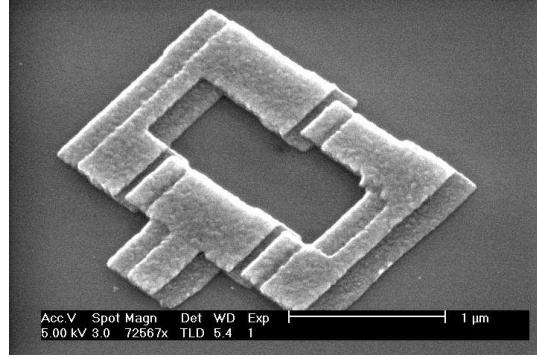


Figure 1.3: SEM picture of a three-junction flux qubit. The Josephson junctions are thin insulating oxide barriers between the superconducting electrodes [21].

The flux in this low-inductance circuit remains –as opposed to the design above– close to the externally applied field $\Phi_{\text{tot}} \approx \Phi_x$ and fluxoid quantization takes the form

$$\varphi_1 + \varphi_2 + \varphi_3 + \frac{2\pi\Phi_x}{\Phi_0} = 0. \quad (1.13)$$

Moreover, one of the junctions (here junction 3) is slightly smaller than the other two, $E_{J,3}/E_{J,2} = E_{J,3}/E_{J,1} = \alpha \approx 0.8$.

Writing down the Hamiltonian of the loop [20] yields

$$\mathbf{H} = \sum_{i=1}^3 \frac{Q_i^2}{2C_{J,i}} - E_J \left(\cos \varphi_1 + \cos \varphi_2 + \alpha \cos \left(\frac{2\pi\Phi}{\Phi_0} - \varphi_1 - \varphi_2 \right) \right) + \frac{(\Phi - \Phi_x)^2}{2L}. \quad (1.14)$$

Due to the small inductance of the loop, $\Phi \approx \Phi_x$ holds, and the term expressing the magnetic energy is small. The phase across junction 3 in (1.14) is expressed by the phases φ_1 and φ_2 of the two other junctions, leaving only these two phases as independent variables for the potential. If we plot the potential landscape of the Josephson energies spanned by these two variables along $\varphi_1 = \varphi_2 = \varphi$ (the direction connecting two nearest-neighbor minima in the periodic potential created by the cosine terms), we obtain a double well potential for the applied flux close to half a flux quantum and $\alpha \approx 0.8$, see figure 1.4.

At low temperatures, only the lowest states in the two wells contribute, making sure that there is only one bound state in each well. The states in the two wells correspond to persistent currents running clockwise and counterclockwise through the loop.

The phase configuration in these minima can be derived from the classical stability diagram (minimum energy phase configurations, $\frac{\partial U}{\partial \varphi_1} = 0$, $\frac{\partial U}{\partial \varphi_2} = 0$ and $\varphi_1 = \varphi_2 = \pm \varphi^*$) for $\frac{\Phi_x}{\Phi_0} = \frac{1}{2}$

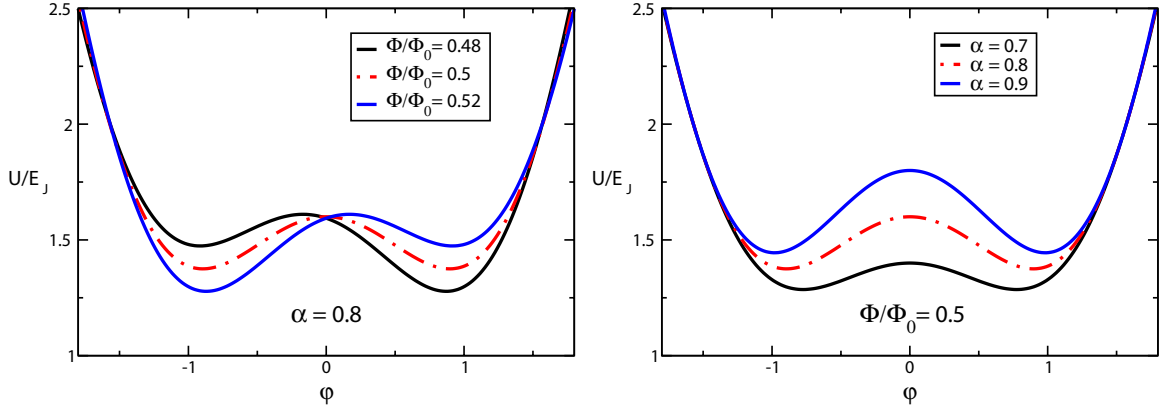


Figure 1.4: Energy landscape of a three junction qubit. Left figure: The energy bias ϵ can be tuned by the applied magnetic flux. With the definition of the persistent current (1.16), it reads: $\epsilon = 2 I_p (\Phi - \Phi_0/2)$. Right figure: The tunnel matrix element is determined by the barrier between the two classical minima, which depends on α . One can see that a smaller α lowers the barrier and increases the tunneling.

[22],

$$\cos \varphi^* = \frac{1}{2\alpha}. \quad (1.15)$$

The persistent current is the current flowing in this classical minimum,

$$I_p = I_C \sin \varphi^* = I_C \sqrt{1 - \frac{1}{4\alpha^2}}. \quad (1.16)$$

In the classical limit, for large E_J and vanishing E_C of the junctions, tunneling would be suppressed, establishing these two states with well defined phase (and therefore well defined current and flux) as eigenstates of the system, justifying the name *flux qubit*. For realistic scenarios of E_J being larger than E_C , but both being within few orders of magnitude, tunneling is driven by the capacitive quantum fluctuations, and the eigenstates of the system are superpositions of the two flux states, making the system act as qubit. Hence, the reduced Hamiltonian of this two-state (or pseudo-spin) system can be written in standard representation,

$$\mathbf{H}_{\text{eff}} = -\frac{1}{2} \epsilon \hat{\sigma}_z - \frac{1}{2} \Delta \hat{\sigma}_x, \quad (1.17)$$

where $\hat{\sigma}_z$ and $\hat{\sigma}_x$ are the Pauli matrices. The diagonal term containing ϵ is the energy bias, i.e. the energy asymmetry between the two wells, and Δ is the tunnel matrix element. The eigenenergies of this Hamiltonian are $\pm \sqrt{\epsilon^2 + \Delta^2}/2$, the resulting anticrossing is depicted in figure 1.5.

As mentioned above, several quantum phenomena have been observed in flux qubits, including superposition of states [14] and coherent Rabi oscillations [15, 16]. This justifies the two-state approximation used above.

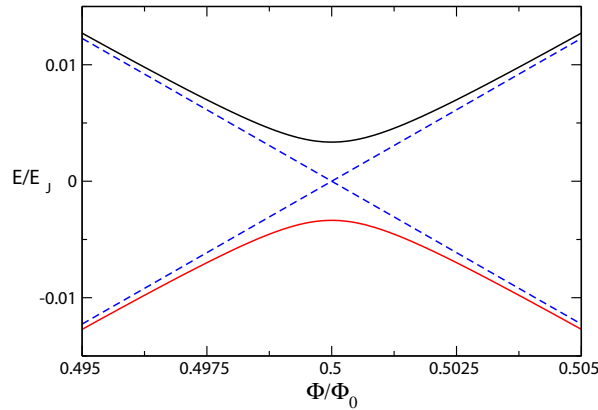


Figure 1.5: The energies of the two localized persistent-current states are indicated with the dashed lines. At the degeneracy point $\Phi = \Phi_0/2$, the quantum levels (solid lines) are symmetric and antisymmetric superpositions of the two persistent-current states and an anticrossing occurs. The expectation value of the current in the loop is zero at the degeneracy point and approaches the persistent current $\pm I_p$ far away from the degeneracy point.

1.5 Decoherence

Among the design requirements for a quantum computer, the sufficient long timescale over which the quantum coherence needs to be kept, is particularly hard to meet for solid state systems. The relatively strong coupling of the qubits to the many fluctuating, uncontrolled environmental degrees of freedom causes quick decoherence, i.e. dephasing and relaxation.

Dephasing describes the process of vanishing correlations between the states, ending up in a statistical mixture as opposed to a quantum mechanical superposition. The correlations are given by the off-diagonal terms of the density operator. The dephasing time is the characteristic time on which these terms turn to zero. In the flux qubit design, among other sources, flux noise causes the energy splitting of the qubit to fluctuate, resulting in dephasing.

Relaxation is the process of approaching the thermal equilibrium. The relaxation time is the characteristic time on which the diagonal elements of the density matrix go towards the values given by the Boltzmann factors.

Recent measurements on relaxation and dephasing times in flux qubits have yielded timescales of approximately 100 ns for both processes [23].

The coupling of the system to a dissipative environment and the resulting decoherence effects are often modelled by the Spin-Boson model [24]. Here, the qubits are described by spin-1/2 particles and the environment is taken as a bath of harmonic oscillators. This way, all Gaussian noise sources can be reproduced by appropriately chosen spectral functions. On the other hand, non-Gaussian noise such as $1/f$ noise can not be treated by this method.

1.6 Coherent manipulation

Quantum operations in solid state devices are performed by applying electromagnetic fields. To implement given operations, two components of the effective magnetic field need to be controlled. However, for flux qubits, usually only control over the energy bias ϵ can be gained

by means of an external magnetic field, whereas the tunnel element Δ remains fixed. A possible solution is *resonant driving*, known from NMR [8]. One induces Rabi oscillations between different states of the qubit by resonant pulses, i.e. AC pulses with frequency close to the qubit's level spacing, and lets the system evolve at this degeneracy point for a certain time. By this, arbitrary one-qubit operations are possible, but the evolution under the internal system Hamiltonian puts physical limits on the minimum time required to prepare the target state.

1.7 Coupling of three qubits

A two-qubit operation is in general induced by turning on the corresponding coupling between the qubits. For flux qubits placed close to each other, the natural interaction is mediated by the magnetic fluxes and always turned on, however, switchable [20] or even tunable [25] coupling schemes based on SQUIDs have been proposed. But even for fixed coupling schemes as the ones presented in the following, full control can be gained and all quantum gates can be realized. However, we want to concentrate on the possibility of creating tripartite entanglement. It will be shown that the coupling schemes proposed in chapter 2 give rise to pairwise coupling between the qubits of the type $\hat{\sigma}_z^{(i)} \otimes \hat{\sigma}_z^{(j)}$. We will see that this can lead to superpositions of macroscopically distinct states. Besides the fundamental interest in this kind of macroscopic quantum behavior, these states will turn out to have interesting entanglement properties.

1.8 Measurement

Besides the controlled manipulations of the qubits, measurements have to be performed to read out the final state of the system. The ideal projective measurement with the collapse of the wavefunction is just an approximation of this process, since the measurement device is a quantum system by its own, coupled to the measured system. In case of flux qubits, the measurement devices are DC-SQUIDs [20, 21, 26], the coupling is given by the mutual inductance between the qubit and the DC-SQUID. By sending a current through the SQUID one can determine the switching current, i.e. the critical current where the SQUID switches to the finite voltage state. This is a measure for the flux enclosed by the SQUID, and thereby for the state of the qubit. However, the flux fluctuations produced by the SQUID current itself cause decoherence in the qubit. Moreover, this switching is a statistical process, giving a spread in the switching currents. No perfect correlation of the measurement result with the state of the qubit can be achieved, in contrast to the ideal von Neumann measurement. Recently developed measurement schemes like dispersive readout [27] or the non-dissipative measurement of the change in the Josephson inductance of the SQUID [28, 29] in contrast to the dissipative switching scheme outlined above can avoid some of these limitations. We will discuss this in more detail in section 2.3, where we propose a measurement geometry for our three-qubit design.

Chapter 2

Coupling strength

Two designs for a coupled 3-qubit system with two different coupling schemes have been investigated, namely inductive coupling via mutually induced fluxes and coupling via the Josephson inductances of shared junctions. It will turn out that of both these mechanisms can be treated by introducing extra phases, which incorporate the couplings and add up linearly to the total coupling strength.

2.1 Coupling via a common loop

The first design is shown in figure 2.1. To achieve a reasonable interaction via the magnetic flux, the qubits have –due to their small mutual inductances– to be put very closely to each other. The dashed line denotes a flux transformer consisting of a SQUID loop around the three qubits to further increase the small coupling. The flux transformer encloses the qubits in a way such as to maximize the inductance between transformer and qubit and to obtain a coupling as symmetrical as possible.

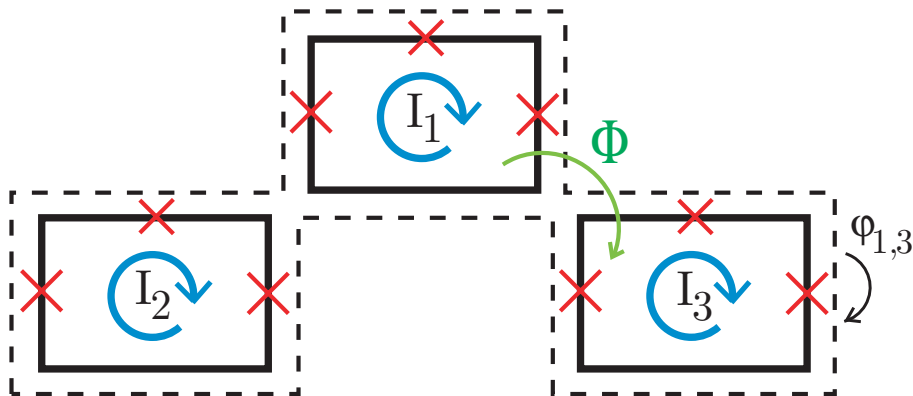


Figure 2.1: Three qubits, enclosed by a common SQUID-loop (dashed line). Crosses represent the Josephson junctions. The circle arrows in the qubits define the directions of the currents, the semicircle arrow indicates a magnetic flux line, causing a coupling between the qubits via their geometrical mutual inductance. In addition, there is an indirect inductive coupling between the qubits mediated by the SQUID loop.

To calculate the coupling strength one has to take into account two terms that contribute to the total potential energy. The first one is the sum of the Josephson energies in the junctions of the qubits. This energy is modified by the coupling via a change in the fluxoid quantization (1.10) due to the additional fluxes. This induces an extra phase bias and thus the energy of the junctions. We will calculate this contribution in the following.

2.1.1 Josephson energy due to phase bias

The total Josephson energy in the junctions of all qubits is given by

$$E_{\text{Jos},Q} = -E_{J,Q} \sum_{i=1}^3 (\cos \varphi_{1,i} + \cos \varphi_{2,i} + \alpha \cos \varphi_{3,i}) . \quad (2.1)$$

Applying the fluxoid quantization for the i -th qubit gives

$$\varphi_{1,i} + \varphi_{2,i} + \varphi_{3,i} + \frac{2\pi\Phi_{\text{tot},i}}{\Phi_0} = 0 . \quad (2.2)$$

The total magnetic flux $\Phi_{\text{tot},i}$ through the i -th qubit is a sum of the externally applied flux $\Phi_{x,i}$, the self produced flux, the fluxes induced by the other qubits and the flux induced by the transformer,

$$\Phi_{\text{tot},i} = \Phi_{x,i} + L_i I_{p,i} - \sum_{j \neq i} M_{ij} I_{p,j} + M_{Ti} I_T . \quad (2.3)$$

Here L_i denotes the self inductance of the i -th qubit, $M_{ij} = M_{ji}$ with $i \neq j$ the mutual inductance between the i -th and the j -th Qubit and M_{Ti} the mutual inductance between the transformer and the qubit. The negative sign in front of the qubit-qubit interaction term reflects the fact that the mutual inductance between the qubits is negative, as a flux in one qubit reduces the fluxes in the other ones (cp. figure 2.1).

Henceforth, we will refer to the persistent current $I_{c,i}$ simply as I_i . Since there are no other currents involved in the calculation, this should not provoke misunderstandings.

The flux Φ_T through the transformer reads

$$\Phi_T = L_T I_T + \sum_{j=1}^3 M_{Tj} I_j \quad (2.4)$$

with L_T being the self inductance of the transformer and I_T the current flowing through it. The screening flux in the transformer opposes the magnetic field, effectively cancelling out the net flux,

$$\Phi_T = 0 . \quad (2.5)$$

Therefore:

$$I_T = -\frac{1}{L_T} \sum_{j=1}^3 M_{Tj} I_j . \quad (2.6)$$

For convenience purposes and for later generalizing the results, we introduce an extra phase,

$$\phi_i = \frac{2\pi}{\Phi_0} \left(L_i I_i - \sum_{j \neq i} M_{ij} I_j - \frac{1}{L_T} M_{Ti} \sum_{j=1}^3 M_{Tj} I_j \right). \quad (2.7)$$

This phase ϕ_i incorporates the coupling effects and enters into the fluxoid quantization (2.2),

$$\varphi_{1,i} + \varphi_{2,i} + \varphi_{3,i} + \phi_i + \frac{2\pi\Phi_{x,i}}{\Phi_0} = 0. \quad (2.8)$$

Since the fluxes induced by the other parts of the system are small compared to the flux quantum, ϕ_i can be considered to be small as well ($\phi_i \approx 7 \cdot 10^{-4}$).

Expressing the phase across the smaller junction in terms of the other phases gives

$$\begin{aligned} \alpha \cos \varphi_{3,i} &= \alpha \cos \left(\frac{2\pi\Phi_{x,i}}{\Phi_0} + \varphi_{1,i} + \varphi_{2,i} + \phi_i \right) = \\ &= \alpha \cos \left(\frac{2\pi\Phi_{x,i}}{\Phi_0} + \varphi_{1,i} + \varphi_{2,i} \right) \cdot \cos \phi_i - \\ &\quad - \alpha \sin \left(\frac{2\pi\Phi_{x,i}}{\Phi_0} + \varphi_{1,i} + \varphi_{2,i} \right) \cdot \sin \phi_i. \end{aligned} \quad (2.9)$$

The discussion of the individual terms yields:

- $\cos \phi_i \approx 1$, since ϕ_i is small.
- $\sin \left(\frac{2\pi\Phi_{x,i}}{\Phi_0} + \varphi_{1,i} + \varphi_{2,i} \right) \approx \sin (\pi + \varphi_{1,i} + \varphi_{2,i}) = -\sin (\varphi_{1,i} + \varphi_{2,i})$.

The minima of the potential landscape of a single qubit are located at $\varphi_1 = \varphi_2 = \pm\varphi^*$ where $\cos \varphi^* = \frac{1}{2\alpha}$ [22].

Therefore: $-\sin (\varphi_{1,i} + \varphi_{2,i}) \approx -2 \sin \varphi^* \cos \varphi^* = -\frac{1}{\alpha} \frac{I_i}{I_{C,Q}}$.

- $\sin \phi_i \approx \phi_i$.

$$\alpha \cos \varphi_{3,i} = \alpha \cos \left(\frac{2\pi\Phi_{x,i}}{\Phi_0} + \varphi_{1,i} + \varphi_{2,i} \right) + \frac{I_i}{I_{C,Q}} \phi_i. \quad (2.10)$$

With the definitions of ϕ_i (2.7), $E_{\text{Jos},Q}$ (2.1) and Φ_0 (1.11), we arrive at

$$\begin{aligned} E_{\text{Jos},Q} &= \sum_{i=1}^3 E_{\text{Jos,uncp}} - \frac{E_{J,Q}}{I_{C,Q}} \sum_{i=1}^3 I_i \phi_i = \\ &= \sum_{i=1}^3 E_{\text{Jos,uncp}} - \sum_{i=1}^3 L_i I_i^2 + \sum_{i=1}^3 \sum_{j \neq i} M_{ij} I_i I_j + \frac{1}{L_T} \sum_{ij} M_{Ti} M_{Tj} I_i I_j. \end{aligned} \quad (2.11)$$

for the Josephson energies of the qubit junctions. Here $E_{\text{Jos,uncp}}$ denotes the Josephson junction energies of a single qubit without couplings,

$$E_{\text{Jos,uncp}} = -E_{J,Q} \sum_{i=1}^3 \left(\cos \varphi_{1,i} + \cos \varphi_{2,i} + \alpha \cos \left(\frac{2\pi\Phi_{x,i}}{\Phi_0} + \varphi_{1,i} + \varphi_{2,i} \right) \right). \quad (2.12)$$

We now separate the sums into single qubit energies and interaction terms. Note that

$$\sum_{i=1}^3 \sum_{j \neq i} c_{ij} = 2 \sum_{i=1}^3 \sum_{j>i} c_{ij}, \text{ if } c_{ij} = c_{ji} \quad \forall i, j.$$

$$E_{\text{Jos,Q}} = \sum_{i=1}^3 E_{\text{Jos,uncp}} + \sum_{i=1}^3 \left(\frac{M_{Ti}^2}{L_T} - L_i \right) I_i^2 + 2 \sum_{i=1}^3 \sum_{j>i} \left(M_{ij} + \frac{M_{Ti} M_{Tj}}{L_T} \right) I_i I_j. \quad (2.13)$$

This coupling, expressed by the last term in (2.13), is antiferromagnetic, giving an energy advantage for an antiparallel configuration of the currents.

2.1.2 Energy stored in the magnetic field

The second contribution is the energy stored in the joint magnetic field [30]. It is given by

$$E_{\text{mag}} = \frac{1}{2} \sum_{i=1}^3 L_i I_i^2 - \sum_{i=1}^3 \sum_{j>i} M_{ij} I_i I_j + \sum_{i=1}^3 M_{Ti} I_T I_i + \frac{1}{2} L_T I_T^2. \quad (2.14)$$

Insert (2.6) and split again into single qubit terms and interactions:

$$\begin{aligned} E_{\text{mag}} &= \frac{1}{2} \sum_{i=1}^3 L_i I_i^2 - \sum_{i=1}^3 \sum_{j>i} M_{ij} I_i I_j - \frac{1}{2} \frac{1}{L_T} \sum_{ij} M_{Ti} M_{Tj} I_i I_j = \\ &= -\frac{1}{2} \sum_{i=1}^3 \left(\frac{M_{Ti}^2}{L_T} - L_i \right) I_i^2 - \sum_{i=1}^3 \sum_{j>i} \left(M_{ij} + \frac{M_{Ti} M_{Tj}}{L_T} \right) I_i I_j \end{aligned} \quad (2.15)$$

We see that this contribution gives a ferromagnetic coupling with half the strength of the Josephson term. The sign of the interaction can be understood by looking at the two parts of the expression $M_{ij} + \frac{M_{Ti} M_{Tj}}{L_T}$. First, the direct qubit-qubit interaction, represented by M_{ij} , has to be ferromagnetic owing to the negative mutual inductance between the qubits. Comparing the direction of the flux line in Fig. 2.1, one recognizes that for a parallel alignment of the magnetic fluxes, each qubit reduces the flux in the other qubits and thereby the energy of the joint magnetic field, yielding an energy advantage for a parallel alignment. Second, the screening of the magnetic flux in the transformer, as described above, gives rise to a second ferromagnetic contribution. The two mutual inductances showing up in the transformer coupling part $\frac{1}{L_T} M_{Ti} M_{Tj}$ can be considered as the links in the interaction chain first qubit \leftrightarrow flux transformer \leftrightarrow second qubit.

2.1.3 Coupling strength

Adding up the two contributions gives

$$\begin{aligned}
 E &= E_{\text{Jos},Q} + E_{\text{mag}} = \\
 &= \sum_{i=1}^3 E_{\text{Jos},\text{uncp}} + \frac{1}{2} \sum_{i=1}^3 \left(\underbrace{\frac{M_{Ti}^2}{L_T} - L_i}_{L_i'} \right) I_i^2 + \sum_{i=1}^3 \sum_{j>i} \left(\underbrace{M_{ij} + \frac{M_{Ti} M_{Tj}}{L_T}}_{K_{ij}} \right) I_i I_j \quad (2.16)
 \end{aligned}$$

L_i' is the modified self inductance of the i -th qubit. As pointed out in the introduction, the double well potential is predominantly shaped by the Josephson energies. We can therefore neglect the modified self inductance when applying the two-state approximation.

K_{ij} is the coupling coefficient between the i -th and the j -th qubit and describes an antiferromagnetic coupling. This can be considered an effect of Lenz' rule imposed by the perfect screening of the fluxes in the qubits. Table 2.1 shows numerical values for the inductances obtained with **FastHenry**, an inductance analysis program [31].

$L_1 = L_2 = L_3$	2.39 pH
L_T	15 pH
$M_{12} = M_{13}$	0.014 pH
M_{23}	0.0039 pH
M_{T1}	0.68 pH
$M_{T2} = M_{T3}$	0.73 pH
$L_1' = L_2' = L_3'$	-2.36 pH
$K_{12} = K_{13}$	0.047 pH
K_{23}	0.039 pH

Table 2.1: Mutual inductances for the common-loop-design, based on the following geometrical sizes: qubits $1 \mu\text{m}$ by $1.51 \mu\text{m}$ with lines of 100 nm height and 300 nm width, distance qubit–loop 600 nm .

One finds that the coupling due to the flux transformer ($K_{ij} - M_{ij}$) gives a significantly larger coupling than the direct geometric inductance between the qubits (M_{ij}). Moreover, it turns out that the strong asymmetry arising for direct coupling between the qubit $1 \leftrightarrow$ qubit $2, 3$ (0.014 pH) and qubit $2 \leftrightarrow$ qubit 3 (0.0039 pH) is decreased because the mutual inductance between qubits $2, 3$ and the flux transformer (0.73 pH) is stronger than between qubit 1 and the transformer (0.68 pH). We therefore can assume an equal coupling constant between all three pairs of qubits,

$$K_{ij} \approx K \quad \forall i \neq j. \quad (2.17)$$

Furthermore, the persistent currents of all qubits are ideally identical, $I_1 = I_2 = I_3 = I_p \approx 300 \text{ nA}$ and the coupling C_{ij} reads

$$C_{ij} = K_{ij} I_i I_j \approx K I_p^2 = C \approx 5.8 \text{ MHz}. \quad (2.18)$$

2.2 Coupling via shared junctions—qubit triangle

In this section the design shown in figure 2.2 will be discussed. The three qubits are pairwise sharing a common line with an extra Josephson junction inserted in it. Every pair of qubits sends its currents through the joint junction and therefore imposes a phase $\varphi_{i,S}$ across it.

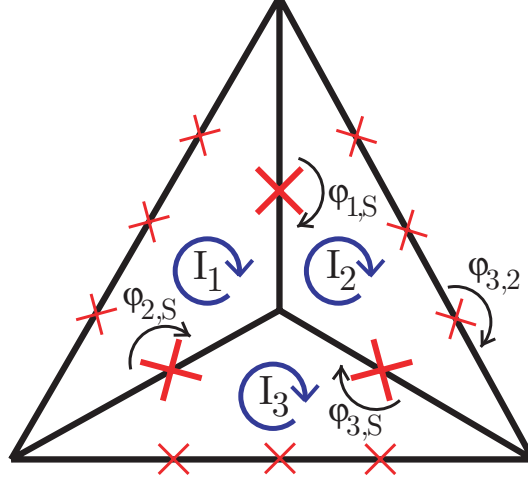


Figure 2.2: The design of the flux qubit triangle. The three qubits are formed by the three small isosceles triangles, the round arrows in the qubits defining the directions of the currents. Small crosses represent the Josephson junctions in the individual qubits, large crosses the coupling junctions (big Josephson energy—small Josephson inductance).

As in section 2.1, two energies are associated with this coupling. The first one is again the sum of the Josephson energies in the qubit junctions. The phases across the shared junctions influence fluxoid quantization in the individual qubits and thus change the Josephson energies of their junctions. We will first calculate this effect.

2.2.1 Josephson energy due to phase bias

The total Josephson energies in the qubit junctions is again given by

$$E_{\text{Jos},Q} = -E_{J,Q} \sum_{i=1}^3 (\cos \varphi_{1,i} + \cos \varphi_{2,i} + \alpha \cos \varphi_{3,i}) . \quad (2.19)$$

When applying fluxoid quantization, we take the additional phases $\varphi_{i,S}$ of the shared junctions into account (here exemplarily for qubit 1, in analogy for qubits 2 and 3):

$$\varphi_{11} + \varphi_{12} + \varphi_{13} + \varphi_{1,S} - \varphi_{2,S} + \frac{2\pi\Phi_{\text{tot},1}}{\Phi_0} = 0 \quad (2.20)$$

The coupling junctions are large compared to the qubit junctions and their critical currents are far above the persistent currents in the qubits. Hence, their phases are small and behave nearly classical (the fluctuations in the phases are small, and phases can therefore be expressed in terms of the classical flowing currents). In this regime, the nonlinear inductance discussed in chapter 1 can be assumed to be linear, having the same effect as the mutual inductances in

section 2.1. Moreover, we assume the critical currents of these junctions to be equal (which can be achieved in an actual experiment, because critical currents can be tuned very accurately [16]). According to the directions of currents (cp. Figure 2.2), we get

$$\varphi_{1,S} = \arcsin \frac{I_1 - I_2}{I_{C,S}} \approx \frac{I_1 - I_2}{I_{C,S}}, \quad (2.21)$$

$$\varphi_{2,S} \approx \frac{I_3 - I_1}{I_{C,S}}, \quad (2.22)$$

$$\varphi_{3,S} \approx \frac{I_2 - I_3}{I_{C,S}}. \quad (2.23)$$

Adding up the phases for the fluxoid quantization rules (2.20) in each qubit consistently, we again define extra coupling phases (cp. (2.7)), namely

$$\phi_1 = \varphi_{1,S} - \varphi_{2,S} \approx \frac{2I_1 - I_2 - I_3}{I_{C,S}}, \quad (2.24)$$

$$\phi_2 = \varphi_{3,S} - \varphi_{1,S} \approx \frac{2I_2 - I_1 - I_3}{I_{C,S}}, \quad (2.25)$$

$$\phi_3 = \varphi_{2,S} - \varphi_{3,S} \approx \frac{2I_3 - I_1 - I_2}{I_{C,S}}. \quad (2.26)$$

Moreover, the coupling mediated by the geometrical inductance will turn out to be much smaller than the one due to the shared junctions. Therefore, we neglect the additional fluxes induced by the other qubits and set $\Phi_{\text{tot},i} \approx \Phi_{x,i}$.

The rewritten fluxoid quantization

$$\varphi_{1,i} + \varphi_{2,i} + \varphi_{3,i} + \phi_i + \frac{2\pi\Phi_{x,i}}{\Phi_0} = 0 \quad (2.27)$$

then looks the same as (2.8).

Applying the same reasoning as in section 2.1.1, we get in analogy to (2.11)

$$E_{\text{Jos},Q} = \sum_{i=1}^3 E_{\text{Jos},\text{uncp}} - \frac{E_J}{I_{C,Q}} \sum_{i=1}^3 I_i \phi_i. \quad (2.28)$$

Putting in (2.24),(2.25) and (2.26) and using (1.7) and (1.11) yields

$$E_{\text{Jos},Q} = \sum_{i=1}^3 E_{\text{Jos},\text{uncp}} + \frac{\Phi_0}{2\pi I_{C,S}} 2 \left(- \sum_{i=1}^3 I_i^2 + \sum_{i=1}^3 \sum_{j>i} I_i I_j \right). \quad (2.29)$$

We can express this in terms of the Josephson inductance of the shared junctions $L_{J,S}$ (1.5),

$$L_{J,S} \approx \frac{\Phi_0}{2\pi I_{C,S}}, \quad (2.30)$$

$$E_{\text{Jos},Q} = \sum_{i=1}^3 E_{\text{Jos},\text{uncp}} - 2 L_{J,S} \sum_{i=1}^3 I_i^2 + 2 L_{J,S} \sum_{i=1}^3 \sum_{j>i} I_i I_j . \quad (2.31)$$

We find that the coupling due to the phase bias is antiferromagnetic, as in section 2.1.1. The Josephson inductance of the shared junctions here plays the role of the mutual inductance mediating the interaction between the qubits. It depends on the size of the junctions, with a bigger junction resulting in a smaller inductance and a smaller coupling. This can be understood by considering that the same current imposes a smaller phase difference across a larger junction modifying the fluxoid quantization less violently.

2.2.2 Josephson energy of the shared junctions

The second energy associated with the inserted junctions is their own Josephson energy. We expand and get

$$E_{\text{Jos},S} = -E_{J,S} \sum_{i=1}^3 \cos \varphi_{i,S} \approx -E_{J,S} \sum_{i=1}^3 \left(1 - \frac{\varphi_{i,S}^2}{2} \right) . \quad (2.32)$$

By putting in (2.21), (2.22), (2.23) and using the definition of the Josephson inductance (2.30), we obtain

$$E_{\text{Jos},S} = -3 E_{J,S} + L_{J,S} \sum_{i=1}^3 I_i^2 - L_{J,S} \sum_{i=1}^3 \sum_{j>i} I_i I_j . \quad (2.33)$$

2.2.3 Coupling strength

The total potential energy reads

$$\begin{aligned} E &= E_{\text{Jos},Q} + E_{\text{Jos},S} = \\ &= \sum_{i=1}^3 E_{\text{Jos},\text{uncp}} - 3 E_{J,S} - L_{J,S} \sum_{i=1}^3 I_i^2 + L_{J,S} \sum_{i=1}^3 \sum_{j>i} I_i I_j . \end{aligned} \quad (2.34)$$

Therefore:

$$K_{ij} = K = L_{J,S} \quad \forall i \neq j \quad (2.35)$$

Using the same values as in section 2.1.3, $I_1 = I_2 = I_3 = I_p \approx 300$ nA, we arrive at the coupling

$$C_{ij} = K_{ij} I_i I_j \approx L_{J,S} I_p^2 = C . \quad (2.36)$$

This type of coupling allows for great flexibility, a typical and achievable coupling strength for later discussions is $C=700$ MHz (corresponding to $L_{J,S} \approx 5$ pH).

2.2.4 Smaller contributions

In addition to the strong coupling provided by the junctions, there are still smaller contributions from the geometrical inductance (as described in section 2.1) and the kinetic inductance of the shared lines [16]. All these coupling add up linearly to the total coupling

$$C_{\text{tot}} = \sum_n C_n. \quad (2.37)$$

In table 2.2, the mutual geometrical inductances as calculated by `FastHenry` and the resulting coupling are listed (cp. table 2.1).

$L_1 = L_2 = L_3$	2.8 pH
$M_{12} = M_{13} = M_{23}$	-0.48 pH
C	65 MHz

Table 2.2: Mutual geometrical inductances for the qubit triangle, based on the following geometrical sizes: short sides of the qubit triangles $2 \mu\text{m}$, all lines 100 nm thick and 300 nm wide.

The mutual geometrical inductances between the qubits as listed in table 2.2 are due to the close arrangement and the pairwise shared lines much stronger than in the case of the common loop design (table 2.1). Nevertheless, the coupling mediated by the geometrical inductances is much weaker than the Josephson coupling.

2.3 Measurement design

Fig. 2.3 shows a possible design for the readout of the individual qubits. Three SQUIDs are attached to the three sides of the triangle and coupled to it by their mutual inductance.

The quantum state can be read out by measuring the generated magnetic flux, as the critical supercurrent of the SQUIDs depends on the flux piercing the SQUID loops [26]. By ramping the current through the SQUID up to the critical current one can determine the point where switching to the finite voltage state takes place. However, in the voltage state, quasiparticles are generated that later recombine with a burst of energy, and high frequency radiation is emitted towards the circuit. To circumvent these drawbacks, one can indirectly obtain the critical current by determining the Josephson inductance. This is based on the property of a SQUID to behave as an inductor, with a Josephson inductance that depends on the magnetic flux enclosed in the loop. The value of the Josephson inductance can be determined by measuring the impedance of the SQUID. This way, very high measurement fidelities of 90% could be observed experimentally [28, 29]. In order to achieve a high measurement fidelity, the mutual inductance between SQUID and qubit needs to be large [29], leading to the common design, where the the qubit is enclosed in the SQUID. A placement besides the qubits as in our design decreases the coupling and could partially be compensated for by larger structures.

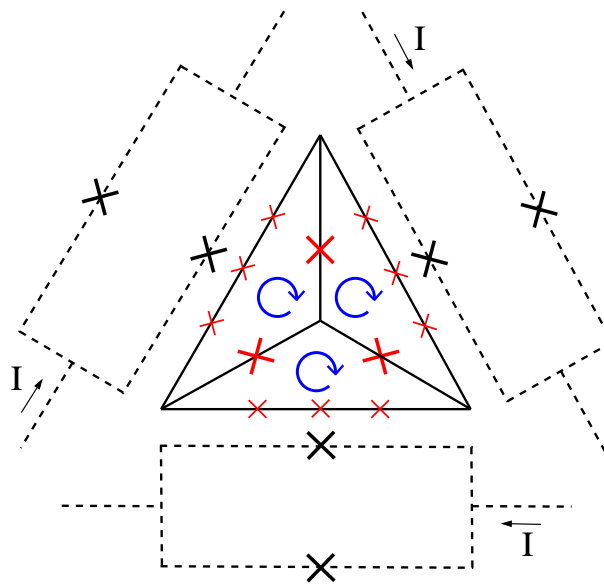


Figure 2.3: Possible readout design with three SQUIDs. The SQUIDs are coupled to the triangle by their mutual inductances.

Chapter 3

Eigenstates of the system

We aim for preparing tripartite entangled states in a preferably easy and stable way. Both demands are naturally met by the eigenstates of a system, as eigenstates are easy to prepare by π -pulse driving on the one hand side and stable to pure dephasing processes on the other hand side. Since the dephasing time T_2 is usually the shorter timescale compared to the relaxation time T_1 [23], this is particularly desirable. We start with writing down the Hamiltonian in an appropriate basis, taking into account the coupling derived in chapter 2 and continue with investigating the eigenenergies and eigenstates for different coupling strengths and in different regimes of the energy bias ϵ .

3.1 Hamiltonian

By adding up the single qubit Hamiltonians of the individual qubits as introduced in (1.17) and the coupling term derived in chapter 2, we arrive at the total Hamiltonian. The currents in the qubits are quantum mechanically associated with $\hat{\sigma}_z$ operators and the Hamiltonian reads in terms of the Pauli spin matrices¹

$$\mathbf{H} = \sum_{i=1}^3 \left(-\frac{1}{2} \epsilon_i \hat{\sigma}_z^{(i)} - \frac{1}{2} \Delta_i \hat{\sigma}_x^{(i)} \right) + C (\hat{\sigma}_z^{(1)} \hat{\sigma}_z^{(2)} + \hat{\sigma}_z^{(1)} \hat{\sigma}_z^{(3)} + \hat{\sigma}_z^{(2)} \hat{\sigma}_z^{(3)}). \quad (3.1)$$

¹The superscript indices here have the meaning of being applied to the qubit with the corresponding index while unity is applied to the qubits with the missing indices (e.g. $\hat{\sigma}_z^{(3)} \equiv \mathbf{1}_2 \otimes \mathbf{1}_2 \otimes \hat{\sigma}_z$, $\hat{\sigma}_z^{(1)} \hat{\sigma}_z^{(2)} \equiv \hat{\sigma}_z \otimes \hat{\sigma}_z \otimes \mathbf{1}_2$).

Writing \mathbf{H} down in the standard basis (see A.2) yields

$$\mathbf{H} = -\frac{1}{2} \begin{pmatrix} \epsilon_1 + \epsilon_2 + \epsilon_3 - 6C & \Delta_3 & \Delta_2 & 0 & \Delta_1 & 0 & 0 & 0 \\ \Delta_3 & \epsilon_1 + \epsilon_2 - \epsilon_3 + 2C & 0 & \Delta_2 & 0 & \Delta_1 & 0 & 0 \\ \Delta_2 & 0 & \epsilon_1 - \epsilon_2 + \epsilon_3 + 2C & \Delta_3 & 0 & 0 & \Delta_1 & 0 \\ 0 & \Delta_2 & \Delta_3 & \epsilon_1 - \epsilon_2 - \epsilon_3 + 2C & 0 & 0 & 0 & \Delta_1 \\ \Delta_1 & 0 & 0 & 0 & -\epsilon_1 + \epsilon_2 + \epsilon_3 + 2C & \Delta_3 & \Delta_2 & 0 \\ 0 & \Delta_1 & 0 & 0 & \Delta_3 & -\epsilon_1 + \epsilon_2 - \epsilon_3 + 2C & 0 & \Delta_2 \\ 0 & 0 & \Delta_1 & 0 & \Delta_2 & 0 & -\epsilon_1 - \epsilon_2 + \epsilon_3 + 2C & \Delta_3 \\ 0 & 0 & 0 & \Delta_1 & 0 & \Delta_2 & \Delta_3 & -\epsilon_1 - \epsilon_2 - \epsilon_3 - 6C \end{pmatrix}. \quad (3.2)$$

We want to assume the qubits to be identical ($\Delta_1 = \Delta_2 = \Delta_3 = \Delta$, $\epsilon_1 = \epsilon_2 = \epsilon_3 = \epsilon$). We already introduced this approximation implicitly by setting the coupling C equal for all three pairs of qubits.

In the following, we choose a collective quartet-doublet basis, reflecting the nature of the system as a system of three coupled (pseudo-) spin-1/2 particles (see appendix A.4 for the definition of this basis). This will simplify many arguments related to the symmetries of the system. The Hamiltonian rewritten in the collective basis is (as from now, operators and states expressed in the collective basis carry a tilde, see also appendix A)

$$\tilde{\mathbf{H}} = -\frac{1}{2} \begin{pmatrix} 3\epsilon - 6C & \sqrt{3}\Delta & 0 & 0 & 0 & 0 & 0 & 0 \\ \sqrt{3}\Delta & \epsilon + 2C & 2\Delta & 0 & 0 & 0 & 0 & 0 \\ 0 & 2\Delta & \epsilon + 2C & \sqrt{3}\Delta & 0 & 0 & 0 & 0 \\ 0 & 0 & \sqrt{3}\Delta & -3\epsilon - 6C & 0 & 0 & 0 & 0 \\ 0 & 0 & 0 & 0 & \epsilon + 2C & \Delta & 0 & 0 \\ 0 & 0 & 0 & 0 & \Delta & -\epsilon + 2C & 0 & 0 \\ 0 & 0 & 0 & 0 & 0 & 0 & \epsilon + 2C & \Delta \\ 0 & 0 & 0 & 0 & 0 & 0 & \Delta & -\epsilon + 2C \end{pmatrix}. \quad (3.3)$$

As can be seen from 3.3, the Hamiltonian is block diagonal in the doublet and quartet subspaces. In the following, $|E_1\rangle$ – $|E_8\rangle$ denote the eigenstates of the system (E_1 – E_8 are the associated eigenenergies), where $|E_1\rangle$ – $|E_4\rangle$ correspond to the upper four by four matrix (the quartet), $|E_5\rangle$ and $|E_6\rangle$ to the first doublet, $|E_7\rangle$ and $|E_8\rangle$ to the second one. Apparently, due to the identical form of the two doublets, there are two pairs of degenerate eigenstates, $|E_5\rangle$ and $|E_7\rangle$ as well as $|E_6\rangle$ and $|E_8\rangle$. The eigenenergies and eigenstates of the doublet blocks can be found in appendix B.

Figure 3.1 displays the eigenenergies in dependence of the energy bias ϵ for different coupling strengths, ranging from large ferromagnetic coupling to large antiferromagnetic coupling. These parameter regimes will be investigated in the following.

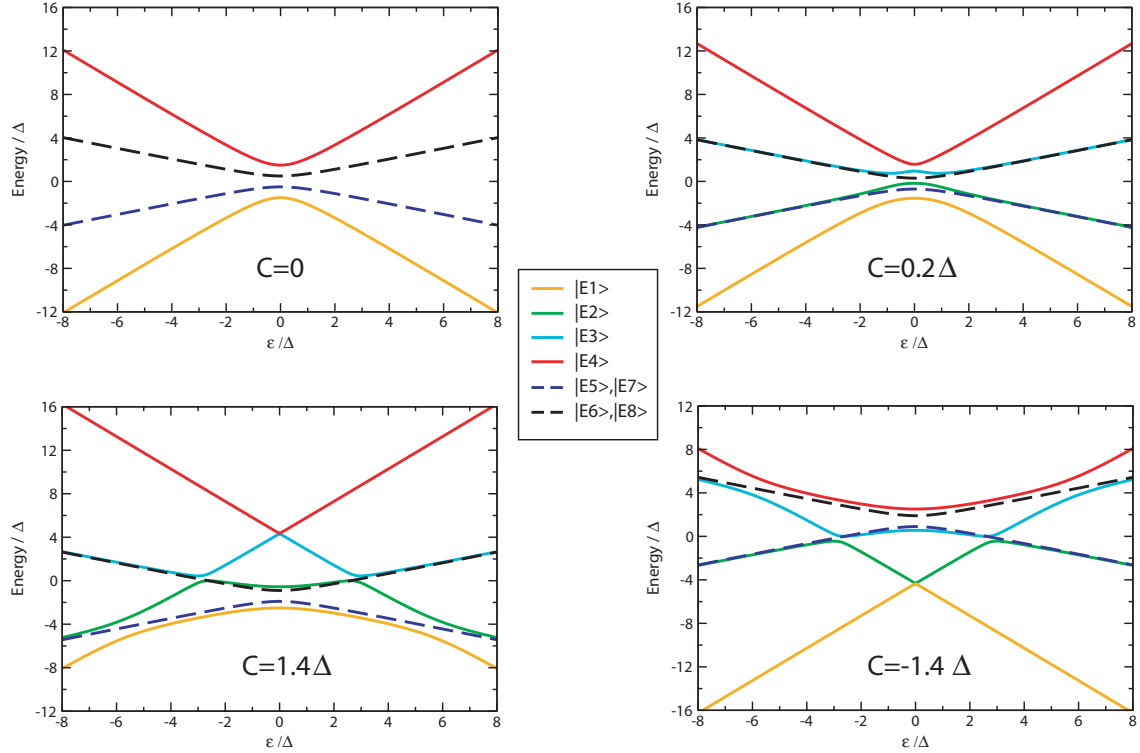


Figure 3.1: Plot of the eigenenergies of the eigenstates $|E_1\rangle$ – $|E_8\rangle$ for several coupling strengths. $|E_5\rangle$ and $|E_6\rangle$ as well as $|E_7\rangle$ and $|E_8\rangle$ are always degenerate. For $C = 0$, an additional degeneracy involving $|E_2\rangle$ and $|E_3\rangle$ is imposed, which is lifted for finite coupling strengths (details in the text). The energy level diagram for the ferromagnetic coupling $C = -1.4\Delta$ is just opposed to the case of antiferromagnetic coupling of the same strength.

For discussion of the eigenstates we refer to figures C.1–C.3.

3.2 No coupling, $C = 0$

We first explore the case of vanishing coupling, $C = 0$. Apparently, no entangled states can be found in this regime, the system can be described by three disjoint, independent quantum systems. As a result, all eigenstates can be written as tensor products of the eigenstates of the single qubits. Nevertheless, the discussion provides some insight into symmetries of the system and will therefore be performed here. As a first observation, we find the energy spectrum of the system to be symmetrical around zero energy as well as zero energy bias ($\epsilon = 0$). Moreover, the amplitudes of all eigenstates show the same behavior as function of the energy bias ϵ , as can be seen in figure C.1, but in terms of different basis states and with different relative phases (see below). Both observations obey the fact that the system is invariant under a combined flip of the spins and an inversion of the sign of ϵ . This is

obvious as ϵ is (due to the missing coupling) the only parameter that determines the spin alignment (and hence the energy of a certain configuration), favoring spins aligned parallel to the applied magnetic field and giving an energy disadvantage to the opposite aligned ones. We also find that for the same reason the ground state maps onto the highest excited state by just a global spin flip. We will refer to these general considerations when looking at the case of finite coupling and will now explicitly write down the form of the some of the eigenstates in standard notation.

3.2.1 No energy bias, $\epsilon = 0$

Without energy bias, for zero coupling as well as for finite coupling (see below), no $\hat{\sigma}_z$ spin alignment in either direction is preferred, therefore all states will yield zero expectation value for $\hat{\sigma}_z$, $\langle \hat{\sigma}_z^{(1)} \rangle = \langle \hat{\sigma}_z^{(2)} \rangle = \langle \hat{\sigma}_z^{(3)} \rangle = \langle \hat{\sigma}_z^{(1)} + \hat{\sigma}_z^{(2)} + \hat{\sigma}_z^{(3)} \rangle = 0$. The single qubit Hamiltonian (1.17) then reduces to $\mathbf{H} = -\frac{1}{2} \Delta \hat{\sigma}_x$ with the two well-known eigenstates $|\psi_G\rangle = 1/\sqrt{2}(|\downarrow\rangle + |\uparrow\rangle)$ (ground state) and $|\psi_{\text{ex}}\rangle = 1/\sqrt{2}(|\downarrow\rangle - |\uparrow\rangle)$ (excited state). The ground state of the composite three-qubit system $|E_1\rangle$ is the direct product of the $\hat{\sigma}_x$ eigenstates with the lower energy (crossing point of the curves in the first plot of figure C.1),

$$|\psi_G\rangle = |E_1\rangle = \frac{1}{\sqrt{8}}(|\downarrow\rangle + |\uparrow\rangle)_A \otimes (|\downarrow\rangle + |\uparrow\rangle)_B \otimes (|\downarrow\rangle + |\uparrow\rangle)_C, \quad (3.4)$$

whereas the highest excited state reads (crossing point in the fourth plot)

$$|\psi_{\text{ex}}\rangle = |E_4\rangle = \frac{1}{\sqrt{8}}(|\downarrow\rangle - |\uparrow\rangle)_A \otimes (|\downarrow\rangle - |\uparrow\rangle)_B \otimes (|\downarrow\rangle - |\uparrow\rangle)_C. \quad (3.5)$$

Reflecting the symmetry of the system under exchange of qubits, the other six eigenenergies split up in two 3-fold degenerate subspaces, the corresponding states being $|E_2\rangle, |E_5\rangle, |E_7\rangle$ (first excitation above the ground state) and $|E_3\rangle, |E_6\rangle, |E_8\rangle$ (second excitation above the ground state). These subspaces contain states with different properties, including non-zero entanglement. However, we make here a physical choice for the basis states, taking into account that the system physically consists of three disjoint subsystems.

The basis states spanning the low-energy subspace for $\epsilon = 0$ then read

$$\begin{aligned} |E_2\rangle &:= (|\downarrow\rangle + |\uparrow\rangle)_A \otimes (|\downarrow\rangle + |\uparrow\rangle)_B \otimes (|\downarrow\rangle - |\uparrow\rangle)_C, \\ |E_5\rangle &:= (|\downarrow\rangle + |\uparrow\rangle)_A \otimes (|\downarrow\rangle - |\uparrow\rangle)_B \otimes (|\downarrow\rangle + |\uparrow\rangle)_C, \\ |E_7\rangle &:= (|\downarrow\rangle - |\uparrow\rangle)_A \otimes (|\downarrow\rangle + |\uparrow\rangle)_B \otimes (|\downarrow\rangle + |\uparrow\rangle)_C \end{aligned} \quad (3.6)$$

and for the high-energy subspace

$$\begin{aligned} |E_3\rangle &:= (|\downarrow\rangle - |\uparrow\rangle)_A \otimes (|\downarrow\rangle - |\uparrow\rangle)_B \otimes (|\downarrow\rangle + |\uparrow\rangle)_C, \\ |E_6\rangle &:= (|\downarrow\rangle - |\uparrow\rangle)_A \otimes (|\downarrow\rangle + |\uparrow\rangle)_B \otimes (|\downarrow\rangle - |\uparrow\rangle)_C, \\ |E_8\rangle &:= (|\downarrow\rangle + |\uparrow\rangle)_A \otimes (|\downarrow\rangle - |\uparrow\rangle)_B \otimes (|\downarrow\rangle - |\uparrow\rangle)_C. \end{aligned} \quad (3.7)$$

The basis states are composed of the low-energy eigenvalues with respect to two of the qubits and a high-energy eigenvalue with respect to the third one for the low-energy subspace, and oppositely for the high-energy subspace.

One can see that all eigenstates occurring at zero energy bias are superpositions of all basis states, where all basis states are equal in amplitude, only varying in their relative phases. Particularly, all eigenstates contain contributions from the two totally aligned states $|\uparrow\uparrow\uparrow\rangle$ and $|\downarrow\downarrow\downarrow\rangle$. As we will see in section 3.3 and 3.4, this is not true for finite coupling.

3.2.2 High energy bias

With increasing (positive) energy bias, the energy degeneracy between spin up and spin down states expressed by their equal amplitudes is lifted. For the ground state $|E_1\rangle$, spins aligned antiparallel to the magnetic field increasingly get suppressed, with the totally misaligned state $|\downarrow\downarrow\downarrow\rangle$ decaying quickest. In the limit of large energy bias, only the totally aligned component of the ground state is left,

$$|\psi_G\rangle = |E_1\rangle = |\uparrow\uparrow\uparrow\rangle. \quad (3.8)$$

The highest state in analogy looks like

$$|\psi_{\text{ex}}\rangle = |\downarrow\downarrow\downarrow\rangle. \quad (3.9)$$

These are the classical states of the system for large energy bias (no superposition).

For the states spanning the degenerate subspaces we get classical, frustrated states with $\hat{\sigma}_z$ expectation values of $\langle\hat{\sigma}_z^{(1)} + \hat{\sigma}_z^{(2)} + \hat{\sigma}_z^{(3)}\rangle = \frac{1}{2}$ for the low-energy subspace,

$$|E_2\rangle = |\uparrow\uparrow\downarrow\rangle \quad , \quad |E_5\rangle = |\downarrow\uparrow\uparrow\rangle \quad , \quad |E_7\rangle = |\uparrow\downarrow\uparrow\rangle, \quad (3.10)$$

and $\langle\hat{\sigma}_z^{(1)} + \hat{\sigma}_z^{(2)} + \hat{\sigma}_z^{(3)}\rangle = -\frac{1}{2}$ for the high-energy subspace,

$$|E_3\rangle = |\downarrow\downarrow\uparrow\rangle \quad , \quad |E_6\rangle = |\downarrow\uparrow\downarrow\rangle \quad , \quad |E_8\rangle = |\uparrow\downarrow\downarrow\rangle. \quad (3.11)$$

3.3 Weak antiferromagnetic coupling, $C = 0.2 \Delta$

Introducing a $\hat{\sigma}_z \otimes \hat{\sigma}_z$ coupling into the system for small energy bias lifts the three-fold degeneracies described above into two-fold degeneracies. Thus, the states $|E_2\rangle$, $|E_5\rangle$, $|E_7\rangle$, $|E_3\rangle$, $|E_6\rangle$ and $|E_8\rangle$ do not have a direct counterpart for zero coupling and only the ground state $|E_1\rangle$ and the highest excited state $|E_4\rangle$ can be directly compared to the case of $C = 0$.

3.3.1 Ground state and highest excited state

The antiferromagnetic coupling energetically favors frustrated states. For $\epsilon = 0$, the ground state $|E_1\rangle$ therefore contains a larger contribution of frustrated states and a smaller contribution of aligned states compared to the case of vanishing coupling. The highest excited state $|E_4\rangle$ shows the opposite behavior. For large energy bias, the states converge to the states for zero coupling and the plots look the same.

3.3.2 The degenerate subspaces

As already mentioned, the three-fold degeneracies for $C = 0$ are for finite coupling lifted into two-fold degeneracies. This can be understood by looking at the collective basis in appendix A. We want to point out the situation for zero energy bias.

Again the expectation value for the total $\hat{\sigma}_z$ component of the states will be zero, $\langle\hat{\sigma}_z^{\text{tot}}\rangle = \langle\hat{\sigma}_z^{(1)} + \hat{\sigma}_z^{(2)} + \hat{\sigma}_z^{(3)}\rangle = 0$. This results in equal superpositions of states with opposite $\hat{\sigma}_z$ expectation values. We can construct a state with $\langle\hat{\sigma}_z\rangle = 0$ by a superposition of $|\tilde{v}_5\rangle$ and $|\tilde{v}_6\rangle$, $|\tilde{v}_7\rangle$ and $|\tilde{v}_8\rangle$, as well as $|\tilde{v}_2\rangle$ and $|\tilde{v}_3\rangle$ (note that the second quantum number in the notation of the collective basis states as in appendix A gives the $\hat{\sigma}_z$ expectation value). An equal superposition of $|\tilde{v}_1\rangle$ and $|\tilde{v}_4\rangle$ also yields $\langle\hat{\sigma}_z\rangle = 0$; however, due to the antiferromagnetic coupling,

this aligned state is energetically raised compared to the frustrated states. Moreover, it turns out that a superposition of $|\tilde{v}_2\rangle$ and $|\tilde{v}_3\rangle$ is not an eigenstate of the system. The remaining superpositions span the two subspaces².

The low-energy subspace is spanned by

$$\begin{aligned} |\tilde{\psi}_1^L\rangle &= x |\tilde{v}_5\rangle + \sqrt{1-x^2} |\tilde{v}_6\rangle, \\ |\tilde{\psi}_2^L\rangle &= x |\tilde{v}_7\rangle + \sqrt{1-x^2} |\tilde{v}_8\rangle, \end{aligned} \quad (3.12)$$

the high-energy subspace by

$$\begin{aligned} |\tilde{\psi}_1^H\rangle &= x' |\tilde{v}_5\rangle - \sqrt{1-x'^2} |\tilde{v}_6\rangle, \\ |\tilde{\psi}_2^H\rangle &= x' |\tilde{v}_7\rangle - \sqrt{1-x'^2} |\tilde{v}_8\rangle. \end{aligned} \quad (3.13)$$

For zero energy bias x and x' read (for the general form of x and x' see appendix B)

$$x = x' = \frac{1}{\sqrt{2}}. \quad (3.14)$$

All four states are superpositions of states with $\langle \hat{\sigma}_z \rangle = \pm \frac{1}{2}$, i.e. frustrated states. The application of the operator representing the coupling to any frustrated state $|f\rangle$ yields

$$\left(\hat{\sigma}_z^{(1)} \hat{\sigma}_z^{(2)} + \hat{\sigma}_z^{(1)} \hat{\sigma}_z^{(3)} + \hat{\sigma}_z^{(2)} \hat{\sigma}_z^{(3)} \right) |f\rangle = -|f\rangle. \quad (3.15)$$

All frustrated states are thus eigenstates of the coupling for any arbitrary coupling strength. Therefore, $|\tilde{\psi}_1^L\rangle, |\tilde{\psi}_2^L\rangle, |\tilde{\psi}_1^H\rangle, |\tilde{\psi}_2^H\rangle$ do not depend on the coupling strength. Formally, this is expressed by the coupling C being located as factor in front of the doublet matrices.

Low-energy subspace

$$|\tilde{\psi}^L\rangle = A |\tilde{\psi}_1^L\rangle + e^{i\varphi} \sqrt{1-A^2} |\tilde{\psi}_2^L\rangle \quad (3.16)$$

is an arbitrary state in the low-energy subspace. In chapter 4, the topic will be covered how to prepare given states, with respect to the relative amplitudes as well as phases, in these degenerate subspaces. Here, we take a look at –in terms of entanglement– significant resulting states.

For quantifying entanglement, we use so-called *global entanglement* here, addressed in chapter 5 and appendix D.2. The amplitude A and phase φ of the states $|E_5\rangle$ and $|E_7\rangle$ displayed in figures C.2 and C.3 are chosen such as to maximize (the state displayed in box 5), respectively minimize (displayed in Box 7) the global entanglement. Remarkably, the optimal choice for A and φ does not depend on the energy bias.

We obtain maximal entanglement for the state

$$|\tilde{\psi}_{\max}^L\rangle = \frac{1}{\sqrt{2}} (|\tilde{\psi}_1^L\rangle + i |\tilde{\psi}_2^L\rangle) := |\tilde{E}_5\rangle, \quad (3.17)$$

²These are the eigenstates of the 2×2 block matrices (the doublets) of the coupled Hamiltonian (cp. appendix B)

and minimal entanglement for

$$|\tilde{\psi}_{\min}^L\rangle = \frac{1}{\sqrt{2}}(|\tilde{\psi}_1^L\rangle + |\tilde{\psi}_2^L\rangle) := |\tilde{E}_7\rangle. \quad (3.18)$$

The global entanglement for $|\tilde{\psi}_{\max}^L\rangle$ is $\frac{8}{9}$, equal to the so-called W (*Werner*) state

$$|W\rangle = \frac{1}{\sqrt{3}}(|\uparrow\uparrow\downarrow\rangle + |\uparrow\downarrow\uparrow\rangle + |\downarrow\uparrow\uparrow\rangle). \quad (3.19)$$

For zero energy bias, the state $|\tilde{\psi}_{\max}^L\rangle$ transformed into the standard basis has the form

$$\begin{aligned} |\psi_{\max}^L\rangle &= S^\dagger |\tilde{\psi}_{\max}^L\rangle = \\ &= \frac{1}{2\sqrt{6}} \left\{ 2(|\uparrow\uparrow\downarrow\rangle + |\downarrow\downarrow\uparrow\rangle) - (1 - i\sqrt{3})(|\uparrow\downarrow\uparrow\rangle + |\downarrow\uparrow\downarrow\rangle) - (1 + i\sqrt{3})(|\uparrow\downarrow\downarrow\rangle + |\downarrow\uparrow\uparrow\rangle) \right\}. \end{aligned} \quad (3.20)$$

In fact, as suggested by the equal value for the global entanglement, $|\psi_{\max}^L\rangle$ can be transferred onto a W state by a unitary operator \hat{U}^L composed of purely local operations,

$$\hat{U}^L |\psi_{\max}^L\rangle = |W\rangle \quad (3.21)$$

with

$$\hat{U}^L = \{e^{-i\pi/3} \hat{R}_y(\pi/2)\}^{(1)} \otimes \{\hat{R}_z(2\pi/3) \hat{R}_y(\pi/2)\}^{(2)} \otimes \{\hat{R}_z(-2\pi/3) \hat{R}_y(\pi/2)\}^{(3)}, \quad (3.22)$$

where $\hat{R}_z(\theta)$ ($\hat{R}_y(\theta)$) rotates the qubit by an angle θ around the z-axis (y-axis),

$$\hat{R}_z(\theta) = e^{-i\frac{\theta}{2}\hat{\sigma}_z}, \quad \hat{R}_y(\theta) = e^{-i\frac{\theta}{2}\hat{\sigma}_y}. \quad (3.23)$$

Since \hat{U}^L is a tensor product of operations acting on the individual qubits (subsystems), whereas entanglement is a resource reflecting correlations between subsystems, \hat{U} does not change the entanglement properties of the state. In this sense, $|\psi_{\max}^L\rangle$ and $|W\rangle$ are called locally equivalent³.

High-energy subspace

The same considerations employed for the low-energy subspace also apply to the high-energy subspace. The plots in box 6 and box 8 in figures C.2 and C.3 are again –with respect to the entanglement– the maximized and minimized superpositions of the basis states $|\tilde{\psi}_1^H\rangle$ and $|\tilde{\psi}_2^H\rangle$; optimal amplitude and phase are identical to (3.17) and (3.18):

$$|\tilde{\psi}_{\max}^H\rangle = \frac{1}{\sqrt{2}}(|\tilde{\psi}_1^H\rangle + i|\tilde{\psi}_2^H\rangle) := |\tilde{E}_6\rangle \quad (3.24)$$

$$|\tilde{\psi}_{\min}^H\rangle = \frac{1}{\sqrt{2}}(|\tilde{\psi}_1^H\rangle + |\tilde{\psi}_2^H\rangle) := |\tilde{E}_8\rangle \quad (3.25)$$

³ \hat{U} belongs to a general class of operations called LOCC (local operations and classical communication).

Again we write for zero energy bias the explicit form of $|\tilde{\psi}_{\max}^H\rangle$ in the standard basis,

$$\begin{aligned} |\psi_{\max}^H\rangle &= S^\dagger |\tilde{\psi}_{\max}^H\rangle = \\ &= \frac{1}{2\sqrt{6}} \left\{ 2(|\uparrow\uparrow\downarrow\rangle + |\downarrow\downarrow\uparrow\rangle) + (1 - i\sqrt{3})(|\uparrow\downarrow\uparrow\rangle - |\downarrow\uparrow\downarrow\rangle) + (1 + i\sqrt{3})(|\uparrow\downarrow\downarrow\rangle - |\downarrow\uparrow\uparrow\rangle) \right\}, \end{aligned} \quad (3.26)$$

and can find a local transformation rotating this state onto the W state,

$$\hat{U}^H = \{e^{-i\pi/3} \hat{H}\}^{(1)} \otimes \{\hat{R}_z(2\pi/3) \hat{H}\}^{(2)} \otimes \{\hat{R}_z(-2\pi/3) \hat{H}\}^{(3)}, \quad (3.27)$$

where \hat{H} denotes the Hadamard gate,

$$\hat{H} = \frac{1}{\sqrt{2}} \begin{pmatrix} 1 & 1 \\ 1 & -1 \end{pmatrix}. \quad (3.28)$$

3.4 Strong antiferromagnetic coupling, $C = 1.4 \Delta$

In this regime due to the large coupling, frustrated alignment of spins is strongly favored.

3.4.1 Ground state and the highest excited states

The arguments provided in 3.3.1 concerning the ground state and the highest excited state for the weak antiferromagnetic coupling apply even more intensively to the case of strong antiferromagnetic coupling.

The ground state for zero energy bias takes the form

$$|\psi_G\rangle = |E_1\rangle = \frac{1}{\sqrt{6 + 2\delta^2}} (|\uparrow\uparrow\downarrow\rangle + |\uparrow\downarrow\uparrow\rangle + |\uparrow\downarrow\downarrow\rangle + |\downarrow\uparrow\uparrow\rangle + |\downarrow\downarrow\uparrow\rangle + |\downarrow\uparrow\downarrow\rangle + \delta(|\uparrow\uparrow\uparrow\rangle + |\downarrow\downarrow\downarrow\rangle)), \quad (3.29)$$

where δ is small ($\delta \rightarrow 0$ for $C \rightarrow \infty$, $\delta \approx 0.2$ for $C = 1.4 \Delta$), i.e. the aligned states $|\uparrow\uparrow\uparrow\rangle$ and $|\downarrow\downarrow\downarrow\rangle$ are strongly suppressed.

The two highest excited states $|E_3\rangle$ (box 3 in figure C.3) and $|E_4\rangle$ (box 4 in figure C.3), however, show an interesting behavior. In a small range for the energy bias ϵ around zero, $|E_3\rangle$ and $|E_4\rangle$ are superpositions of the maximally unfavorable states in terms of energy, i.e. of the states $|\uparrow\uparrow\uparrow\rangle$ and $|\downarrow\downarrow\downarrow\rangle$.

For zero energy bias we obtain

$$\begin{aligned} |E_3\rangle &= \frac{1}{\sqrt{2 + 6\delta'^2}} (|\uparrow\uparrow\uparrow\rangle + |\downarrow\downarrow\downarrow\rangle - \delta'(|\uparrow\uparrow\downarrow\rangle + |\uparrow\downarrow\uparrow\rangle + |\uparrow\downarrow\downarrow\rangle + |\downarrow\uparrow\uparrow\rangle + |\downarrow\downarrow\uparrow\rangle + |\downarrow\uparrow\downarrow\rangle)) \\ &\text{with } \delta' \approx 0.07, \text{ therefore } |E_3\rangle \approx \frac{1}{\sqrt{2}} (|\uparrow\uparrow\uparrow\rangle + |\downarrow\downarrow\downarrow\rangle). \end{aligned} \quad (3.30)$$

$$\begin{aligned} |E_4\rangle &= \frac{1}{\sqrt{2 + 6\delta''^2}} (-|\uparrow\uparrow\uparrow\rangle + |\downarrow\downarrow\downarrow\rangle + \delta''(|\uparrow\uparrow\downarrow\rangle + |\uparrow\downarrow\uparrow\rangle - |\uparrow\downarrow\downarrow\rangle + |\downarrow\uparrow\uparrow\rangle - |\downarrow\downarrow\uparrow\rangle - |\downarrow\uparrow\downarrow\rangle)) \\ &\text{with } \delta'' \approx 0.1, \text{ therefore } |E_4\rangle \approx \frac{1}{\sqrt{2}} (|\downarrow\downarrow\downarrow\rangle - |\uparrow\uparrow\uparrow\rangle). \end{aligned} \quad (3.31)$$

Despite the antiferromagnetic coupling, $|E_3\rangle$ and $|E_4\rangle$ are for small energy bias close to superpositions that contain only the macroscopically distinct states $|\uparrow\uparrow\uparrow\rangle$ and $|\downarrow\downarrow\downarrow\rangle$ with equal amplitude. Such states are called GHZ (*Greenberger-Horne-Zeilinger*) states. The interesting entanglement properties of GHZ states are covered in chapter 5.

3.4.2 The degenerate subspaces

As emphasized above, the form of the states in the degenerate subspaces *does not depend on the coupling strength*, the coupling only shifts the states in energy (cp. appendix B and (3.15)). Therefore, all statements made in 3.3.2 apply without modification. In the next chapter, we will show how to prepare arbitrary states –i.e. arbitrary superpositions of $|\psi_1^L\rangle$ and $|\psi_2^L\rangle$ ($|\psi_1^H\rangle$ and $|\psi_2^H\rangle$, respectively)– in these subspaces by means of external driving. Due to the particular stability of these states with respect to the coupling, the results are not limited to a particular design scheme or coupling.

Chapter 4

Preparing states in the degenerate subspaces

We aim for preparing arbitrary states in the degenerate subspaces introduced in 3.3.2, i.e. we want to apply a π -pulsing scheme in order to fully depopulate the ground state and populate the desired subspace with an arbitrary superpositions of $|\psi_1^L\rangle$ and $|\psi_2^L\rangle$ ($|\psi_1^H\rangle$ and $|\psi_2^H\rangle$, respectively),

$$|\psi^{L(H)}\rangle = A |\psi_1^{L(H)}\rangle + e^{i\varphi} \sqrt{1 - A^2} |\psi_2^{L(H)}\rangle . \quad (4.1)$$

This is different from ordinary π -pulse driving for the fact that two degenerate states above the ground state need to be populated in parallel with a given amplitude ratio and relative phase. We investigate this situation by the use of a dressed state approach. Note that analogous results can be obtained by the use of Floquet states and classical driving [32].

We consider driving of the system by means of external radiofrequency (*rf*) pulses. The applied oscillating flux couples in via the energy bias ϵ_i to the $\hat{\sigma}_z$ component of the Hamiltonian, given by

$$\epsilon_i'(t) = 2 I_{p,i} \left(\Phi_{\text{tot},i}(t) - \frac{\Phi_0}{2} \right) = 2 I_{p,i} \left(\Phi_i + \Phi_{\text{rf},i}(t) - \frac{\Phi_0}{2} \right) = \epsilon_i + \delta\epsilon_i(t) . \quad (4.2)$$

Here, we consider individual microwave amplitudes for the qubits. The Hamiltonians for the individual qubits have the form

$$\mathbf{H}_i = -\frac{1}{2} \epsilon_i'(t) \hat{\sigma}_z^{(i)} - \frac{1}{2} \Delta_i \hat{\sigma}_x^{(i)} = -\frac{1}{2} \epsilon_i \hat{\sigma}_z^{(i)} - \frac{1}{2} \Delta_i \hat{\sigma}_x^{(i)} - \frac{1}{2} \delta\epsilon_i(t) \hat{\sigma}_z^{(i)} , \quad (4.3)$$

where $\delta\epsilon_i(t) = \delta\epsilon_i \cos \omega t$ is a periodic perturbation.

The total Hamiltonian of the system can then be written as

$$\mathbf{H} = \mathbf{H}_0 + \hat{V}(t) . \quad (4.4)$$

\mathbf{H}_0 is the unperturbed Hamiltonian of the system as given in (3.1) and $\hat{V}(t)$ is the periodic perturbation

$$\hat{V}(t) = -\frac{1}{2} \underbrace{\{ \delta\epsilon_1 \hat{\sigma}_z^{(1)} + \delta\epsilon_2 \hat{\sigma}_z^{(2)} + \delta\epsilon_3 \hat{\sigma}_z^{(3)} \}}_{\hat{V}_0} \cos \omega t . \quad (4.5)$$

We choose a parametrization in polar coordinates in order to make sure that the maximal transition rate does not depend on the ratio of the relative amplitudes driving the individual qubits (given by κ_1 and κ_2), but only on a global driving amplitude κ ,

$$\hat{V}_0 = \frac{\kappa}{3} \left\{ \begin{pmatrix} 1 \\ 1 \\ 1 \end{pmatrix} + \kappa_1 \begin{pmatrix} 1 \\ 0 \\ -1 \end{pmatrix} + \kappa_2 \begin{pmatrix} 1 \\ -1 \\ 0 \end{pmatrix} \right\} \begin{pmatrix} \hat{\sigma}_z^{(1)} \\ \hat{\sigma}_z^{(2)} \\ \hat{\sigma}_z^{(3)} \end{pmatrix} \quad \text{with } 0 \leq \kappa_1, \kappa_2 \leq 1 \quad (4.6)$$

4.1 Quantizing the electromagnetic field and the interaction Hamiltonian

The electromagnetic field can be written quantum mechanically as a sum over all modes of the field, each one corresponding to a harmonic oscillator. However, by driving with a laser, we can achieve the situation of a near-monochromatic field, i.e. a field with a dominating mode and a narrow line width. Therefore, we want to treat it (in the ideal limit) as a monochromatic, single mode quantum field, disregarding all modes except the one being resonant with the desired transition of the system [33].

The Hamiltonian of the field mode with frequency ω reads

$$\mathbf{H}_F = \hbar\omega \left(a^\dagger a + \frac{1}{2} \right) \quad (4.7)$$

with a^\dagger and a being the creation and annihilation operators, whose effect on number states $|n\rangle$ is given by

$$a^\dagger |n\rangle = \sqrt{n+1} |n+1\rangle, \quad (4.8)$$

$$a |n\rangle = \sqrt{n} |n-1\rangle, \quad (4.9)$$

$$a^\dagger a |n\rangle = n |n\rangle. \quad (4.10)$$

At the coordinate origin, the magnetic field vector can be written as

$$\vec{B} = i\vec{\epsilon} B_0 (a + a^\dagger). \quad (4.11)$$

Here, B_0 is the field strength and $\vec{\epsilon}$ is the polarization of the field.

To lowest order, the interaction is a dipole-dipole interaction between the field and the dipole moment of the qubits, which is aligned along $\hat{\sigma}_z$, and we obtain the interaction between the field and a qubit,

$$\mathbf{H}_I = g_I \hat{\sigma}_z (a^\dagger + a). \quad (4.12)$$

g_I is the coupling constant which describes the strength of the interaction. It depends on details of the experimental realization.

Adding up the system Hamiltonian \mathbf{H}_0 , the Hamiltonian of the field mode \mathbf{H}_F and the interaction \mathbf{H}_I (rewritten in terms of \hat{V}_0 as introduced above), we arrive at the total Hamiltonian,

$$\mathbf{H} = \mathbf{H}_0 + \hbar\omega \left(a^\dagger a + \frac{1}{2} \right) + \hat{g}_I V_0 (a^\dagger + a). \quad (4.13)$$

In what follows we assume that the mean number of photons $\langle n \rangle$ (which will simply be referred to as n in the following) is large. In 4.2 we will calculate expectation values of the creation and annihilation operators, scaling with \sqrt{n} . These expectation values are affected by a fluctuation δn in the number of photons as

$$\frac{\sqrt{n + \delta n} - \sqrt{n}}{\sqrt{n}} = \frac{\sqrt{n}}{\sqrt{n}} \left(\sqrt{1 + \frac{\delta n}{n}} - 1 \right) \approx \frac{1}{2} \frac{\delta n}{n}, \quad (4.14)$$

where in the last step a Taylor approximation was applied.

For large n , however, the width δn in the distribution of the number of photons is small compared to n . For example for a coherent state holds $\delta n = \sqrt{n}$ [33], yielding

$$\lim_{n \rightarrow \infty} \frac{\sqrt{n + \delta n} - \sqrt{n}}{\sqrt{n}} = \lim_{n \rightarrow \infty} \frac{1}{2\sqrt{n}} = 0. \quad (4.15)$$

This results in the system being subjected to the same field intensity during the experiment.

4.2 Preparing given states in the degenerate subspaces

We first disregard the coupling expressed by \mathbf{H}_I . The state of the composite system consisting of the qubits and the electromagnetic field can be written as $|\psi, n\rangle$, where the labels in the ket are |qubits, field>, i.e. qubits in the state $|\psi\rangle$, and n being the number of photons.

For propagating the system from the ground state to one of the excited two-fold degenerate subspaces, we choose the frequency of the mode to be resonant with the transition frequency from the ground state to the excited level (the indices 'e' and 'g' stand for the ground state and the excited states, respectively),

$$\hbar\omega = E_e - E_g. \quad (4.16)$$

Consider the three states

$$|g, n\rangle, \quad |e_1, n-1\rangle, \quad |e_2, n-1\rangle, \quad (4.17)$$

where $|e_1\rangle$ and $|e_2\rangle$ are two arbitrary states in the degenerate subspace.

The three states in (4.17) are energetically degenerate eigenstates of the *uncoupled* Hamiltonian $(\mathbf{H}_0 + \mathbf{H}_F)$,

$$\begin{aligned} (\mathbf{H}_0 + \mathbf{H}_F) |g, n\rangle &= \mathbf{H}_0 |g, n\rangle + \hbar\omega(a^\dagger a + 1/2) |g, n\rangle = \{E_g + \hbar\omega(n + 1/2)\} |g, n\rangle \\ (\mathbf{H}_0 + \mathbf{H}_F) |e_1, n-1\rangle &= \{E_e + \hbar\omega(n-1 + 1/2)\} |e_1, n-1\rangle = \{E_g + \hbar\omega(n + 1/2)\} |e_1, n-1\rangle \\ (\mathbf{H}_0 + \mathbf{H}_F) |e_2, n-1\rangle &= \{E_e + \hbar\omega(n-1 + 1/2)\} |e_2, n-1\rangle = \{E_g + \hbar\omega(n + 1/2)\} |e_2, n-1\rangle. \end{aligned} \quad (4.18)$$

We can now introduce the couplings between the field and the qubits. The couplings correspond to absorption ($|g, n\rangle \rightarrow |e_1, n-1\rangle$, $|g, n\rangle \rightarrow |e_2, n-1\rangle$) and stimulated emission ($|e_1, n-1\rangle \rightarrow |g, n\rangle$, $|e_2, n-1\rangle \rightarrow |g, n\rangle$) processes.

We first note that the transition matrix elements between the states $|e_1, n-1\rangle$ and $|e_2, n-1\rangle$ vanish,

$$\langle e_1, n-1|(a^\dagger + a)|e_2, n-1\rangle = \langle e_1, n-1|\sqrt{n+1}|e_2, n-2\rangle + \langle e_1, n-1|\sqrt{n}|e_2, n\rangle = 0, \quad (4.19)$$

since the number states are orthogonal, $\langle n|m\rangle = \delta_{nm}$.

The elements between the ground state and the excited states, however, are non-zero,

$$\langle g, n|g_I \hat{V}_0(a^\dagger + a)|e_1, n-1\rangle = g_I \sqrt{n} \langle g, n|\hat{V}_0|e_1, n\rangle, \quad (4.20)$$

$$\langle g, n|g_I \hat{V}_0(a^\dagger + a)|e_2, n-1\rangle = g_I \sqrt{n} \langle g, n|\hat{V}_0|e_2, n\rangle. \quad (4.21)$$

We write down the matrix representing the reduced perturbation in the tree-fold degenerate subspace, spanned by the states in (4.17). The basis states are numbered as

$$|g, n\rangle = \begin{pmatrix} 1 \\ 0 \\ 0 \end{pmatrix}, \quad |e_1, n-1\rangle = \begin{pmatrix} 0 \\ 1 \\ 0 \end{pmatrix}, \quad |e_2, n-1\rangle = \begin{pmatrix} 0 \\ 0 \\ 1 \end{pmatrix}. \quad (4.22)$$

With this choice for the basis, the reduced perturbation takes the form

$$\hat{V}_0^{\text{red}} = g_I \sqrt{n} \begin{pmatrix} 0 & \langle g|\hat{V}_0|e_1\rangle & \langle g|\hat{V}_0|e_2\rangle \\ \langle e_1|\hat{V}_0|g\rangle & 0 & 0 \\ \langle e_2|\hat{V}_0|g\rangle & 0 & 0 \end{pmatrix}. \quad (4.23)$$

4.2.1 Driving the low-energy subspace

For convenience purposes, we calculate \hat{V}_0^{red} in the coupled basis introduced in appendix A,

$$\hat{V}_0^{\text{red}} = g_I \sqrt{n} \begin{pmatrix} 0 & \langle \tilde{g}|\tilde{V}_0|\tilde{e}_1\rangle & \langle \tilde{g}|\tilde{V}_0|\tilde{e}_2\rangle \\ \langle \tilde{e}_1|\tilde{V}_0|\tilde{g}\rangle & 0 & 0 \\ \langle \tilde{e}_2|\tilde{V}_0|\tilde{g}\rangle & 0 & 0 \end{pmatrix}. \quad (4.24)$$

As pointed out in chapter 3.3.2 and explicitly written down in appendix B, the lower energy subspace is spanned by $|\tilde{\psi}_1^L\rangle$ and $|\tilde{\psi}_2^L\rangle$, which are superpositions of $|\tilde{v}_5\rangle$ and $|\tilde{v}_7\rangle$ ($|\tilde{v}_6\rangle$ and $|\tilde{v}_8\rangle$, respectively), whereas the ground state $|\tilde{E}_4\rangle$ is a superposition of $\{|\tilde{v}_1\rangle, \dots, |\tilde{v}_4\rangle\}$. Moreover, the state vectors have only real entries (the Hamiltonian is purely real). This enables us –without further knowledge about the structure of the states– to write

$$|\tilde{g}\rangle = |\tilde{E}_4\rangle = \begin{pmatrix} g_1 \\ g_2 \\ g_3 \\ \pm\sqrt{1-g_1^2-g_2^2-g_3^2} \\ 0 \\ 0 \\ 0 \\ 0 \end{pmatrix}, \quad |\tilde{e}_1\rangle = |\tilde{\psi}_1^L\rangle = \begin{pmatrix} 0 \\ 0 \\ 0 \\ 0 \\ e \\ \sqrt{1-e^2} \\ 0 \\ 0 \end{pmatrix}, \quad |\tilde{e}_2\rangle = |\tilde{\psi}_2^L\rangle = \begin{pmatrix} 0 \\ 0 \\ 0 \\ 0 \\ 0 \\ 0 \\ e \\ \sqrt{1-e^2} \end{pmatrix}. \quad (4.25)$$

We obtain

$$\begin{aligned}\hat{V}_0^{\text{red}} &= -\sqrt{\frac{2}{3}}g_{\text{I}}\sqrt{n}(eg_2 + \sqrt{1-e^2}g_3)\begin{pmatrix} 0 & \sqrt{3}\kappa_1 & \kappa_1 + 2\kappa_2 \\ \sqrt{3}\kappa_1 & 0 & 0 \\ \kappa_1 + 2\kappa_2 & 0 & 0 \end{pmatrix} = \\ &= \hbar\begin{pmatrix} 0 & \omega_1 & \omega_2 \\ \omega_1 & 0 & 0 \\ \omega_2 & 0 & 0 \end{pmatrix}.\end{aligned}\quad (4.26)$$

Here, all the constants¹ have been substituted by the Rabi frequencies ω_1 and ω_2 .

When we take into account this coupling between $|g, n\rangle$ and $|e_1, n-1\rangle$, as well as between $|g, n\rangle$ and $|e_2, n-1\rangle$, as expressed by \hat{V}_0^{red} , we obtain three perturbed states $|1(n)\rangle$, $|2(n)\rangle$, $|3(n)\rangle$ (the eigenstates of \hat{V}_0^{red}), two of which are shifted up and down, respectively, in energy by $\hbar\Omega$ with $\Omega := \sqrt{\omega_1^2 + \omega_2^2}$. These states are called dressed states. In the dressed state language, this configuration can be understood as two two-state systems, the first one consisting of $|g, n\rangle$ and $|e_1, n-1\rangle$, the second one of $|g, n\rangle$ and $|e_2, n-1\rangle$. The missing coupling between $|e_1, n-1\rangle$ and $|e_2, n-1\rangle$ on the other hand, results in an energy shift of zero (state $|2(n)\rangle$) with respect to the original energies.

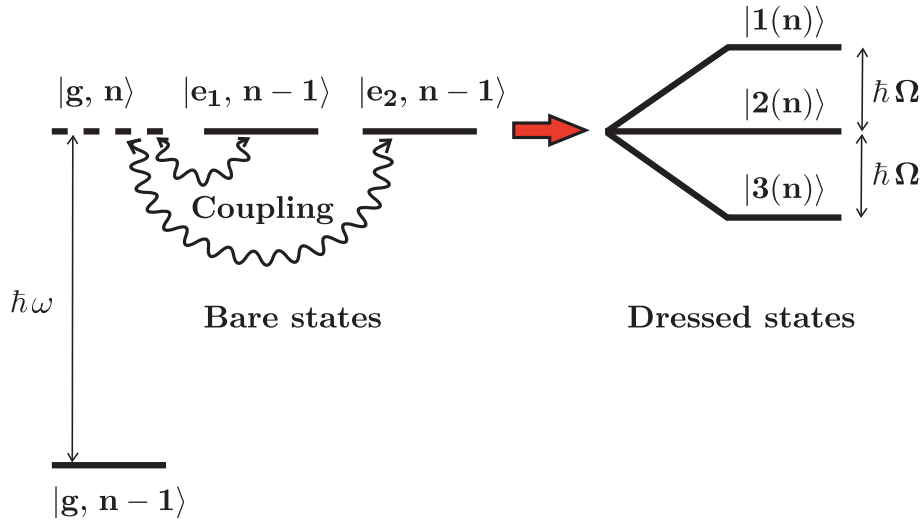


Figure 4.1: Level diagram of the qubit+field system showing the dressed states. The bare states are perturbed by the coupling encountered via absorption and induced emission, resulting in new eigenstates $|1(n)\rangle$, $|2(n)\rangle$, and $|3(n)\rangle$ (dressed states). The frequency of the field ω is resonant with the qubits' level splitting. $\hbar\Omega$ is the energy separation induced by the coupling.

In the following, we aim for exploring the dynamical behavior of the states, that is to say we derive the Rabi formula by means of our dressed state approach. We expect the probability to find the system in the state $|e_1, n-1\rangle$ ($|e_2, n-1\rangle$, respectively) after a time t if we started in the ground state $|g, n\rangle$ at time $t = 0$ to be a sinusoidal function of time, oscillating at the

¹The eigenstates of the system are supposed not to change during the short duration of the pulses. Moreover, κ_1 and κ_2 shall remain fixed during the driving process.

Bohr frequency Ω associated with the perturbed levels [33]. For resonant coupling as in our case, the Rabi frequency equals the Bohr frequency.

In the interaction picture, the time evolution of the system is governed by the perturbation and the Schrödinger equation reads

$$i\hbar \frac{\partial}{\partial t} |\psi(t)\rangle = \hat{V}_0^{\text{red}} |\psi(t)\rangle. \quad (4.27)$$

\hat{V}_0^{red} is time independent (as a result of the used dressed state approach), and we can solve (4.27) by

$$|\psi(t)\rangle = \hat{U}(t, t_0) |\psi(t_0)\rangle = e^{-\frac{i}{\hbar} \hat{V}_0^{\text{red}} (t-t_0)} |\psi(t_0)\rangle. \quad (4.28)$$

Our objective is to calculate the propagator $\hat{U}(t, t_0)$. The dressed states together with the corresponding eigenvalues read

$$|1(n)\rangle = \frac{1}{\sqrt{2}\Omega} \begin{pmatrix} \Omega \\ \omega_1 \\ \omega_2 \end{pmatrix}, \quad |2(n)\rangle = \frac{1}{\Omega} \begin{pmatrix} 0 \\ -\omega_2 \\ \omega_1 \end{pmatrix}, \quad |3(n)\rangle = \frac{1}{\sqrt{2}\Omega} \begin{pmatrix} -\Omega \\ \omega_1 \\ \omega_2 \end{pmatrix} \quad (4.29)$$

$$\lambda_1 = \hbar\Omega, \quad \lambda_2 = 0, \quad \lambda_3 = -\hbar\Omega. \quad (4.30)$$

We get (in the following we set $t_0 = 0$ without loss of generality)

$$\hat{U}(t) = \hat{T} \begin{pmatrix} e^{-i\Omega t} & 0 & 0 \\ 0 & 1 & 0 \\ 0 & 0 & e^{i\Omega t} \end{pmatrix} \hat{T}^\dagger \quad \text{with} \quad \hat{T} = (|1(n)\rangle |2(n)\rangle |1(n)\rangle). \quad (4.31)$$

The explicit form of $\hat{U}(t)$ can be found in appendix E.

Consider we start with a fully occupied ground state without any population in the excited levels. The effect of the propagator onto this initial state then looks like

$$|\psi(t)\rangle = \hat{U}(t) \begin{pmatrix} 1 \\ 0 \\ 0 \end{pmatrix} = \begin{pmatrix} \cos \Omega t \\ -i\omega_1 \frac{\sin \Omega t}{\Omega} \\ -i\omega_2 \frac{\sin \Omega t}{\Omega} \end{pmatrix}. \quad (4.32)$$

We obtain the expected sinusoidal behavior mentioned above. Complete depopulation of the ground state can be achieved by applying a π -pulse of length

$$t_\pi = \frac{\pi}{2\Omega}, \quad (4.33)$$

yielding the final state (disregarding a global phase)

$$|\psi(t_\pi)\rangle = \frac{1}{\Omega} \begin{pmatrix} 0 \\ \omega_1 \\ \omega_2 \end{pmatrix}. \quad (4.34)$$

By choosing the amplitudes of the sources κ_1 and κ_2 (and thereby the Rabi frequencies ω_1 and ω_2) appropriately, we can completely depopulate the ground state and prepare states with arbitrary amplitude ratio (in a given basis) in the degenerate subspace. Note that this

could not be achieved by a symmetric driving in ϵ ($\epsilon_1(t) = \epsilon_2(t) = \epsilon_3(t)$); the Hamiltonian \mathbf{H}_0 in (3.1) has no transition matrix elements between the ground state (living in the upper 4×4 block) and the degenerate subspaces (living in the lower 2×2 blocks).

We now want to enhance this scheme by additionally introducing a relative phase, that is preparing a target state

$$|\psi_{\text{target}}\rangle = \frac{1}{\Omega} \begin{pmatrix} 0 \\ \omega_1 \\ \omega_2 e^{i\varphi} \end{pmatrix}. \quad (4.35)$$

4.2.2 Introducing a relative phase

We assume the two microwave sources, so far just characterized by their amplitudes κ_1 and κ_2 , to be independent not only in amplitude but also in their relative phase. However, both sources shall be kept on resonance, as expressed by the condition (4.16), oscillating on the same frequency,

$$\begin{aligned} \vec{B}_1(t) &= \vec{\epsilon} B_1 \cos \omega t = \vec{\epsilon} B_1 \frac{1}{2} (e^{i\omega t} + e^{-i\omega t}), \\ \vec{B}_2(t) &= \vec{\epsilon} B_2 \cos(\omega t + \theta) = \vec{\epsilon} B_2 \frac{1}{2} (e^{i\theta} e^{i\omega t} + e^{-i\theta} e^{-i\omega t}). \end{aligned} \quad (4.36)$$

Quantization of the field introduces the creation and annihilation operators, whereas the exponentials $e^{\pm i\omega t}$ disappear for a single-mode field (in the interaction representation) [34],

$$\begin{aligned} \vec{B}_1 &= \vec{\epsilon} B_1 (a + a^\dagger), \\ \vec{B}_2 &= \vec{\epsilon} B_2 (e^{i\theta} a + e^{-i\theta} a^\dagger). \end{aligned} \quad (4.37)$$

The interaction Hamiltonian then takes the form

$$\mathbf{H}_I = g_I \frac{\kappa}{3} \left[\left\{ \begin{pmatrix} 1 \\ 1 \\ 1 \end{pmatrix} + \kappa_1 \begin{pmatrix} 1 \\ 0 \\ -1 \end{pmatrix} \right\} \vec{\sigma}(a + a^\dagger) + \kappa_2 \begin{pmatrix} 1 \\ -1 \\ 0 \end{pmatrix} \vec{\sigma}(e^{i\theta} a + e^{-i\theta} a^\dagger) \right] \quad (4.38)$$

and the reduced perturbation operator reads (cp. (4.26))

$$\begin{aligned} \hat{V}_0^{\text{red}} &= -\sqrt{\frac{2}{3}} g_I \frac{\kappa}{3} \sqrt{n} (e g_2 + \sqrt{1 - e^2} g_3) \begin{pmatrix} 0 & \sqrt{3}\kappa_1 & \kappa_1 + 2\kappa_2 e^{-i\theta} \\ \sqrt{3}\kappa_1 & 0 & 0 \\ \kappa_1 + 2\kappa_2 e^{i\theta} & 0 & 0 \end{pmatrix} = \\ &= \hbar \begin{pmatrix} 0 & \omega_1 & \omega_2 e^{-i\varphi} \\ \omega_1 & 0 & 0 \\ \omega_2 e^{i\varphi} & 0 & 0 \end{pmatrix}. \end{aligned} \quad (4.39)$$

The operator can still be written in terms of the two frequencies ω_1 and ω_2 and in addition a phase φ ; however, note that in general, ω_2 as in (4.39) is different from ω_2 as in (4.26).

Determining the propagator $\hat{U}(t) = e^{-\frac{i}{\hbar}\hat{V}_0^{\text{red}}t}$ in the same way as above and applying it to the initial ground state gives

$$|\psi(t)\rangle = \hat{U}(t) \begin{pmatrix} 1 \\ 0 \\ 0 \end{pmatrix} = \begin{pmatrix} \cos \Omega t \\ -i\omega_1 \frac{\sin \Omega t}{\Omega} \\ -i\omega_2 \frac{\sin \Omega t}{\Omega} e^{i\varphi} \end{pmatrix}. \quad (4.40)$$

The explicit form of $\hat{U}(t)$ can again be found in appendix E.

For a π -pulse of the same length as in (4.33) and disregarding a global phase we get a final state

$$|\psi(t_\pi)\rangle = \frac{1}{\Omega} \begin{pmatrix} 0 \\ \omega_1 \\ \omega_2 e^{i\varphi} \end{pmatrix}. \quad (4.41)$$

We obtain the delightful result that amplitude as well as phase can be controlled by amplitude and phase of the applied pulses. This enables us to prepare arbitrary states in the subspace. By an optimal choice of ω_1 , ω_2 and φ , states with maximized entanglement can be created (see appendix D.2). We will concentrate on these states in the following.

Chapter 5

Entanglement properties

Entanglement [35] is considered to be one of the key resources [36] in quantum information processing, lying at the heart of many striking phenomena and methods, such as quantum teleportation [37, 38] and entanglement-based approaches for secure quantum key distribution [39]. Over decades, it has therefore been the subject of much study and attention.

In quantum mechanics, a system is made up by its subsystems in a holistic way, where the states of the subsystems do in general not determine the state of the system. To each subsystem, a Hilbert space is associated, and the Hilbert space of the total system is the product of these individual Hilbert spaces, $H = \bigotimes_j H_j$. However, not all states in H are product states, i. e. they factorize into the states of the subsystems. As a result, the measurement outcomes on the subsystems (particles) show correlations that are only contained in the state of the combined system and cannot be accounted for classically. As an example, the singlet state $|\psi\rangle = \frac{1}{\sqrt{2}}(|\uparrow\downarrow\rangle - |\downarrow\uparrow\rangle)$ predicts perfect anticorrelation between the measurement outcomes on the two particles for a spin measurement along an arbitrary axis. Probably the most famous example of the baffling nature of entanglement is the violation of Bell's inequality (or Bell-type inequalities, respectively). Considering the singlet state above, the perfect anticorrelation also holds true if one separates the two particles by an arbitrarily large distance. Before a measurement on one of the particles, the two possible outcomes $|\uparrow\rangle$ and $|\downarrow\rangle$ are equally likely; however, after having measured the state of the two particles at two distant (spacelike separated) stations, one always finds the perfect anticorrelation. As this seems to impose some action at a distance, it is called *quantum nonlocality*.¹

An alternative explanation avoiding such an interaction assumes that the measurement results are determined before the measurement by the history of the particles, i.e. each particle carries a local plan preparing the particle's answer on a certain type of measurement (*local realism*). If such a local plan in the form of hidden variables would exist, a theory not including these variables would be incomplete. In this fashion, the incompleteness of quantum mechanics was claimed by Einstein, Podolsky and Rosen (EPR) in their famous 1935 paper [40].

However, the statistical predictions of quantum mechanics regarding measurements performed on different axes are different from the predictions made by hidden variable theories. These differences can be expressed in terms of inequalities for expectation values of certain measurements, called *Bell inequalities* [41], which are violated if quantum mechanics holds true.

¹However, the observers at the stations cannot exchange information as they cannot affect the probabilities of each others' results. Both of them see the two possible outcomes of their individual measurements occur with probability 1/2, regardless of what the other observer chose to measure.

These inequalities are experimentally testable and have been tested [42, 43, 44, 45].

5.1 Tripartite entanglement

Despite the great importance of entanglement, a necessary and sufficient condition for the entanglement of a given state is only known for two-qubit systems [46]. The determination of entanglement for multipartite states, however, is an open question. For three qubits it was shown in Ref. [47] that two different kinds of *genuine* multipartite entanglement (i.e. each party is entangled with each other party) can occur. Namely, each tripartite entangled state can (with nonzero probability) be converted² by LOCC [48] to either one of two standard forms, the GHZ state, $|\text{GHZ}\rangle = \frac{1}{\sqrt{2}}(|\uparrow\uparrow\uparrow\rangle + |\downarrow\downarrow\downarrow\rangle)$ [49], or the W state, $|\text{W}\rangle = \frac{1}{\sqrt{3}}(|\uparrow\uparrow\downarrow\rangle + |\uparrow\downarrow\uparrow\rangle + |\downarrow\uparrow\uparrow\rangle)$, which are mutually unrelated under LOCC. For GHZ-like entanglement, a measure was invented [50], the *3-tangle* τ . It allows for a reliable distinction between the two classes of entanglement, as it is zero for all W-type states (and all separable states, of course), whereas it is greater than zero for all states in the GHZ class. An expression for τ in terms of the coefficients of the state in the standard basis is given in appendix D.1. A tool for detection of any kind of genuine tripartite entanglement for arbitrary states is not at hand; however, if some knowledge about the state under investigation is provided, *entanglement witnesses* (EW) can be used [51, 52]. These are observables with a positive expectation value for all (bi-)separable states (in general $n-1$ partite entangled states), whereas a negative expectation value indicates the presence of tripartite (n -partite) entanglement³. The common way to construct an EW for a state $|\psi\rangle$ is

$$\mathcal{W} = \alpha \mathbb{1} - |\psi\rangle\langle\psi|, \quad (5.1)$$

where α is the maximal squared overlap of $|\psi\rangle$ with any biseparable or fully separable state. Determination of α is in general complicated⁴, but we can use the proximity of the states under investigation (as described in 3.3.2 and 3.4) to W and GHZ states, respectively, to make use of known values for α . In order to measure EWs, they must be decomposed into a sum of local measurements. This as well is a demanding task and we will again refer to previous work done on this topic [55, 56, 57].

5.1.1 Entanglement of state $|E_3\rangle$

As pointed out in 3.4.1, $|E_3\rangle$ is for zero energy bias close to $|\text{GHZ}\rangle = \frac{1}{\sqrt{2}}(|\uparrow\uparrow\uparrow\rangle + |\downarrow\downarrow\downarrow\rangle)$. For constructing a GHZ witness adapted to $|E_3\rangle$, the maximal squared overlap of $|E_3\rangle$ with non-GHZ entangled states is required, though not known. We therefore choose an EW suitable for detecting the state $|\text{GHZ}\rangle$ for which α is known ($\alpha = 3/4$) and thus make use of the proximity of $|E_3\rangle$ to $|\text{GHZ}\rangle$. However, instead of using the EW [58]

$$\widetilde{\mathcal{W}}_{\text{GHZ}} = \frac{3}{4} \mathbb{1} - |\text{GHZ}\rangle\langle\text{GHZ}|, \quad (5.2)$$

²No operational criterion for the existence of such a transformation between two given states is known.

³The object of study here is tripartite entanglement. However, the concept of entanglement witnesses applies to multipartite entanglement as well.

⁴Since one has to minimize over all product states, i.e. over a convex hull of states, numerical calculations involving the theory of convex optimization are commonly used [52, 53, 54].

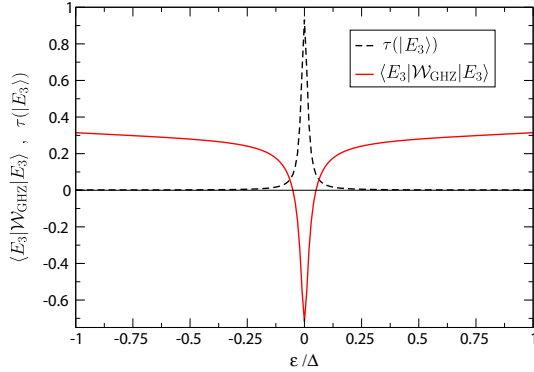


Figure 5.1: 3-tangle and expectation value of the GHZ witness \mathcal{W}_{GHZ} (explicit form in the text) for the state $|E_3\rangle$. As can be seen, both quantities indicate a strong GHZ-like entanglement around $\epsilon = 0$.

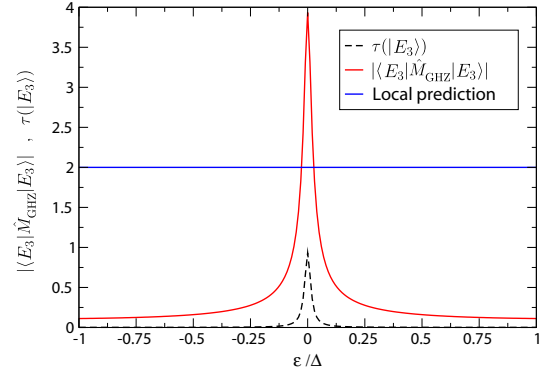


Figure 5.2: 3-tangle and expectation value of the Bell operator \hat{M}_{GHZ} (explicit form in the text) for the state $|E_3\rangle$. The high 3-tangle coincides with a significant violation of the Bell inequality.

we apply an EW introduced in Ref. [57], which can be measured with two collective local measurement settings,

$$\mathcal{W}_{\text{GHZ}} = \frac{7}{4} \mathbb{1} - \hat{\sigma}_x^{\otimes 3} - \frac{1}{2} [\hat{\sigma}_z \hat{\sigma}_z \mathbb{1} + \hat{\sigma}_z \mathbb{1} \hat{\sigma}_z + \mathbb{1} \hat{\sigma}_z \hat{\sigma}_z]. \quad (5.3)$$

The two local settings here are the $\{\hat{\sigma}_x^{(1)}, \hat{\sigma}_x^{(2)}, \hat{\sigma}_x^{(3)}\}$ and the $\{\hat{\sigma}_z^{(1)}, \hat{\sigma}_z^{(2)}, \hat{\sigma}_z^{(3)}\}$ setting. From these, all correlators appearing in (5.3) can be computed. In contrast, the EW $\widetilde{\mathcal{W}}_{\text{GHZ}}$ requires four measurement settings (see table 5.1).

The 3-tangle $\tau(|E_3\rangle)$ and the expectation value $\langle E_3 | \mathcal{W}_{\text{GHZ}} | E_3 \rangle$ for varying energy bias are shown in figure 5.1. Both quantities indicate a strong (cp. limiting case: $\tau_{\text{max}} = \tau(|\text{GHZ}\rangle) = 1$, $\langle \mathcal{W}_{\text{GHZ}} \rangle_{\text{min}} = \langle \text{GHZ} | \mathcal{W}_{\text{GHZ}} | \text{GHZ} \rangle = -3/4$) tripartite entanglement of GHZ type in a narrow range around zero energy bias (here, only $|E_3\rangle$ is plotted, $|E_4\rangle$ shows the same behavior). The range of negative expectation value for \mathcal{W}_{GHZ} is even a little smaller than the range of non-zero 3-tangle. This reflects the fact that EWs need to be adapted to the state under investigation and can take positive expectation value even if the associated entanglement is present. In section 5.2, we will comment on the violation of Bell inequality as displayed in figure 5.2.

5.1.2 Entanglement of state $|E_2\rangle$

More GHZ-like states can be found among the eigenstates. In figure 5.3, the 3-tangle $\tau(|E_2\rangle)$ and the expectation values for two EWs $\langle E_2 | \mathcal{W}_{\text{GHZ}}^{(1)} | E_2 \rangle$ and $\langle E_2 | \mathcal{W}_{\text{GHZ}}^{(2)} | E_2 \rangle$ for varying energy bias are displayed. We obtain a strong (limiting case: $\langle \mathcal{W}_{\text{GHZ}}^{(1)} \rangle_{\text{min}} = \langle \mathcal{W}_{\text{GHZ}}^{(2)} \rangle_{\text{min}} = -1/4$) entanglement for a finite energy bias $\epsilon \approx \pm 2.6\Delta$ and a high residual entanglement in the range between these two maxima.

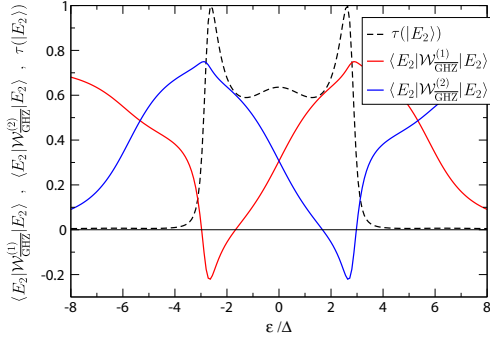


Figure 5.3: 3-tangle and expectation value of the GHZ witnesses $\mathcal{W}_{\text{GHZ}}^{(1)}$ and $\mathcal{W}_{\text{GHZ}}^{(2)}$ for the state $|E_2\rangle$. For finite energy bias $\epsilon \approx \pm 2.6\Delta$, we find a peaking 3-tangle as well as negative expectation value for the two GHZ witnesses, indicating entanglement of the GHZ class. Moreover, the entanglement is more robust to detuning of the energy bias compared to the situation for $|E_3\rangle$.

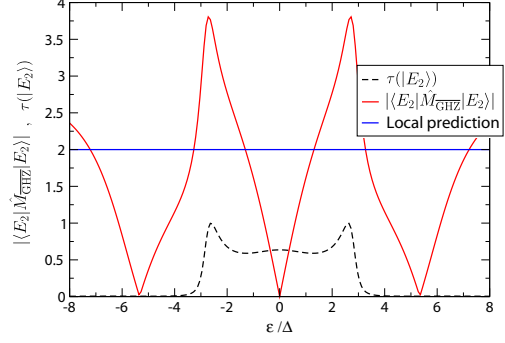


Figure 5.4: 3-tangle and expectation value of the Bell operator \hat{M}_{GHZ} for the state $|E_2\rangle$. A significant violation of the corresponding Bell inequality over a relatively large range of ϵ can be observed.

Left maximum at $\epsilon \approx -2.6\Delta$

The explicit form of the state constituting the left maximum is

$$|E_2^{(1)}\rangle = -\alpha\{|\uparrow\uparrow\downarrow\rangle + |\uparrow\downarrow\uparrow\rangle + |\downarrow\uparrow\uparrow\rangle - |\downarrow\downarrow\downarrow\rangle\} + \beta\{|\downarrow\downarrow\uparrow\rangle + |\downarrow\uparrow\downarrow\rangle + |\uparrow\downarrow\downarrow\rangle - |\uparrow\uparrow\uparrow\rangle\}, \quad (5.4)$$

where $\alpha \approx 0.5$, $\beta \approx 0.09$.

Thus, this state is close to the state

$$|\overline{\text{GHZ}}\rangle = \frac{1}{2}(|\uparrow\uparrow\downarrow\rangle + |\uparrow\downarrow\uparrow\rangle + |\downarrow\uparrow\uparrow\rangle - |\downarrow\downarrow\downarrow\rangle) = \frac{1}{\sqrt{2}}(|\bar{0}\bar{0}\bar{0}\rangle + |\bar{1}\bar{1}\bar{1}\rangle) \quad (5.5)$$

with $|\bar{0}\rangle = (|\uparrow\rangle + i|\downarrow\rangle)/\sqrt{2}$ and $|\bar{1}\rangle = -(|\uparrow\rangle - i|\downarrow\rangle)/\sqrt{2}$.

The LOCC transformation

$$\hat{U}_{E_2}^{(1)} |\overline{\text{GHZ}}\rangle = |\text{GHZ}\rangle \quad (5.6)$$

onto the state $|\text{GHZ}\rangle$ has the form

$$\hat{U}_{E_2}^{(1)} = e^{i\pi/4} \left\{ \hat{R}_x(-\pi/2) \hat{R}_z(-\pi) \hat{R}_y(\pi/2) \right\}^{\otimes 3}. \quad (5.7)$$

The EW is chosen such as to detect tripartite entanglement in the proximity of $|\overline{\text{GHZ}}\rangle$ [56],

$$\mathcal{W}_{\text{GHZ}}^{(1)} = \frac{3}{4} \mathbb{1} - |\overline{\text{GHZ}}\rangle\langle\overline{\text{GHZ}}| = \frac{3}{4} \mathbb{1} - \hat{U}_{E_2}^{(1)\dagger} |\text{GHZ}\rangle\langle\text{GHZ}| \hat{U}_{E_2}^{(1)}. \quad (5.8)$$

For an optimal decomposition of $\mathcal{W}_{\text{GHZ}}^{(1)}$ refer to table 5.1.

Right maximum at $\epsilon \approx 2.6\Delta$

For the state in the right maximum we find

$$|E_2^{(2)}\rangle = \alpha\{|\downarrow\downarrow\uparrow\rangle + |\downarrow\uparrow\downarrow\rangle + |\uparrow\downarrow\downarrow\rangle - |\uparrow\uparrow\uparrow\rangle\} - \beta\{|\uparrow\uparrow\downarrow\rangle + |\uparrow\downarrow\uparrow\rangle + |\downarrow\uparrow\uparrow\rangle - |\downarrow\downarrow\downarrow\rangle\} \quad (5.9)$$

with α and β as above. $|E_2^{(2)}\rangle$ is the totally flipped counterpart to $|E_2^{(1)}\rangle$ and therefore shows the same behavior after being flipped back by $\hat{R}_x(-\pi)^{\otimes 3}$,

$$\hat{U}_{E_2}^{(2)}|E_2^{(2)}\rangle \approx |\text{GHZ}\rangle \quad \text{with} \quad \hat{U}_{E_2}^{(2)} = \hat{U}_{E_2}^{(1)} \hat{R}_x(-\pi)^{\otimes 3}. \quad (5.10)$$

The corresponding EW looks like

$$\mathcal{W}_{\text{GHZ}}^{(2)} = \hat{R}_x(\pi)^{\otimes 3} \mathcal{W}_{\text{GHZ}}^{(1)} \hat{R}_x(-\pi)^{\otimes 3}. \quad (5.11)$$

The optimal decomposition of $\mathcal{W}_{\text{GHZ}}^{(2)}$ can again be looked up in table 5.1.

Whereas the behavior of the highest excited states $|E_3\rangle$ and $|E_4\rangle$ for vanishing energy bias as described above was expected, we make the surprising observation—referring to figure 5.3—of the existence of GHZ entangled states also in the parameter regime of finite energy bias. Moreover, the entanglement shown by $|E_2\rangle$ is more stable to deviations from the optimal energy bias than the one of $|E_3\rangle$, overcoming a major drawback caused by the antiferromagnetic nature of the coupling.

5.1.3 Entanglement in the degenerate subspaces

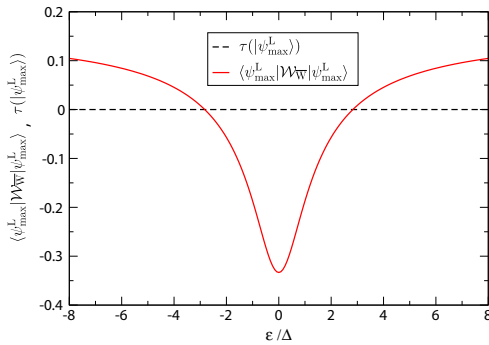


Figure 5.5: 3-tangle and expectation value of the W witness $\mathcal{W}_{\overline{W}}$ (explicit form in the text) for the state $|\psi_{\text{max}}^L\rangle$. The vanishing 3-tangle excludes entanglement of the GHZ type, whereas the negative expectation value of the W witness indicates a W type entanglement.

In figure 5.5, the 3-tangle and the expectation value of the EW $\langle\psi_{\text{max}}^L|\mathcal{W}_{\overline{W}}|\psi_{\text{max}}^L\rangle$ for the maximally entangled superposition $|\psi_{\text{max}}^L\rangle$ in the low-energy subspace is displayed (corresponding behavior for $|\psi_{\text{max}}^H\rangle$ —not shown separately).

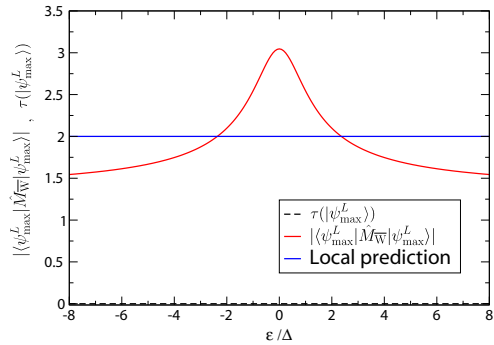


Figure 5.6: 3-tangle and expectation value of the Bell operator $\hat{M}_{\overline{W}}$ (explicit form in the text) for the state $|\psi_{\text{max}}^L\rangle$. The maximal violation of the Bell inequality for the W-equivalent state is not as high as for the GHZ-equivalent states above, however, the violation persists over a large range of ϵ .

Because we know that $|\psi_{\max}^L\rangle$ ($= |E_5\rangle$) is equivalent under LOCC to the W state (see 3.3.2), we can construct an EW making use of the known maximal overlap ($\alpha = 2/3$ [58]) between the W state (and therefore the state $|\psi_{\max}^L\rangle$) and biseparable states,

$$\mathcal{W}_{\overline{W}} = \frac{2}{3} \mathbb{1} - |\psi_{\max}^L\rangle\langle\psi_{\max}^L|. \quad (5.12)$$

Its expectation value is positive on biseparable and fully separable states. It thus detects genuine tripartite entanglement in general, without distinguishing between entanglement of the W and the GHZ class. However, in connection with the 3-tangle, a distinction can be achieved, stating an entanglement of the W type in a large range for ϵ .

Reviewing the results of this section, we were able to find states with either kind of genuine tripartite entanglement, GHZ type as well as W type.

EW	Local decomposition
$\widetilde{\mathcal{W}}_{\text{GHZ}}$	$= \frac{1}{8} [5 \cdot \mathbb{1}^{\otimes 3} - 2 \hat{\sigma}_x^{\otimes 3} - \hat{\sigma}_z \hat{\sigma}_z \mathbb{1} - \hat{\sigma}_z \mathbb{1} \hat{\sigma}_z - \mathbb{1} \hat{\sigma}_z \hat{\sigma}_z + \frac{1}{2} (\hat{\sigma}_x + \hat{\sigma}_y)^{\otimes 3} + \frac{1}{2} (\hat{\sigma}_x - \hat{\sigma}_y)^{\otimes 3}]$
\mathcal{W}_{GHZ}	$= \frac{7}{4} \mathbb{1} - \hat{\sigma}_x^{\otimes 3} - \frac{1}{2} [\hat{\sigma}_z \hat{\sigma}_z \mathbb{1} + \hat{\sigma}_z \mathbb{1} \hat{\sigma}_z + \mathbb{1} \hat{\sigma}_z \hat{\sigma}_z]$
$\mathcal{W}_{\text{GHZ}}^{(1)}$	$= \frac{1}{16} [10 \cdot \mathbb{1}^{\otimes 3} + 4 \hat{\sigma}_z^{\otimes 3} - 2(\hat{\sigma}_y \hat{\sigma}_y \mathbb{1} + \hat{\sigma}_y \mathbb{1} \hat{\sigma}_y + \mathbb{1} \hat{\sigma}_y \hat{\sigma}_y) - (\hat{\sigma}_z + \hat{\sigma}_x)^{\otimes 3} - (\hat{\sigma}_z - \hat{\sigma}_x)^{\otimes 3}]$
$\mathcal{W}_{\text{GHZ}}^{(2)}$	$= \frac{1}{16} [10 \cdot \mathbb{1}^{\otimes 3} - 4 \hat{\sigma}_z^{\otimes 3} - 2(\hat{\sigma}_y \hat{\sigma}_y \mathbb{1} + \hat{\sigma}_y \mathbb{1} \hat{\sigma}_y + \mathbb{1} \hat{\sigma}_y \hat{\sigma}_y) + (\hat{\sigma}_z - \hat{\sigma}_x)^{\otimes 3} + (\hat{\sigma}_z + \hat{\sigma}_x)^{\otimes 3}]$
$\mathcal{W}_{\overline{W}}$	$= \frac{1}{24} [17 \cdot \mathbb{1}^{\otimes 3} - 7 \hat{\sigma}_x^{\otimes 3} - 3(\hat{\sigma}_x \mathbb{1} \mathbb{1} + \mathbb{1} \hat{\sigma}_x \mathbb{1} + \mathbb{1} \mathbb{1} \hat{\sigma}_x) + 5(\hat{\sigma}_x \hat{\sigma}_x \mathbb{1} + \hat{\sigma}_x \mathbb{1} \hat{\sigma}_x + \mathbb{1} \hat{\sigma}_x \hat{\sigma}_x) -$ $-(\mathbb{1} - \hat{\sigma}_x + \hat{\sigma}_z) \otimes (\mathbb{1} - \hat{\sigma}_x - \frac{\sqrt{3}}{2} \hat{\sigma}_y - \frac{1}{2} \hat{\sigma}_z) \otimes (\mathbb{1} - \hat{\sigma}_x + \frac{\sqrt{3}}{2} \hat{\sigma}_y - \frac{1}{2} \hat{\sigma}_z) -$ $-(\mathbb{1} - \hat{\sigma}_x - \hat{\sigma}_z) \otimes (\mathbb{1} - \hat{\sigma}_x + \frac{\sqrt{3}}{2} \hat{\sigma}_y + \frac{1}{2} \hat{\sigma}_z) \otimes (\mathbb{1} - \hat{\sigma}_x - \frac{\sqrt{3}}{2} \hat{\sigma}_y + \frac{1}{2} \hat{\sigma}_z) -$ $-(\mathbb{1} - \hat{\sigma}_x + \hat{\sigma}_y) \otimes (\mathbb{1} - \hat{\sigma}_x - \frac{1}{2} \hat{\sigma}_y + \frac{\sqrt{3}}{2} \hat{\sigma}_z) \otimes (\mathbb{1} - \hat{\sigma}_x - \frac{1}{2} \hat{\sigma}_y - \frac{\sqrt{3}}{2} \hat{\sigma}_z) -$ $-(\mathbb{1} - \hat{\sigma}_x - \hat{\sigma}_y) \otimes (\mathbb{1} - \hat{\sigma}_x + \frac{1}{2} \hat{\sigma}_y - \frac{\sqrt{3}}{2} \hat{\sigma}_z) \otimes (\mathbb{1} - \hat{\sigma}_x + \frac{1}{2} \hat{\sigma}_y + \frac{\sqrt{3}}{2} \hat{\sigma}_z)]$

Table 5.1: Local decomposition of the entanglement witnesses used above. The decomposition for $\widetilde{\mathcal{W}}_{\text{GHZ}}$ (shown to be optimal in [58]) requires four collective measurement settings in contrast to the two settings needed for \mathcal{W}_{GHZ} [57]. The optimal decomposition for $\mathcal{W}_{\text{GHZ}}^{(1)}$ can be found in Ref. [56] (five settings), the one for $\mathcal{W}_{\text{GHZ}}^{(2)}$ (five settings) was computed by rotating the individual Pauli operators occurring in $\mathcal{W}_{\text{GHZ}}^{(1)}$ according to $\hat{R}_x(\pi)$, $\mathcal{W}_{\text{GHZ}}^{(2)} = \hat{R}_x(\pi)^{\otimes 3} \mathcal{W}_{\text{GHZ}}^{(1)} \hat{R}_x(-\pi)^{\otimes 3}$. The decomposition for $\mathcal{W}_{\overline{W}}$ (five settings) was obtained similarly from the optimized decomposition $\mathcal{W}_{\overline{W}}^{(1)}$ (five settings) derived in Ref. [55], $\mathcal{W}_{\overline{W}} = \hat{U}^L \dagger \mathcal{W}_{\overline{W}}^{(1)} \hat{U}^L$.

5.2 Bell inequalities

Multiqubit states can contradict local realistic models in a new and stronger way than two-qubit states. For GHZ states, the construction of local plans mimicking the total anticorrelation (along an arbitrary axis) predicted by the state is not even possible anymore [49, 59, 60].

The concept of locality therefore breaks down at an earlier stage, giving rise to a refutation by quantum mechanics that is no longer statistical but can rather be accomplished by a single run, i.e. the explanation required by the data accumulated by a series of experiments is not refuted by the statistics of the data obtained in another long series of runs but by the outcome of a single crucial run [60]. However, the actual data obtained by a realistic experiment with realistic detectors would reveal less than perfect correlations, making the original GHZ reasoning not feasible for an experimental verification. To face this problem, N -particle Bell inequalities have been proposed [61, 62, 63], which involve pairs of settings at each of the measurement stations. These works have shown that the predictions made by quantum mechanics for the GHZ state violate these inequalities by a factor that grows exponentially with N . Thereby systems capable of showing entanglement of the GHZ type might provide an interesting way to test the hypothesis of local hidden variables⁵.

5.2.1 State $|E_3\rangle$

We use a Bell operator similar to one proposed by Mermin [61],

$$\hat{M}_{\text{GHZ}} = \frac{1}{2i} \left(\prod_{j=1}^3 (\hat{\sigma}_y^j + i\hat{\sigma}_x^j) - \prod_{j=1}^3 (\hat{\sigma}_y^j - i\hat{\sigma}_x^j) \right) = \hat{\sigma}_y \hat{\sigma}_y \hat{\sigma}_x + \hat{\sigma}_y \hat{\sigma}_x \hat{\sigma}_y + \hat{\sigma}_x \hat{\sigma}_y \hat{\sigma}_y - \hat{\sigma}_x \hat{\sigma}_x \hat{\sigma}_x . \quad (5.13)$$

The Bell inequality, i.e. the local prediction for $\langle \hat{M}_{\text{GHZ}} \rangle$ reads

$$\langle \psi | \hat{M}_{\text{GHZ}} | \psi \rangle \leq 2 \quad \forall |\psi\rangle , \quad (5.14)$$

whereas quantum mechanics states a maximal value of

$$\langle \text{GHZ} | \hat{M}_{\text{GHZ}} | \text{GHZ} \rangle = 4 . \quad (5.15)$$

In Fig. 5.2, the violation of (5.14) by $|E_3\rangle$ is displayed. Again, we find the violation to occur only in a small range around zero energy bias, however the height of the violation confirms the almost perfect overlap of $|E_3\rangle$ (at $\epsilon = 0$) with the ideal GHZ state.

5.2.2 State $|E_2\rangle$

Making use of the equivalency of $|E_2^{(1,2)}\rangle$ with $|\text{GHZ}\rangle$ mediated by $\hat{U}_{E_2}^{(1,2)}$, we use a modified Bell operator,

$$\hat{M}_{\text{GHZ}} = \hat{U}_{E_2}^{(2)\dagger} \hat{M}_{\text{GHZ}} \hat{U}_{E_2}^{(2)} = \hat{\sigma}_x \hat{\sigma}_x \hat{\sigma}_z + \hat{\sigma}_x \hat{\sigma}_z \hat{\sigma}_x + \hat{\sigma}_z \hat{\sigma}_x \hat{\sigma}_x - \hat{\sigma}_z \hat{\sigma}_z \hat{\sigma}_z . \quad (5.16)$$

We again find (Fig. 5.4) a significant violation of the local prediction located at the points of maximal 3-tangle (and minimal expectation value of the EW). Although being not as strong as for $|E_3\rangle$, this violation might –due to its smaller sensitivity to energy bias deviations– be more promising in terms of feasibility of preparation and measurement.

⁵Obviously, quantum nonlocality can only arise in the entanglement of remote systems. The violation of Bell inequalities as sign for non-classical correlations is nevertheless highly substantial as an ingredient to quantum information processing.

5.2.3 Degenerate subspace

We again aim for investigating the properties of $|\psi_{\max}^L\rangle$. For constructing an appropriate Bell operator $\hat{M}_{\overline{W}}$, we first need the Bell operator \hat{M}_W for the common representation of the W state $|W\rangle$ and then adapt it by applying the local operation \hat{U}^L .

In general, Bell inequalities for three qubits are constructed from the correlator

$$E(\mathbf{a}, \mathbf{b}, \mathbf{c}) = \langle \psi | (\mathbf{a} \cdot \vec{\sigma}) \otimes (\mathbf{b} \cdot \vec{\sigma}) \otimes (\mathbf{c} \cdot \vec{\sigma}) | \psi \rangle . \quad (5.17)$$

$\mathbf{a}, \mathbf{b}, \mathbf{c}$ are real three-dimensional normalized vectors, which define a rotation of the Pauli matrices $\vec{\sigma} = (\hat{\sigma}_x, \hat{\sigma}_y, \hat{\sigma}_z)$. A Bell operator is then given by

$$\hat{M} = E(\mathbf{a}, \mathbf{b}, \mathbf{c}') + E(\mathbf{a}, \mathbf{b}', \mathbf{c}) + E(\mathbf{a}', \mathbf{b}, \mathbf{c}) - E(\mathbf{a}', \mathbf{b}', \mathbf{c}') . \quad (5.18)$$

In order to obtain an optimal Bell operator for a given state, one can optimize over the six unit vectors $\mathbf{a}, \mathbf{a}', \mathbf{b}, \mathbf{b}', \mathbf{c}$ and \mathbf{c}' [64, 65]. The two Bell operators \hat{M}_{GHZ} and $\hat{M}_{\overline{\text{GHZ}}}$ introduced above are in this sense optimal choices for the states $|\text{GHZ}\rangle$ and $|\overline{\text{GHZ}}\rangle$.

The optimal values as obtained by a numerical optimization for \hat{M}_W adapted the state $|W\rangle$ are listed in table 5.2.

a_1	0.318053	a'_1	-0.635515	b_1	0.635515	b'_1	0.318052	c_1	0.635515	c'_1	0.318053
a_2	0.250811	a'_2	-0.501155	b_2	0.501155	b'_2	0.250810	c_2	0.501154	c'_2	0.250810
a_3	0.914296	a'_3	-0.587337	b_3	-0.587336	b'_3	0.914296	c_3	-0.587338	c'_3	0.914296

Table 5.2: Entries of the vectors $\mathbf{a}, \mathbf{a}', \mathbf{b}, \mathbf{b}', \mathbf{c}$ and \mathbf{c}' for the Bell operator \hat{M}_W [66]. In connection with (5.17) and (5.18), the explicit form of \hat{M}_W can be determined.

The Bell operator for the state $|\psi_{\max}^L\rangle$ then reads

$$\hat{M}_{\overline{W}} = \hat{U}^{L\dagger} \hat{M}_W \hat{U}^L . \quad (5.19)$$

The violation of the Bell inequality as displayed in Fig. 5.6 approaches for $\epsilon = 0$ the theoretical maximum for a W state of $\langle M_{\overline{W}} \rangle \approx 3.05$. Moreover, it persists over a large range of ϵ which even noticeably exceeds the observed range for $|E_2\rangle$.

5.3 Robustness to limited measurement fidelity

Any experimental test of tripartite entanglement or the violation of Bell inequalities involving three qubits will be more fragile than a two particle test and will be put in jeopardy by detector imperfections (as three-party correlations need to be measured in either case, the measurement fidelity enters –roughly spoken– with the power of three) and fabrication issues of the sample preparation. However, concerning Bell inequalities, the stronger violation that is possible with three particles might compensate for that. We will investigate the effect of a limited measurement fidelity $f < 1$ on the expectation values of the EWs and Bell operators introduced above and compare the results to a representative two-particle case. We model a non-perfect measurement of a spin component $\hat{\sigma}_i$ by the perfect measurement of a spin

component $\hat{\sigma}'_i$ which yields the correct measurement result with a probability f , whereas a '1' is measured otherwise,

$$\hat{\sigma}'_i = f \hat{\sigma}_i + (1 - f) \mathbb{1}. \quad (5.20)$$

In the following, the results for the aforementioned parameter regimes are plotted.

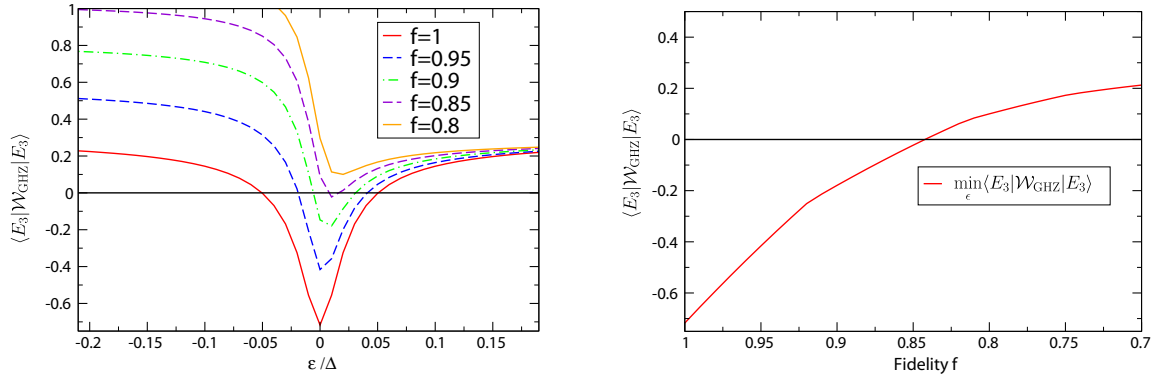


Figure 5.7: Left: Expectation value of GHZ witness \mathcal{W}_{GHZ} for several measurement fidelities for $|E_3\rangle$. Right: Minimal expectation value of \mathcal{W}_{GHZ} vs. fidelity. The absolute lower limit for the measurement fidelity in order to detect tripartite entanglement with \mathcal{W}_{GHZ} is $f_{\min} \approx 84.3\%$.

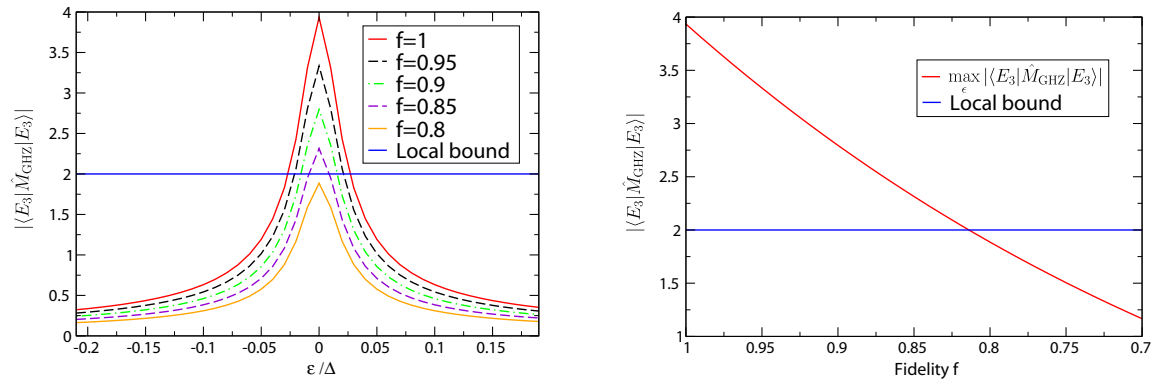


Figure 5.8: Left: Expectation value of Bell operator \hat{M}_{GHZ} for several measurement fidelities for $|E_3\rangle$. Right: Maximal violation of Bell inequality vs. fidelity. The absolute lower limit for the measurement fidelity in order to detect nonlocality with \hat{M}_{GHZ} is $f_{\min} \approx 81.4\%$.

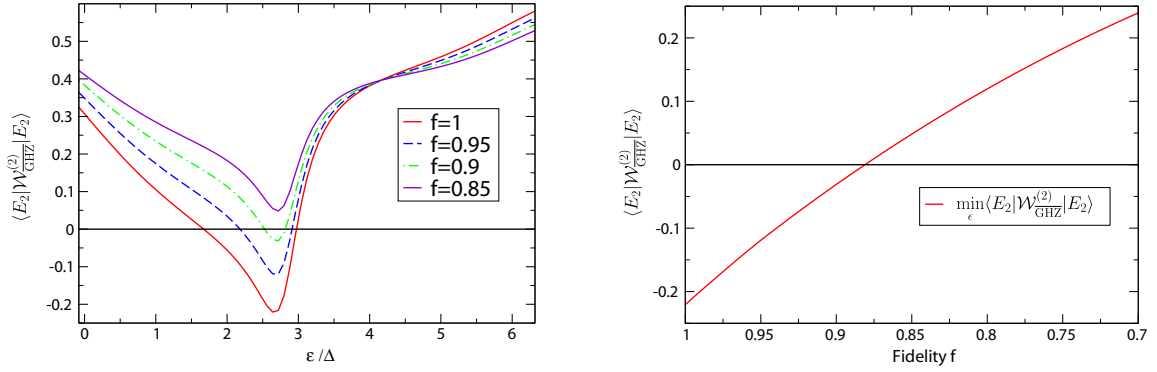


Figure 5.9: Left: Expectation value of GHZ witness $\mathcal{W}_{\text{GHZ}}^{(2)}$ for several measurement fidelities for $|E_2\rangle$. Right: Minimal expectation value of $\mathcal{W}_{\text{GHZ}}^{(2)}$ vs. fidelity. The absolute lower limit for the measurement fidelity in order to detect tripartite entanglement with $\mathcal{W}_{\text{GHZ}}^{(2)}$ is $f_{\min} \approx 88.2\%$. Only the range of positive energy bias is displayed, corresponding to the right minimum in Fig. 5.3.

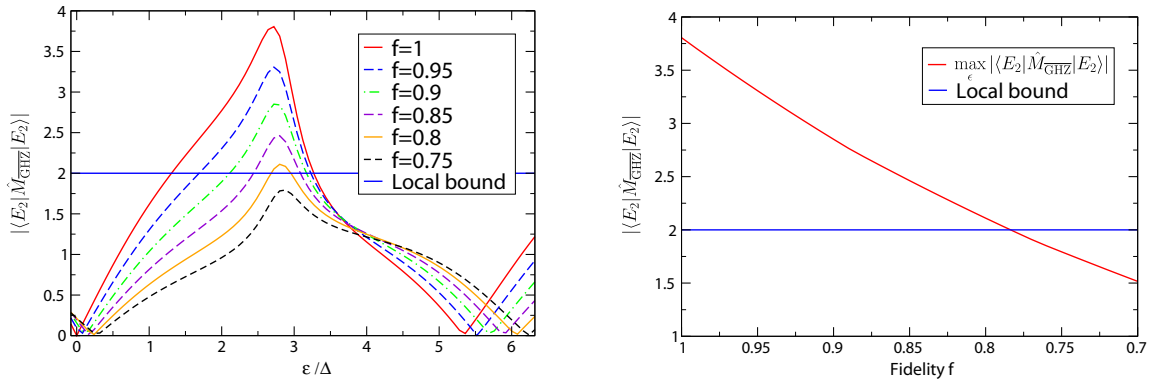


Figure 5.10: Left: Expectation value of Bell operator \hat{M}_{GHZ} for several measurement fidelities for $|E_2\rangle$. Right: Maximal violation of Bell inequality vs. fidelity. The absolute lower limit for the measurement fidelity in order to detect nonlocality with \hat{M}_{GHZ} is $f_{\min} \approx 78.4\%$. Only the range of positive energy bias is displayed, corresponding to the right maximum in Fig. 5.4.

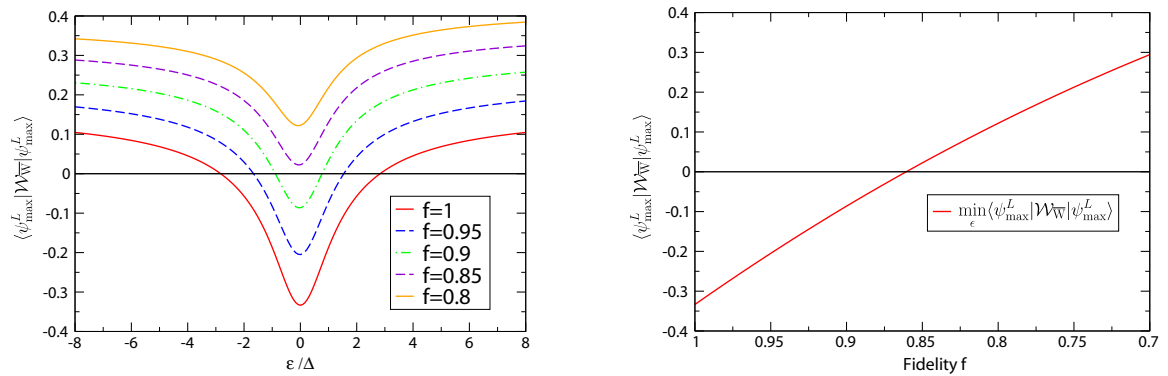


Figure 5.11: Left: Expectation value of W witness $\mathcal{W}_{\overline{W}}$ for several measurement fidelities for $|\psi_{\max}^L\rangle$. Right: Minimal expectation value of $\mathcal{W}_{\overline{W}}$ vs. fidelity. The absolute lower limit for the measurement fidelity in order to detect tripartite entanglement with $\mathcal{W}_{\overline{W}}$ is $f_{\min} \approx 86.1\%$.

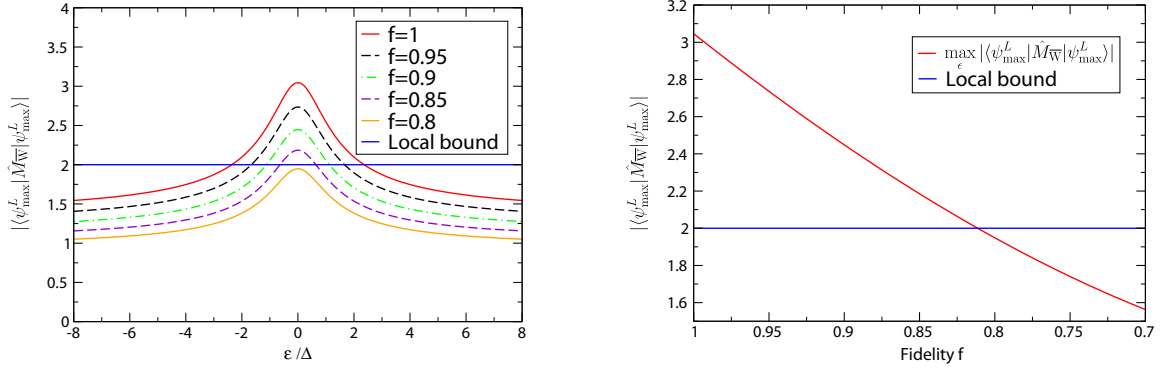


Figure 5.12: Left: Expectation value of Bell operator $\hat{M}_{\overline{W}}$ for several measurement fidelities for $|\psi_{\max}^L\rangle$. Right: Maximal violation of Bell inequality vs. fidelity. The absolute lower limit for the measurement fidelity in order to detect nonlocality with $\hat{M}_{\overline{W}}$ is $f_{\min} \approx 81.2\%$.

In Tab. 5.3, the minimal detector fidelities for the detection of tripartite entanglement or violation of Bell inequalities using the aforementioned operators are compared. Moreover, the required fidelity for the violation of the CHSH inequality (named after *Clouser-Horne-Shimony-Holt* [67]) by a bell pair $|\psi\rangle = \frac{1}{\sqrt{2}}(|\uparrow\downarrow\rangle - |\downarrow\uparrow\rangle)$ is listed. Evidently, the fidelity needed to detect nonlocal three-party correlations via the Bell inequalities introduced above lies even slightly below the one required for falsifying the CHSH inequality. The requested measurement fidelity is already available for charge qubits, where significant progress has recently been achieved with dispersive readout⁶ inside a cavity, providing a visibility of more than 90% [27]. A similar design has been proposed for flux qubits [68]. Moreover, other experiments based on Josephson junction technology indicating similar fidelities have been performed [28, 29, 69, 70].

Operator	f_{\min}	Operator	f_{\min}
\mathcal{W}_{GHZ}	84.3%	\hat{M}_{GHZ}	81.4%
$\mathcal{W}_{\text{GHZ}}^{(2)}$	88.2%	$\hat{M}_{\overline{\text{GHZ}}}$	78.4%
$\mathcal{W}_{\overline{W}}$	86.1%	$\hat{M}_{\overline{W}}$	81.2%
		\hat{M}_{CHSH}	$\frac{2}{1+\sqrt{2}} \approx 82.8\%$

Table 5.3: Minimal detector fidelities for the detection of tripartite entanglement or violation of Bell inequalities, respectively.

⁶i.e. the shift in resonance frequency of a resonator coupled to the system

Chapter 6

Pulse shaping

In the previous chapters, properties of the eigenstates of the system were discussed. Although the system will naturally occupy its ground state after some time, the population of higher excited eigenstates can be achieved by applying resonant π -pulses. Here, the relevant parameter is the area under the pulse in the time domain. A higher pulse amplitude leads to a larger Rabi frequency, thereby transferring the system to the desired state more quickly (4.33). In this driving scheme, the shape of the pulses –i.e. the envelope of the amplitude– is in principle irrelevant (as long as the rotating wave approximation is still valid, i.e. the linewidth is much smaller than the transition frequency). However, facing the challenges given by the short decoherence times in solid state systems, short pulse times are crucial to preserve the quantum properties of the system over the duration of the pulses. In addition, whenever one has to deal with additional time scales, as –for example– given by the coupling between qubits in the realization of quantum gates or the preparation of arbitrary non-eigenstates, simple amplification of the (single-qubit) pulses does not yield the desired propagator anymore. It rather creates a mismatch between the evolution of the individual qubits on their local Bloch spheres and the evolution governed by the coupling which acts in parallel. To achieve a time optimal propagation from the the initial state into the final state, one has to take this coupling into account and shape the pulses optimally [8, 71]. Other boundary conditions requiring complex pulse shapes might be the avoidance of certain Fourier components in the pulse to prevent the excitation of leakage levels [72] or the optimization of the shape with respect to other parameters.

The need for complex pulses in order to achieve the desired behavior of the system is accompanied by the need to actually shape these pulses with available technology. As mentioned above, decoherence and coupling eventually require this shaping to act on very short timescales, not (yet) reached by waveform generators.

In this chapter, we discuss pulse shaping by networks of passive electronic elements. This work stands in the context of the time-optimal implementation of a CNOT gate in a system of two coupled charge qubits (see the corresponding publication in appendix G). The task is to find an approximation for the optimal pulses that can be implemented by a passive circuit network and yields a high fidelity of the gate operation. Moreover, we will find that the number of elements needed to obtain a good approximation of the pulse provides a measure of its complexity.

6.1 Laplace transform

There are two equivalent descriptions of a signal: the description in the time domain as expressed by a function $f(t)$ or the description as spectrum written as $F(s)$. We want to deal with the spectrum as obtained by the one-side Laplace transform

$$F(s) = \mathcal{L}\{f(t)\} = \int_{t=0}^{\infty} f(t) e^{-st} dt . \quad (6.1)$$

s is a complex variable and can be considered to be a complex frequency. The necessary and sufficient condition for the existence of the spectrum of a function $f(t)$ is that the integral on the right hand side remains finite.

We restrict ourselves to the discussion of rational functions with real coefficients, $F(s) = \frac{P(s)}{Q(s)}$, where $P(s)$ denotes the polynomial in the numerator and $Q(s)$ the polynomial in the denominator. We will see that rational functions play an outstanding role in network synthesis theory. Moreover, the restriction to rational functions is not a strong limitation, because many of the most important time-domain functions (the Dirac delta function, the trigonometric functions etc., see table F.1 in appendix F) yield a spectrum that is in fact a rational function.

By dividing $P(s)$ by $Q(s)$ we obtain

$$F(s) = \frac{P(s)}{Q(s)} = a_n s^n + a_{n-1} s^{n-1} + \dots + a_1 s + a_0 + \frac{P_1(s)}{Q(s)} . \quad (6.2)$$

This allows for finding the corresponding time function for every individual term (after possibly rewriting $\frac{P_1(s)}{Q(s)}$ as sum of partial fractions) by reverse lookup in table F.1.

We list two properties of the Laplace transform, which will be made use of later:

- The spectrum of the function $f(t-t_0)$ shifted by a time $t_0 \geq 0$ is related to the spectrum of the unshifted function $f(t)$ via

$$\mathcal{L}\{f(t-t_0)\} = e^{-st_0} \mathcal{L}\{f(t)\} . \quad (6.3)$$

- The spectrum of the first derivative $\frac{df}{dt}$ of a function $f(t)$ is related to the spectrum of the function $f(t)$ via

$$\mathcal{L}\left\{\frac{df}{dt}\right\} = s \mathcal{L}\{f(t)\} - f(0) . \quad (6.4)$$

6.2 LTI-Systems and transfer functions

We are looking for a system which is capable of shaping a complex output pulse $p(t)$ out of a simple input pulse $q(t)$,

$$p(t) = \text{Tr}\{q(t)\} , \quad (6.5)$$

where $\text{Tr}\{q(t)\}$ is the transformation performed by the system on the input signal.

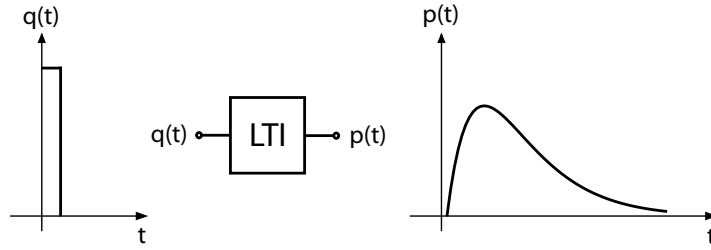


Figure 6.1: Response $p(t)$ of a LTI system on a rectangular input pulse $q(t)$.

Here, we want to deal with LTI (**L**inear **T**ime-**I**nvariant) systems [73]. A system is called linear if each superposition of input signals $q_i(t)$ results in the corresponding superposition of output signals $p_i(t)$,

$$p(t) = \text{Tr} \left\{ \sum_i a_i q_i(t) \right\} = \sum_i a_i \text{Tr}\{q_i(t)\} = \sum_i a_i p_i(t) . \quad (6.6)$$

A system is called time-invariant if the relation between the input and output signal does not depend on time,

$$\text{Tr}\{q(t - t_0)\} = p(t - t_0) . \quad (6.7)$$

Both conditions are fulfilled for networks assembled of devices which are individually linear and time-invariant, such as resistors, capacitors and inductors. The equations of motion for the input and output variables of LTI systems are linear differential equations with constant coefficients.

The internal structure of such systems is in general complicated. However, the analysis of the properties of the system can be reduced to the analysis of the system response $h(t)$ to a properly chosen input pulse, the Dirac pulse $\delta(t)$,

$$h(t) = \text{Tr}\{\delta(t)\} . \quad (6.8)$$

$h(t)$ is called impulse response and depends only on the properties of the system. The output signal $p(t)$ for an arbitrary input signal $q(t)$ is the convolution of $q(t)$ with this characteristic impulse response¹,

$$p(t) = \int_{-\infty}^{\infty} q(\tau) h(t - \tau) d\tau = \int_0^t q(\tau) h(t - \tau) d\tau . \quad (6.9)$$

Thus, the impulse response can be considered to be the Green's function of the system. The power of the spectrum description as introduced above comes into play when one notes that this convolution in the time domain simplifies to a multiplication of the spectra,

$$P(s) = \mathcal{L}\{p(t)\} = \int_0^{\infty} \left[\int_0^{\infty} q(\tau) h(t - \tau) d\tau \right] e^{-st} dt . \quad (6.10)$$

¹Both characteristics of an LTI-system, linearity and time-invariance can be found in (6.9): The integral can be understood as the continuous limit of the superposition sum in (6.6), and as the system is time-invariant, $h(t, \tau)$ depends only on the time difference, $h(t, \tau) = h(t - \tau)$.

Exchanging the order of the integrals and using (6.3) yields

$$P(s) = \int_0^\infty q(\tau) \left[\int_0^\infty h(t - \tau) e^{-st} dt \right] d\tau = \int_0^\infty q(\tau) e^{-s\tau} H(s) d\tau = Q(s) H(s) . \quad (6.11)$$

$H(s) = \mathcal{L}\{h(t)\}$ is called transfer function and completely describes the output response $P(s)$ of the LTI-system to an arbitrary input signal $Q(s)$ in the spectrum domain. Since LTI-systems can be described by linear differential equations with real coefficients, $H(s)$ is always a rational function with real coefficients².

6.3 Circuit synthesis theory

The topic of circuit synthesis theory is concerned with constructing networks in order to realize a given rational transfer function (or several transfer functions in the case of a four terminal network). However, not all rational functions are valid transfer functions for all kinds of networks. Depending on the properties of the transfer function, the topology of the network and the types of the elements constituting the network, circuit synthesis theory also gives necessary and sufficient conditions to decide whether a given function can be implemented or not. In the following, we want to concentrate on the latter question. The actual construction of networks out of given transfer functions is roughly described in appendix F.2. A comprehensive survey of the subject can be found in [74].

6.3.1 Two terminal networks

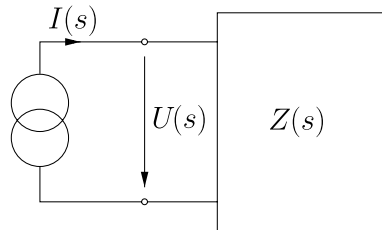


Figure 6.2: Block diagram of a two terminal network connected to a current source. The input signal is the current $I(s)$ provided by the source, the response of the network is the voltage $U(s)$.

Two terminal networks are characterized by the relation of voltage $U(t)$ and current $I(t)$. We express this relation in terms of the spectra and the transfer function (by convention denoted by $Z(s)$),

$$Z(s) = \frac{U(s)}{I(s)} . \quad (6.12)$$

However, implementation by a two terminal network sets narrow restrictions on the allowed transfer function. We aim for finding a network whose output signal for a simple input signal gives a good approximation of the desired pulse shapes shown in figure 6.5 (red curves). To do

²For networks assembled from resistors, H does not depend on s .

so, we proceed to the more general case of four terminal networks, making use of the greater variety of valid transfer functions.

6.3.2 Four terminal networks

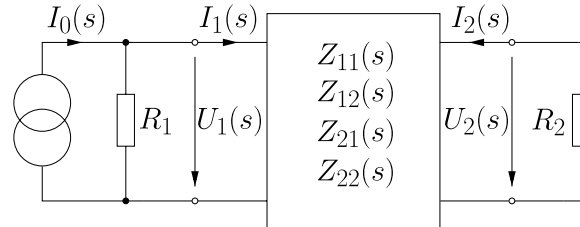


Figure 6.3: Block diagram of a four terminal network. Here, the case $R_1 = R_2 = \infty$ is treated, i.e. an ideal current source connected to the input and a system with infinite working resistance connected to the output. In this case, we only need to specify $Z_{21}(s)$, whereas the other transfer functions remain to be chosen according to the conditions imposed by the desired realization.

As only one equation –and one transfer function– is required to describe a two terminal network, we need two equations –and four transfer functions– to characterize the relations between the input and output voltages and currents $U_1(s)$, $I_1(s)$, $U_2(s)$ and $I_2(s)$ of a four terminal network,

$$\begin{pmatrix} U_1(s) \\ U_2(s) \end{pmatrix} = \begin{pmatrix} Z_{11}(s) & Z_{12}(s) \\ Z_{21}(s) & Z_{22}(s) \end{pmatrix} \begin{pmatrix} I_1(s) \\ I_2(s) \end{pmatrix}. \quad (6.13)$$

The behavior of the network is now completely described by the four coefficients (transfer functions) $Z_{11}(s)$, $Z_{12}(s)$, $Z_{21}(s)$ and $Z_{22}(s)$.

What restrictions apply to the poles and zeros of a four pole transfer function? Consider a transfer function $Z(s)$ in the form

$$Z(s) = \frac{P(s)}{Q(s)} = \frac{a_m s^m + \dots + a_1 s + a_0}{b_n s^n + \dots + b_1 s + b_0}, \quad (6.14)$$

where $Z(s)$ denotes any of the above transfer functions constituting the four pole. In consequence of $P(s)$ and $Q(s)$ having only real coefficients, complex zeros and poles can only occur as pairs of complex conjugates.

Moreover, we want to take a look at the time domain behavior of the input and output signals.

Stability

Let $p(t)$ be the time domain function of the output and $q(t)$ of the input signal. Eq. (6.14) corresponds to the differential equation

$$b_n \frac{d^n p(t)}{dt^n} + \dots + b_1 \frac{dp(t)}{dt} + b_0 p(t) = a_m \frac{d^m q(t)}{dt^m} + \dots + a_1 \frac{dq(t)}{dt} + a_0 q(t), \quad (6.15)$$

as one can obtain (6.14) by applying (6.4) to (6.15).

An important demand on the network as a physical system is that for any bounded input, the output will also be bounded. This condition is called stability. For an input $q(t) \equiv 0$, the differential equation for the output

$$b_n \frac{d^n p}{dt^n} + \dots + b_1 \frac{dp}{dt} + b_0 p = 0 \quad (6.16)$$

can be solved by the ansatz $p(t) = k e^{\lambda t}$. Owing to stability as defined above, there must be no increasing eigen oscillations, therefore all roots of the characteristic equation

$$b_n \lambda^n + \dots + b_1 \lambda + b_0 = 0 \quad (6.17)$$

need to have non-positive real part, i.e. all roots lie on the left half-plane of the complex plane or on the imaginary axis. Roots located on the imaginary axis need to be single.

If this is true for all zero points of a polynomial, the polynomial is called *modified Hurwitz polynomial*.

We find:

The denominator of a stable four pole transfer function is a modified Hurwitz polynomial.

Additional restrictions on the location of poles, the parity of the transfer function (odd or even), etc., are imposed if one sets limitations on the types of elements used, for instance LC- or RC-networks. However, we want to consider the least restrictive case of RLC-networks, i.e. networks consisting of resistors, inductors and capacitors.

Moreover, for the case of finite R_1 and R_2 as shown in figure 6.3, relations between input and output variables are in general not given by one single transfer function, but by combinations of several ones. As an example, we take a look at the case $R_1 = \infty$, R_2 finite. U_2 is then given by $U_2(s) = -R_2 I_2(s)$, and the relation between input current $I_1(s)$ and output voltage $U_2(s)$ (using the second line of (6.13)) reads

$$\frac{U_2(s)}{I_1(s)} = \frac{-R_2 I_2(s)}{-\frac{R_2 + Z_{22}(s)}{Z_{21}(s)} I_2(s)} = \frac{Z_{21}(s) R_2}{Z_{22}(s) + R_2}. \quad (6.18)$$

$\frac{U_2(s)}{I_1(s)}$ is again a transfer function. However, it has in general additional restrictions, since the functions $Z_{11}(s)$, $Z_{12}(s)$, $Z_{21}(s)$ and $Z_{22}(s)$ are not independent from each other [74].

For our purposes, we consider $R_1 = R_2 = \infty$. This corresponds to an ideal current source connected to the input and a system with infinite working resistance at the output (resulting in $I_2 = 0$). Naturally, the input variable is the current $I_1(s)$, whereas the output variable is the voltage $U_2(s)$. The transfer function relating these variables is

$$\frac{U_2(s)}{I_1(s)} = Z_{21}(s), \quad (6.19)$$

which obeys no further restrictions than the ones mentioned above, i.e. a rational function with real coefficients and no poles in the right half-plane of the complex plane.

6.4 Approximation and results

We want to move on to the actual issue. In figure 6.5, the time course of the desired output pulses $\delta n_{g,C}(t)$ for the gate voltage of the control qubit and $\delta n_{g,T}(t)$ for the target qubit (red curves) in a system of two charge qubits along with the approximations by our filter networks (blue curves) are shown.

We first state that the input pulse is arbitrary and should be kept simple, however, it has to contain enough spectral weight at the dominating harmonics of the output pulse. Here, we start for both output pulses with a rectangular input current pulse of length $\tau_r = 1.1$ ps. The short duration of the pulse guarantees a broad frequency spectrum. These time scales are already accessible by the application of well established optoelectronic techniques to the generation and detection of terahertz (THz) pulses [75] used in the field of femtochemistry for the investigation of the dynamics of chemical reactions [76].

The time courses for the optimal pulses in figure 6.5 actually show the interpolating envelope of 50 discrete data points resulting from the numerical optimization. Since the Laplace transform can only be applied to continuous functions, the pulses were written as a sum of 6 (for the pulse on the control qubit, 7 for the target pulse, respectively) harmonic functions obtained by discrete-time Fourier transform. The transfer function for the control pulse (the target pulse) then looks like

$$H(s)_{C(T)} = \frac{\mathcal{L}\{\mathcal{F}\{t_n, \delta n_{g,C(T)}(t_n)\}\}}{\mathcal{L}\{\Theta(t) \Theta(-t + \tau_r)\}} = \frac{\mathcal{L}\{\mathcal{F}\{t_n, \delta n_{g,C(T)}(t_n)\}\}}{(1 - e^{-s\tau_r})/s} \quad (6.20)$$

with $\Theta(t) \Theta(-t + \tau_r)$ making up the rectangular pulse of length τ_r ($\Theta(t)$ denotes the Heaviside function), and $\mathcal{F}\{t_n, \delta n_{g,C(T)}(t_n)\}$ being the Fourier transform of the discrete set of pulse amplitudes $\delta n_{g,C(T)}(t_n)$ of the control qubit (the target qubit).

We aim for determining a four-pole transfer function $Z_{21}(s)$ with the restrictions pointed out above, approximating $H(s)$. The used algorithm finds rational functions $f(x)$, which interpolate a set of data points $\{x_i, y_i\}$ –in our case a finite number of sampling points of $H(s)$ – by a rational function with given degrees for the nominator and denominator polynomial. As $H(s)$ turns out to approach a finite value for $s \rightarrow \pm\infty$, the degrees of the nominator and the denominator need to be equal.

As expected, a small degree results in an inaccurate approximation with the inverse Laplace transform $\mathcal{L}^{-1}\{\mathcal{L}\{\Theta(t) \Theta(-t + \tau_r)\} Z_{21}(s)\}$ of the shaped output pulse showing large deviations from the desired pulse (see figure 6.4).

For higher degrees, the rational interpolation is in increasingly good agreement with the desired pulses. Figure 6.5 shows the approximation achieved by two transfer functions with the degree 14 for the control qubit and 18 for the target qubit, respectively. The higher degree of the network shaping the pulse for the target qubit is consistent with the higher number of harmonics contained in the pulse (see above) and confirms the usability of the network complexity as measure for the complexity of the pulse.

For the same filter networks, a characterization showing the location of the poles with the corresponding residue is displayed in figure 6.6. According to the constructional methods described in appendix F.2, each pole on the negative real axis corresponds to a RC-filter, a pair of complex conjugate poles yields a LCR-filter. The pulse for the control qubit can thereby be approximated with 6 LCR filters and 2 RC filters, the pulse for the target qubit

with 8 LCR filters and 2 RC-filters. The fidelity of the gate operation, i.e. the overlap of the ideal CNOT propagator with the propagator (refer to publication, appendix G) induced by the approximated pulses is higher than 94%. In reality, first the parameters of the sample have to be determined spectroscopically before adapting the filter network accordingly. Moreover, the pulse arriving at the sample will be distorted by the transmission through the leads etc. (which can be again modelled by the corresponding transfer function), which needs to be compensated.

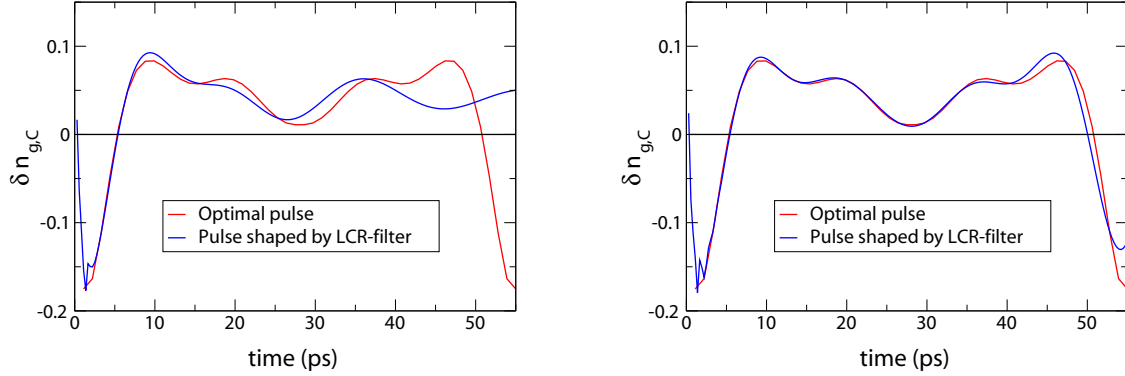


Figure 6.4: Time course of the desired output pulse for the control qubit and its approximation shaped by filter networks of varying complexity. Left: Approximation by a transfer function with degree 6. Right: Approximation by a transfer function with degree 11. The increasing quality of the approximation with increasing degree of the transfer function allows for measuring the pulse complexity in terms of complexity of the transfer function.

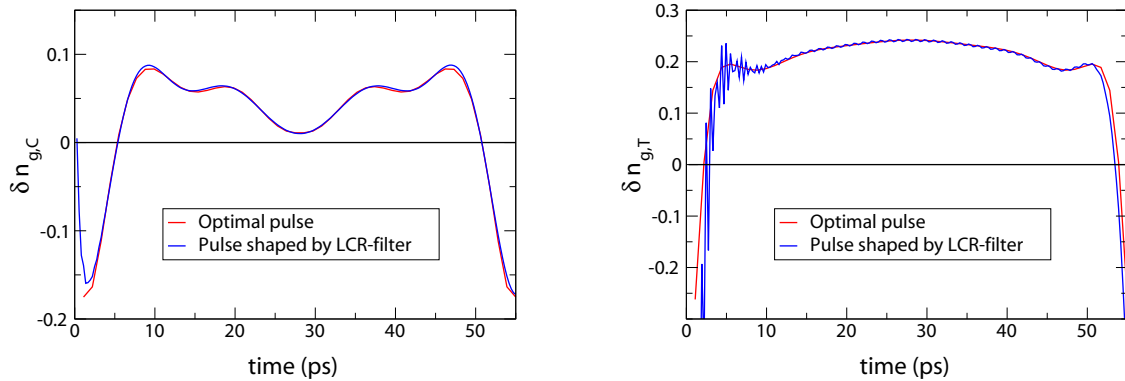


Figure 6.5: Time course of the desired output and the pulses shaped by the filter networks. Left: Control qubit pulse, approximated by a transfer function with degree 14. Right: Target qubit pulse approximated by a transfer function with degree 18.

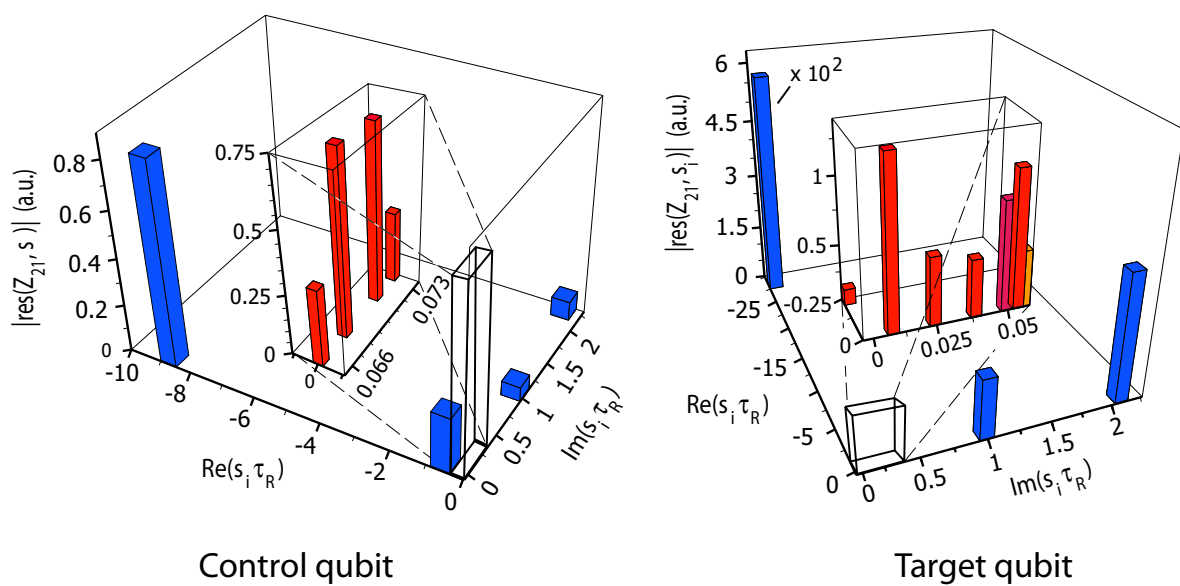


Figure 6.6: Pole configuration of the filters shaping the pulses and the corresponding residue. The position of the bars shows the position of the poles s_i in the complex Laplace plane. Poles on the negative imaginary axis correspond to RC-filters, poles outside also lead to the complex conjugate poles and can be implemented by LCR-filters. The height of the bars shows the modulus of the residue at this pole. The boxes in the middle are blow-ups of the regions close to the origin.

Conclusions

In this work, we showed the suitability of a system of three coupled flux qubits to exhibit strong tripartite entanglement for a realistic and approachable set of parameters as well as the feasibility to prepare, detect and identify this entanglement by available technology.

In chapter 2, we discussed the types and the strengths of the interactions between the qubits for two possible designs, an arrangement of the three qubits next to each other with an additional joint SQUID-loop acting as flux transformer (Fig. 2.1) and a triangle geometry (Fig. 2.2), providing the coupling mainly via the Josephson inductances of shared junctions placed in shared lines between the qubits. Both of these designs cause a pairwise antiferromagnetic Ising type coupling $\hat{\sigma}_z^{(i)} \otimes \hat{\sigma}_z^{(j)}$, where the coupling in the triangle design is found to be much stronger and takes –depending on the size of the shared junctions– values of approx. 1.4Δ (Δ is the tunnel matrix element of the qubits). In section 2.3, we proposed a readout geometry consisting of three SQUIDs attached to the sides of the triangle.

In chapter 3, the properties of the eigenstates of the system were investigated for different coupling strengths and in different regimes of the energy bias ϵ . Due to the antiferromagnetic coupling, the ground state is a superposition of frustrated states (3.29), whereas the highest excited states are for strong coupling close to GHZ states in a small range around zero energy bias (3.31). Moreover, by writing down the Hamiltonian in an appropriate collective basis (3.3), we found two degenerate pairs of eigenstates forming two subspaces. Among the states contained in these degenerate subspaces, we identified states with maximal entanglement, which are equivalent to the W state (3.19) under local unitary operations, see (3.21) and (3.27).

The preparation of these maximally entangled states in the subspaces by application of external microwave fields is covered in chapter 4. By means of a dressed state approach we showed that preparation of arbitrary superpositions of the basis states is possible by pulsing the qubits individually.

In chapter 5, we addressed the detection of tripartite entanglement and violation of Bell inequalities in more detail. We used the 3-tangle [50] and entanglement witnesses (5.1) as tools to identify tripartite entanglement. We detected GHZ type entanglement in the regime of zero energy bias mentioned above (Fig. 5.1) and –in a more robust manner– in a regime of finite energy bias (Fig. 5.3). The W type entanglement in the degenerate subspaces was investigated in 5.1.3 and was found to persist over a large range of the energy bias (Fig. 5.5). Moreover, we observed significant violations of adapted, optimized Bell type inequalities in all these regimes (Fig. 5.2, 5.4, 5.6).

Starting from the local decompositions of the Bell operators and the entanglement witnesses, we discussed the effect of a limited measurement fidelity in section 5.3. The required fidelities

are almost identical and even slightly lower than for the case of two qubits (table 5.3) and were shown to be approachable with recently developed measurement techniques. Thus, the proposed design is indeed suitable for demonstrating tripartite entanglement.

In chapter 6, we presented an approach to the shaping of short pulse sequences by filter networks of passive circuit elements. This was done for the example of a quantum gate implementation in a system of two coupled charge qubits, where an accurate approximation of an optimal pulse sequence (Fig. 6.5) could be achieved with a small number of filter elements (Fig. 6.6), yielding an overlap with the ideal gate propagator of more than 94%. We also outlined the connection between the complexity of the desired pulse on the one hand side and the complexity of the filter network on the other hand side, which allows for estimating and measuring the pulse complexity in terms of properties of the required network (6.4).

Acknowledgments

This diploma thesis and the associated year of work would not have been possible without help and support of many others and even if it would have been possible, it would have been a pain.

I would like to thank Prof. Dr. Jan von Delft for giving me the opportunity to join his group. The environment and atmosphere in the group, professionally as well as personally made it easy to enjoy this time and to learn a lot.

I would particularly like to thank my supervisor PD Dr. Frank Wilhelm, for his advice and help concerning physical and non-physical aspects, his support and discussions in form of 'intellectual pressure fuelling'.

I want to thank Markus Storcz for his continuous support, help and devotion in all kinds of aspects, this has been very helpful and a good example.

Thank goes to Dr. Thomas Schulte-Herbrüggen and Andreas Spörl of the group of Prof. Dr. Steffen Glaser for the fruitful collaboration and the stimulating, intense discussions. I also thank John Clarke and Birgitta Whaley for inviting me to visit their groups in Berkeley. I very much look forward to it.

Thanks to my officemates Michael and Henryk for tolerating my presence for one whole year and for being open to all kinds of questions, to physical, philosophical and profane discussions. The same holds for all the other people at the chair for theoretical condensed matter physics, it was a pleasure to me.

Thanks to my friends, especially Moritz, Ferdinand and Lukas, for their company and much more. Speaking of the last year, I also don't want to forget our common friend Jack, see you again!

I would like to thank my girlfriend Blanca. Be it her understanding for many of my ideas or be it the lack of understanding for some others, it has always been the right call.

Last, but in no way least thanks to my parents and my brothers for their support and dedication over all these many years. You cannot choose your family but I am definitely lucky.

Appendix A

Three-spin basis

The standard basis is given by the eigenstates of the tensor product of the z-components of the individual spins $\hat{s}_z^i = \frac{1}{2} \hat{\sigma}_z^i$,

$$(\hat{s}_z^1 \otimes \hat{s}_z^2 \otimes \hat{s}_z^3) |m_s^1 m_s^2 m_s^3\rangle = m_s^1 m_s^2 m_s^3 |m_s^1 m_s^2 m_s^3\rangle, \quad (\text{A.1})$$

where $m_s^i = \pm 1/2$ corresponds to $|m_s^i\rangle = |\uparrow\rangle$ ($|\downarrow\rangle$), respectively).

$$\begin{aligned} |\uparrow\uparrow\uparrow\rangle &= (1, 0, 0, 0, 0, 0, 0, 0)^T = |v_1\rangle \\ |\uparrow\uparrow\downarrow\rangle &= (0, 1, 0, 0, 0, 0, 0, 0)^T = |v_2\rangle \\ |\uparrow\downarrow\uparrow\rangle &= (0, 0, 1, 0, 0, 0, 0, 0)^T = |v_3\rangle \\ |\uparrow\downarrow\downarrow\rangle &= (0, 0, 0, 1, 0, 0, 0, 0)^T = |v_4\rangle \\ |\downarrow\uparrow\uparrow\rangle &= (0, 0, 0, 0, 1, 0, 0, 0)^T = |v_5\rangle \\ |\downarrow\uparrow\downarrow\rangle &= (0, 0, 0, 0, 0, 1, 0, 0)^T = |v_6\rangle \\ |\downarrow\downarrow\uparrow\rangle &= (0, 0, 0, 0, 0, 0, 1, 0)^T = |v_7\rangle \\ |\downarrow\downarrow\downarrow\rangle &= (0, 0, 0, 0, 0, 0, 0, 1)^T = |v_8\rangle \end{aligned} \quad (\text{A.2})$$

We aim for finding a collective basis, i.e. a basis of eigenstates of the total spin and its z-component rather than of the individual z-components. To do so, we use the well known singlet-triplet basis, say for the qubits denoted by 1 and 2, $|m_s^1 m_s^2\rangle \longrightarrow |s^{12} m_s^{12}\rangle$ and couple a third spin 1/2 particle to it,

$$|m_s^1 m_s^2 m_s^3\rangle \longrightarrow |s^{\text{tot}} m_s^{\text{tot}} s^{12}\rangle. \quad (\text{A.3})$$

The third quantum number s^{12} denotes the total spin of the qubits 1 and 2 combined (possible values being 1 or 0) and has to be carried along to exclude ambiguities (e.g. between the states $|\frac{1}{2} \frac{1}{2} 0\rangle$ and $|\frac{1}{2} \frac{1}{2} 1\rangle$). We express these states in terms of the uncoupled basis and determine the Clebsch-Gordan coefficients $C(s^{\text{tot}} m_s^{\text{tot}} s^{12}, m_s^1 m_s^2 m_s^3) = \langle s^{\text{tot}} m_s^{\text{tot}} s^{12} | m_s^1 m_s^2 m_s^3 \rangle$ by the common method of iteratively applying the lowering operator, starting from the state $|\frac{3}{2} \frac{3}{2} 1\rangle$, as described in Ref. [77]. We arrive at:

$$\begin{aligned}
\left| \frac{3}{2} \frac{3}{2} 1 \right\rangle &= |\uparrow\uparrow\uparrow\rangle &= (1, 0, 0, 0, 0, 0, 0, 0)^T = |\tilde{v}_1\rangle \\
\left| \frac{3}{2} \frac{1}{2} 1 \right\rangle &= \frac{1}{\sqrt{3}} (|\uparrow\uparrow\downarrow\rangle + |\uparrow\downarrow\uparrow\rangle + |\downarrow\uparrow\uparrow\rangle) &= (0, 1, 0, 0, 0, 0, 0, 0)^T = |\tilde{v}_2\rangle \\
\left| \frac{3}{2} -\frac{1}{2} 1 \right\rangle &= \frac{1}{\sqrt{3}} (|\downarrow\downarrow\uparrow\rangle + |\downarrow\uparrow\downarrow\rangle + |\uparrow\downarrow\downarrow\rangle) &= (0, 0, 1, 0, 0, 0, 0, 0)^T = |\tilde{v}_3\rangle \\
\left| \frac{3}{2} -\frac{3}{2} 1 \right\rangle &= |\downarrow\downarrow\downarrow\rangle &= (0, 0, 0, 1, 0, 0, 0, 0)^T = |\tilde{v}_4\rangle \\
\left| \frac{1}{2} \frac{1}{2} 1 \right\rangle &= -\sqrt{\frac{2}{3}} |\uparrow\uparrow\downarrow\rangle + \frac{1}{\sqrt{6}} (|\downarrow\uparrow\uparrow\rangle + |\uparrow\downarrow\uparrow\rangle) &= (0, 0, 0, 0, 1, 0, 0, 0)^T = |\tilde{v}_5\rangle \\
\left| \frac{1}{2} -\frac{1}{2} 1 \right\rangle &= \sqrt{\frac{2}{3}} |\downarrow\downarrow\uparrow\rangle - \frac{1}{\sqrt{6}} (|\uparrow\downarrow\downarrow\rangle + |\downarrow\uparrow\downarrow\rangle) &= (0, 0, 0, 0, 0, 1, 0, 0)^T = |\tilde{v}_6\rangle \\
\left| \frac{1}{2} \frac{1}{2} 0 \right\rangle &= \frac{1}{\sqrt{2}} (|\downarrow\uparrow\uparrow\rangle - |\uparrow\downarrow\uparrow\rangle) &= (0, 0, 0, 0, 0, 0, 1, 0)^T = |\tilde{v}_7\rangle \\
\left| \frac{1}{2} -\frac{1}{2} 0 \right\rangle &= \frac{1}{\sqrt{2}} (|\downarrow\uparrow\downarrow\rangle - |\uparrow\downarrow\downarrow\rangle) &= (0, 0, 0, 0, 0, 0, 0, 1)^T = |\tilde{v}_8\rangle \quad (\text{A.4})
\end{aligned}$$

States and operators in the new coupled basis are written with a tilde,

$$|\tilde{\psi}\rangle = S |\psi\rangle, \quad \tilde{O} = S \hat{O} S^\dagger, \quad (\text{A.5})$$

where $S_{ij} = \langle \tilde{v}_i | v_j \rangle$ is the operator mediating the basis transfer (the matrix of the Clebsch-Gordan coefficients).

Appendix B

Eigenenergies and eigenstates of the doublets

The doublet Hamiltonian reads

$$\mathbf{H} = -\frac{1}{2} \begin{pmatrix} \epsilon + 2C & \Delta \\ \Delta & -\epsilon + 2C \end{pmatrix}. \quad (\text{B.1})$$

The eigenenergies and corresponding eigenstates in the quartet/doublet basis read

$$\begin{aligned} E_5, E_7 &= -C - \frac{\Lambda}{2}, \\ E_6, E_8 &= -C + \frac{\Lambda}{2}. \end{aligned} \quad (\text{B.2})$$

$$\begin{aligned} |\tilde{\psi}_1^L\rangle &= \frac{1}{\sqrt{2\Lambda(\Lambda + \epsilon)}} \begin{pmatrix} 0 \\ 0 \\ 0 \\ 0 \\ -\Delta \\ \epsilon + \Lambda \\ 0 \\ 0 \end{pmatrix}, \quad |\tilde{\psi}_1^H\rangle = \frac{1}{\sqrt{2\Lambda(\Lambda - \epsilon)}} \begin{pmatrix} 0 \\ 0 \\ 0 \\ 0 \\ -\Delta \\ \epsilon - \Lambda \\ 0 \\ 0 \end{pmatrix} \\ |\tilde{\psi}_2^L\rangle &= \frac{1}{\sqrt{2\Lambda(\Lambda + \epsilon)}} \begin{pmatrix} 0 \\ 0 \\ 0 \\ 0 \\ 0 \\ 0 \\ 0 \\ -\Delta \\ \epsilon + \Lambda \end{pmatrix}, \quad |\tilde{\psi}_2^H\rangle = \frac{1}{\sqrt{2\Lambda(\Lambda - \epsilon)}} \begin{pmatrix} 0 \\ 0 \\ 0 \\ 0 \\ 0 \\ 0 \\ 0 \\ -\Delta \\ \epsilon - \Lambda \end{pmatrix} \end{aligned} \quad (\text{B.3})$$

with $\Lambda = \sqrt{\Delta^2 + \epsilon^2}$.

Appendix C

Structure of the eigenstates

We plot the projection of the eigenstates $|E_1\rangle$ – $|E_8\rangle$ onto the states of the standard basis. The discussion of the properties of the eigenstates in chapter 3 is mainly based on these plots.

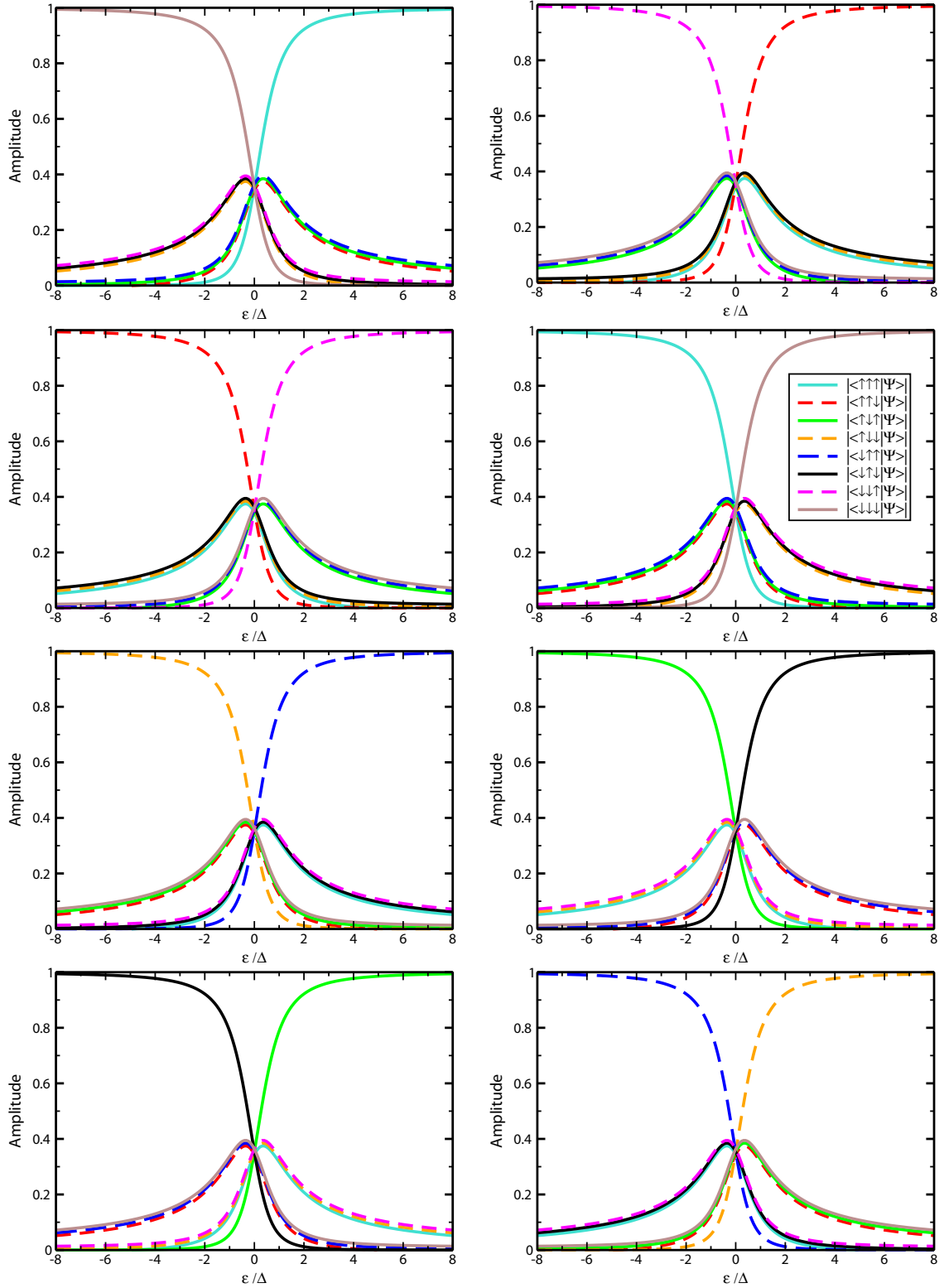


Figure C.1: Plot of the projections of eigenstates $|E_1\rangle$ – $|E_8\rangle$ (from upper left to lower right; first row: $|E_1\rangle, |E_2\rangle$; second row: $|E_3\rangle, |E_4\rangle$; etc.) onto the basis states of the standard basis vs. ϵ for $C = 0$. Curves that lie on top of each other are slightly shifted in order to make them distinguishable. See figure 3.1 for labelling of the eigenstates. Consider that $|E_2\rangle, |E_5\rangle, |E_7\rangle$ form a basis of a degenerate subspace, as well as $|E_3\rangle, |E_6\rangle, |E_8\rangle$ (details in section 3.2)

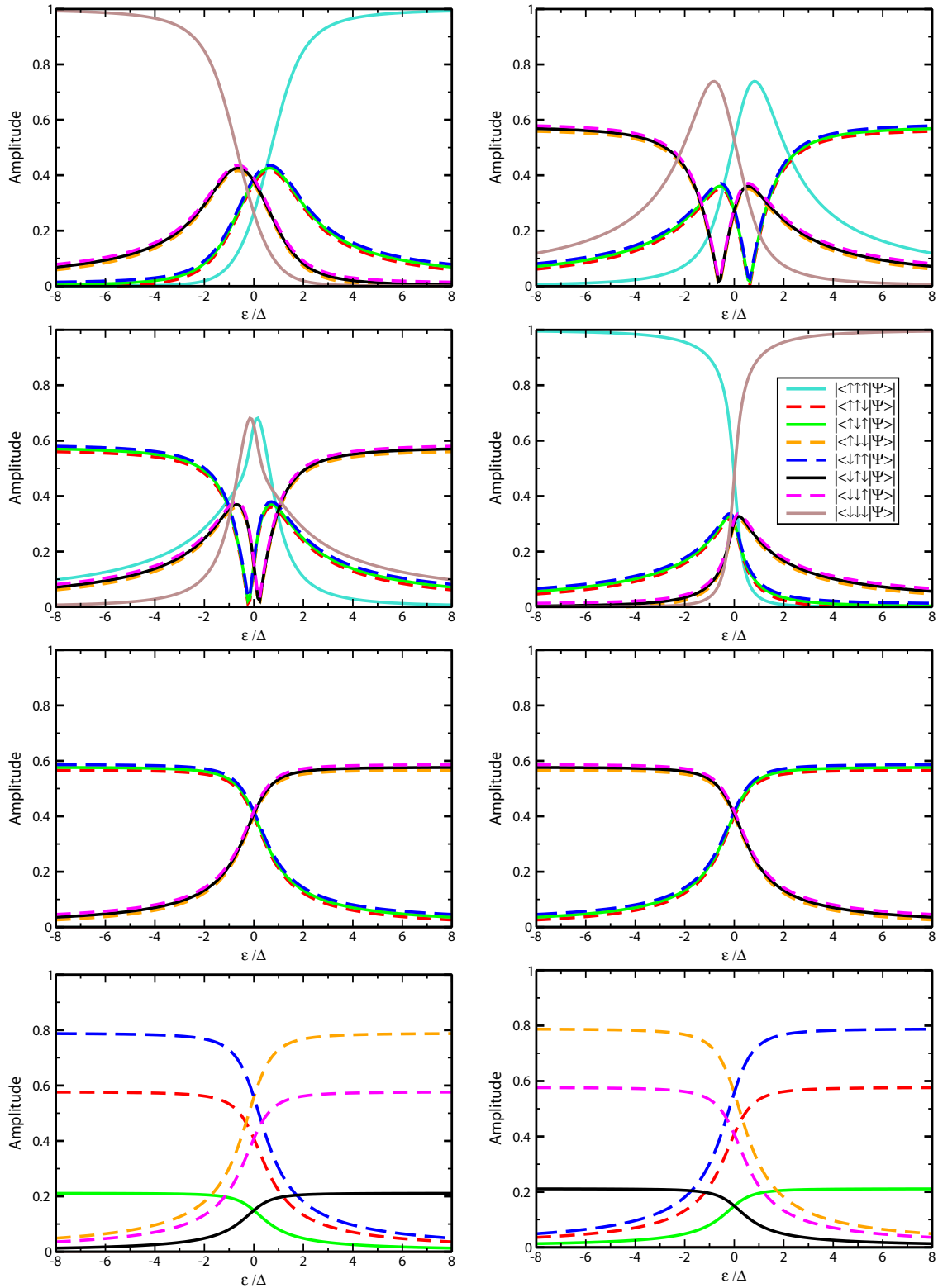


Figure C.2: Plot of the projections of eigenstates $|E_1\rangle$ – $|E_8\rangle$ (from upper left to lower right; first row: $|E_1\rangle, |E_2\rangle$; second row: $|E_3\rangle, |E_4\rangle$; etc.) onto the basis states of the standard basis vs. ϵ for $C = 0.2\Delta$. Curves that lie on top of each other are slightly shifted in order to make them distinguishable. See figure 3.1 for labelling of the eigenstates. Consider that $|E_5\rangle$ and $|E_7\rangle$ form a basis of a degenerate subspace, as well as $|E_6\rangle$ and $|E_8\rangle$ (details in section 3.3)

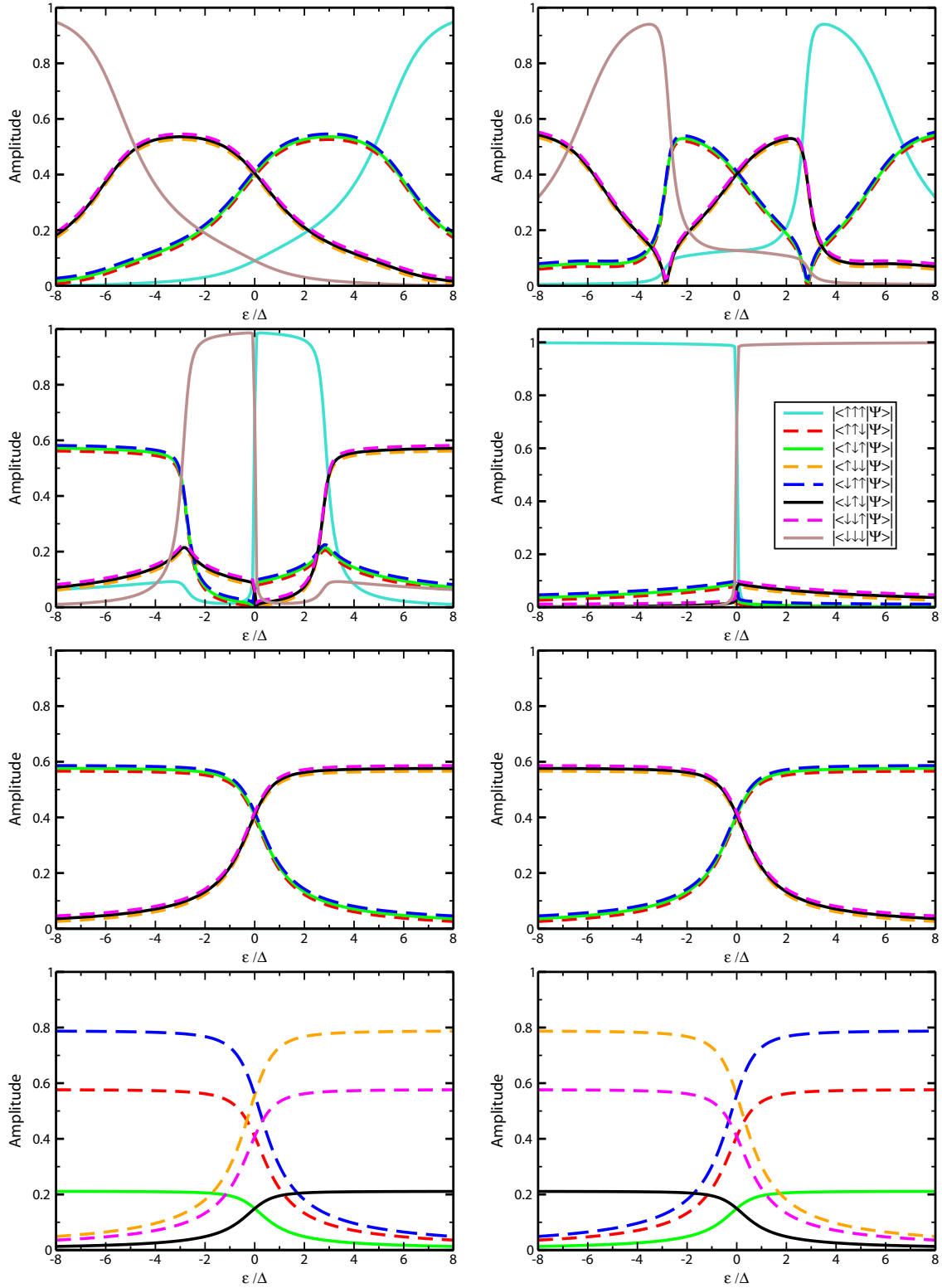


Figure C.3: Plot of the projections of eigenstates $|E_1\rangle$ – $|E_8\rangle$ (from upper left to lower right; first row: $|E_1\rangle, |E_2\rangle$; second row: $|E_3\rangle, |E_4\rangle$; etc.) onto the basis states of the standard basis vs. ϵ for $C = 1.4\Delta$. Curves that lie on top of each other are slightly shifted in order to make them distinguishable. See figure 3.1 for labelling of the eigenstates. Consider that $|E_5\rangle$ and $|E_7\rangle$ form a basis of a degenerate subspace, as well as $|E_6\rangle$ and $|E_8\rangle$ (details in section 3.4)

Appendix D

Entanglement measures

The quantification of entanglement is a long standing problem in quantum information theory. An entanglement measure does not need to be an observable, however, it has to satisfy certain conditions. In particular, it has to be an *entanglement monotone* [78], i.e. it must not increase on average under stochastic local operations and classical communication (SLOCC) [47, 79]. An important measure is the *entanglement of formation* [80, 81, 82], which gives the number of Einstein-Podolsky-Rosen pairs asymptotically required to prepare a given state. By investigating the entanglement properties of mixed bipartite states, a measure for tripartite pure states could be derived, the 3-tangle [50].

D.1 3-tangle

The 3-tangle τ can be expressed in terms of the coefficients a_{ijk} of the state in the standard basis, $|\psi\rangle = \sum_{ijk} a_{ijk} |ijk\rangle$, by

$$\tau = 4|d_1 - 2d_2 + 4d_3|, \quad (\text{D.1})$$

where

$$\begin{aligned} d_1 &= a_{000}^2 a_{111}^2 + a_{001}^2 a_{110}^2 + a_{010}^2 a_{101}^2 + a_{100}^2 a_{011}^2 \\ d_2 &= a_{000} a_{111} a_{011} a_{100} + a_{000} a_{111} a_{101} a_{010} + a_{000} a_{111} a_{110} a_{001} + \\ &\quad + a_{011} a_{100} a_{101} a_{010} + a_{011} a_{100} a_{110} a_{001} + a_{101} a_{010} a_{110} a_{001} \\ d_3 &= a_{000} a_{110} a_{101} a_{011} + a_{111} a_{001} a_{010} a_{100}. \end{aligned} \quad (\text{D.2})$$

D.2 Global entanglement

D.2.1 Definition

The global entanglement Q is given by

$$Q(|\psi\rangle) = 2 \left[1 - \frac{1}{n} \sum_1^n \text{Tr} \rho_k^2 \right] \quad (\text{D.3})$$

with ρ_k being the density matrix reduced to a single qubit k .
For the special case of three qubits, this can be rewritten as [64]

$$Q = \frac{2}{3} (C_{12}^2 + C_{13}^2 + C_{23}^2) + \tau, \quad (\text{D.4})$$

where τ is the 3-tangle and C_{ij} the 2-qubit concurrence between qubit i and qubit j [81]. The global entanglement thus measures the sum of different entanglement contributions.

D.2.2 Choice of $|\tilde{E}_5\rangle$ and $|\tilde{E}_7\rangle$

We look for superpositions of $|\tilde{\psi}_1^{L(H)}\rangle$ and $|\tilde{\psi}_2^{L(H)}\rangle$ (the states spanning the degenerate subspaces, see 3.3.2 and appendix B) with maximal (respectively minimal) entanglement and use the global entanglement introduced above as a measure.

For the global entanglement of an arbitrary state

$$|\tilde{\psi}^{L(H)}\rangle = A |\tilde{\psi}_1^{L(H)}\rangle + e^{i\varphi} \sqrt{1 - A^2} |\tilde{\psi}_2^{L(H)}\rangle \quad (\text{D.5})$$

in the low-energy (high-energy) subspace, we obtain (independent from the energy bias)

$$Q(A, \varphi) = \frac{8}{9} (\cos^2 \varphi - 1) (A^4 - A^2) + \frac{2}{3}, \quad (\text{D.6})$$

which leads to the choice of A and φ for maximal (minimal) entanglement as

$$A = \frac{1}{\sqrt{2}}, \quad \varphi = \frac{\pi}{2} \quad \left(A = \frac{1}{\sqrt{2}}, \quad \varphi = 0 \right). \quad (\text{D.7})$$

This results in in $|\tilde{\psi}_{\max}^{L(H)}\rangle$ ($|\tilde{\psi}_{\min}^{L(H)}\rangle$) with maximized (minimized) Q ,

$$|\tilde{\psi}_{\max}^{L(H)}\rangle = \frac{1}{\sqrt{2}} (|\tilde{\psi}_1^{L(H)}\rangle + i |\tilde{\psi}_2^{L(H)}\rangle) := |\tilde{E}_{5(6)}\rangle, \quad (\text{D.8})$$

$$|\tilde{\psi}_{\min}^{L(H)}\rangle = \frac{1}{\sqrt{2}} (|\tilde{\psi}_1^{L(H)}\rangle + |\tilde{\psi}_2^{L(H)}\rangle) := |\tilde{E}_{7(8)}\rangle. \quad (\text{D.9})$$

Appendix E

Driving propagators

Referring to chapter 4, we write down the explicit form of the propagator $\hat{U}(t)$ for the evolution of a state in the interaction picture under the driving Hamiltonian.

For two microwave sources radiating towards the qubits with individual amplitudes κ_1 and κ_2 as expressed by (4.6), the propagator reads (for the connection of ω_1 , ω_2 and Ω to κ_1 and κ_2 , refer to chapter 4)

$$\hat{U}(t) = \frac{1}{\Omega} \begin{pmatrix} \Omega \cos \Omega t & -i\omega_1 \sin \Omega t & -i\omega_2 \sin \Omega t \\ -i\omega_1 \sin \Omega t & \frac{\omega_2^2 + \omega_1^2 \cos \Omega t}{\Omega} & \frac{\omega_1 \omega_2 (\cos \Omega t - 1)}{\Omega} \\ -i\omega_2 \sin \Omega t & \frac{\omega_1 \omega_2 (\cos \Omega t - 1)}{\Omega} & \frac{\omega_1^2 + \omega_2^2 \cos \Omega t}{\Omega} \end{pmatrix}. \quad (\text{E.1})$$

As we assume the initial state to be the ground state written as $(1, 0, 0)^T$ in the basis introduced in (4.22), the evolution is given by the first column in the matrix representing $\hat{U}(t)$.

If the two sources are also shifted by an independent relative phase, the propagator reads

$$\hat{U}(t) = \frac{1}{\Omega} \begin{pmatrix} \Omega \cos \Omega t & -i\omega_1 \sin \Omega t & -i\omega_2 \sin \Omega t e^{-i\varphi} \\ -i\omega_1 \sin \Omega t & \frac{\omega_2^2 + \omega_1^2 \cos \Omega t}{\Omega} & \frac{\omega_1 \omega_2 (\cos \Omega t - 1)}{\Omega} e^{-i\varphi} \\ -i\omega_2 \sin \Omega t e^{i\varphi} & \frac{\omega_1 \omega_2 (\cos \Omega t - 1)}{\Omega} e^{i\varphi} & \frac{\omega_1^2 + \omega_2^2 \cos \Omega t}{\Omega} \end{pmatrix}. \quad (\text{E.2})$$

Appendix F

Network synthesis

F.1 Important time functions and their Laplace transforms

$f(t)$	$F(s)$	$f(t)$	$F(s)$
$\delta(t)$	1	$e^{s_0 t}$	$\frac{1}{s - s_0}$
$\Theta(t)$	$\frac{1}{s}$	$\frac{t^{n-1}}{(n-1)!} e^{s_0 t}$	$\frac{1}{(s - s_0)^n}$
$\frac{d^n}{dt^n} \delta(t)$	s^n	$\sin \omega t$	$\frac{\omega}{s^2 + \omega^2}$
$\frac{t^{n-1}}{(n-1)!}$	$\frac{1}{s^n}$	$\cos \omega t$	$\frac{s}{s^2 + \omega^2}$

Table F.1: Important time functions and their Laplace transforms. $\delta(t)$ denotes the Dirac delta function, $\Theta(t)$ the Heaviside function.

F.2 Construction of networks

Several methods exist to construct an actual network out of a given transfer function (or a set of transfer functions, respectively). We want to give a rough outline about a common approach which is used in modified form in a number of methods and can be used for two terminal networks as well as four terminal networks. By iteratively eliminating poles, the order of the transfer function is reduced and the transfer function can finally be written as a sum of partial fractions, where each fraction can individually be implemented in a known way. Consider a RC two pole, whose transfer function can always be written in the form [74]

$$Z(s) = \frac{U(s)}{I(s)} = \frac{r_0}{s} + \sum_{i=1}^n \frac{r_i}{s + s_i} + r_\infty \quad (\text{F.1})$$

with $r_0, r_i, r_\infty \geq 0, s_i > 0$. r_i is the residue at the pole s_i . Each individual term in (F.1) can be identified with an elementary RC circuit in the following way: as we wrote down the transfer function in resistive form (voltage in the nominator, current in the denominator), the

description of passive elements is given by their complex impedance, i.e. frequency f replaced by the complex frequency s ,

$$\begin{aligned} r_\infty &\hat{=} R && \text{corresponds to a resistor with } R = r_\infty, \\ \frac{r_0}{s} &\hat{=} \frac{1}{sC} && \text{corresponds to a capacitor with } C = \frac{1}{r_0}, \\ \frac{r_i}{s + s_i} &\hat{=} \frac{1}{sC + \frac{1}{R}} && \text{parallel connection of resistor with } R = \frac{r_i}{s_i} \text{ and capacitor with } C = \frac{1}{r_i}. \end{aligned} \quad (\text{F.2})$$

In the same way correspond terms of type $Z(s) = r \cdot s$ (not in (F.1)) to an inductor with inductance $L = r$.

As example, let's consider an explicit transfer function (taken from [74])

$$Z(s) = \frac{s^2 + 6s + 8}{s^2 + 4s + 3}. \quad (\text{F.3})$$

We find a pole at $s_1 = -1$ with residue $r_1 = 1.5$ and decompose $Z(s)$ into a partial fraction and the rest,

$$Z(s) = \frac{1.5}{s + 1} + Z'(s), \quad (\text{F.4})$$

$$Z'(s) = \frac{s^2 + 4.5s + 3.5}{s^2 + 4s + 3}. \quad (\text{F.5})$$

$Z'(s)$ has a pole at $s_2 = -3$ with residue $r_2 = 0.5$ and we arrive at

$$Z(s) = \frac{1.5}{s + 1} + \frac{0.5}{s + 3} + Z''(s), \quad (\text{F.6})$$

$$Z''(s) = 1. \quad (\text{F.7})$$

(F.3) can be written as sum of three partial fractions, one corresponding to a resistor, the other two giving each a parallel circuit of a resistor and a capacitance, according to (F.2).

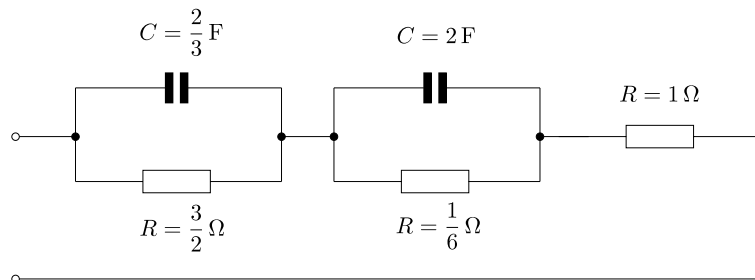


Figure F.1: Realization of a RC-filter by iterative pole elimination. Each of the three blocks (the resistor as well as the two parallel circuits) corresponds to a partial fraction in the resistive transfer function. The structure of the circuit is governed by the location of the poles, whereas the magnitude of the resistances and capacitances is given by the residue.

Taking into account that we deal with a transfer function in resistive form, this sum corresponds to a serial connection of these three blocks. We end up with the circuit shown in figure F.1.

However, instead of eliminating poles from $Z(s)$, we could have followed the same procedure for $Y(s) = \frac{1}{Z(s)}$, iteratively eliminating zeros from $Z(s)$. The result would have been an equivalent parallel circuit of serial connections instead of a serial circuit of parallel connections.

Moreover, as we can deduce from the particular form in (F.1), the poles of a RC two pole transfer function are located on the negative real axis. In contrast, the poles of a LC two pole function sit on the imaginary axis, whereas poles of LCR-filters can exist somewhere in the left halfplane.

Construction of four poles follows the same scheme. The four pole matrix $Z_{ik}(s)$, as given in (6.13) gets –by iterative elimination of poles (zeros, respectively)– decomposed into matrices with known implementation (Fig. F.2). A common algorithm is the method of Gewertz. As for two poles, elimination of a pole on the negative real axis yields a RC-filter, a pair of complex conjugate poles yields a LCR-filter.

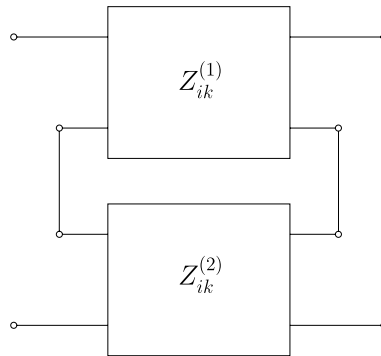


Figure F.2: Serial connection of two four-poles. The resulting set of transfer functions $Z_{ik}(s)$ is the sum of the individual sets of transfer functions, $Z_{ik}(s) = Z_{ik}^{(1)}(s) + Z_{ik}^{(2)}(s)$.

Appendix G

Publication

The attached paper has been submitted to Physical Review Letters and is available online, [quant-ph/0504202](https://arxiv.org/abs/quant-ph/0504202); the ASC (*Arnold Sommerfeld Center for Theoretical Physics*) preprint number is LMU-ASC 38/05.

Optimal Control of Coupled Josephson Qubits

A. Spörl, T. Schulte-Herbrüggen,* and S.J. Glaser

Department of Chemistry, Technische Universität München, Lichtenbergstrasse 4, 85747 Garching, Germany.

V. Bergholm

Materials Physics Laboratory, POB 2200 (Technical Physics) FIN-02015 HUT, Helsinki University of Technology, Finland.

M.J. Storcz, J. Ferber, and F.K. Wilhelm†

Physics Department, ASC, and CeNS, Ludwig-Maximilians-Universität, Theresienstr. 37, 80333 Munich, Germany.

(Dated: July 14, 2005)

This paper is dedicated to the memory of Martti Salomaa.

Quantum optimal control is applied to two and three coupled Josephson charge qubits. It is shown that by using shaped pulses a CNOT gate can be obtained with a trace fidelity $> 1 - 10^{-9}$ for the two qubits. Even when including higher charge states, the leakage is below 1%, although the pulses are non adiabatic. The controls are five times faster than the pioneering experiment (*Nature* **425**, 941 (2003)) for otherwise identical parameters – *i.e.* a progress towards the error-correction threshold by a factor of 100. The controls have palindromic smooth time courses representable by superpositions of few harmonics. We outline schemes to generate these shaped pulses. The approach generalises to larger systems, as shown by realising a TOFFOLI gate in three linearly coupled charge qubits 13 times faster than a circuit of nine CNOTs of above experimental work. In view of the next generation of fast pulse-shape generators, the method is designed to find wide application in quantum control of systems with finite degrees of freedom whose dynamics are Lie-algebraically closed.

PACS numbers: 85.25.Cp, 82.65.Jn, 03.67.Lx, 85.35.Gv

Regarding Hamiltonian simulation and quantum computation recent years have seen an increasing array of quantum systems that can be coherently controlled. Next to natural microscopic quantum systems, a particular attractive candidate for *scalable* setups are superconducting devices based on Josephson junctions [1–3]. Due to the ubiquitous bath degrees of freedom in the solid-state environment, the quantum coherence time remains limited, even in light of recent progress [4, 5] approaching theoretical bounds. Therefore it is a challenge to generate the gates fast and accurately enough to meet the error correction threshold. Concomitantly, progress has been made in applying optimal control techniques to steer quantum systems [6] in a robust, relaxation-minimising [7] or timeoptimal way [8, 9]. Spin systems are a particularly powerful paradigm of quantum systems [10]: under mild conditions they are fully controllable, *i.e.*, local and universal quantum gates can be implemented. In N spins- $\frac{1}{2}$ it suffices that (i) all spins can be addressed selectively by *rf*-pulses and (ii) that the spins form an arbitrary connected graph of weak coupling interactions. The optimal control techniques of spin systems can be extended to pseudo-spin systems, such as charge or flux states in superconducting setups, provided their Hamiltonian dynamics can be expressed to sufficient accuracy within a closed Lie algebra, *e.g.*, $\mathfrak{su}(2^N)$ in a system of N qubits.

As a practically relevant and illustrative example, we consider two capacitively coupled charge qubits controlled by DC pulses as in Ref. [1]. The infinite-dimensional Hilbert space of charge states in the device

can be mapped to its low-energy part defined by zero or one excess charge on the respective islands [2]. Identifying these charges as pseudo-spins, the Hamiltonian can be written as $H_{\text{tot}} = H_{\text{drift}} + H_{\text{control}}$, where the drift or static part reads (for constants see caption to Fig. 1)

$$\begin{aligned} H_{\text{drift}} = & - \left(\frac{E_m}{4} + \frac{E_{c1}}{2} \right) (\sigma_z^{(1)} \otimes \mathbf{1}) - \frac{E_{J1}}{2} (\sigma_x^{(1)} \otimes \mathbf{1}) \\ & - \left(\frac{E_m}{4} + \frac{E_{c2}}{2} \right) (\mathbf{1} \otimes \sigma_z^{(2)}) - \frac{E_{J2}}{2} (\mathbf{1} \otimes \sigma_x^{(2)}) \\ & + \frac{E_m}{4} (\sigma_z^{(1)} \otimes \sigma_z^{(2)}) \quad , \end{aligned} \quad (1)$$

while the controls can be cast into

$$\begin{aligned} H_{\text{control}} = & \left(\frac{E_m}{2} n_{g2} + E_{c1} n_{g1} \right) (\sigma_z^{(1)} \otimes \mathbf{1}) \\ & + \left(\frac{E_m}{2} n_{g1} + E_{c2} n_{g2} \right) (\mathbf{1} \otimes \sigma_z^{(2)}) \quad . \end{aligned} \quad (2)$$

Note that the Pauli matrices involved constitute a minimal generating set of the Lie algebra $\mathfrak{su}(4)$; hence the system is fully controllable. The control amplitudes $n_{g\nu}$, $\nu = 1, 2$ are gate charges controlled by external voltages via $n_{g\nu} = V_{g\nu} C_{g\nu} / 2e$. They are taken to be piecewise constant in each time interval t_k . This pseudo-spin Hamiltonian motivated by Ref. [1] also applies to other systems such as double quantum dots [11] and Josephson flux qubits [12], although in the latter case the controls are typically *rf*-pulses.

In a time interval t_k the system thus evolves under $H_{\text{tot}}^{(k)} = H_{\text{drift}} + H_{\text{control}}^{(k)}$. The task is to find a sequence of

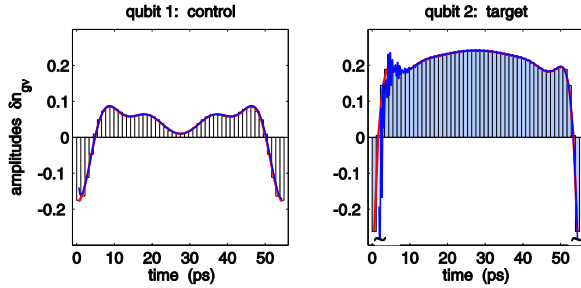


FIG. 1: (Colour online) Fastest gate charge controls obtained for realising a CNOT-gate on two coupled charge qubits (left part: control qubit, right part: working qubit). The total gate charges for the qubits are $n_{g\nu} = n_{g\nu}^0 + \delta n_{g\nu}$ with $\nu = 1, 2$. Here, $n_{g1}^0 = 0.24$, $n_{g2}^0 = 0.26$ and the qubit energies $E_{c1}/h = 140.2$ GHz, $E_{c2}/h = 162.2$ GHz, $E_{J1}/h = 10.9$ GHz, $E_{J2}/h = 9.9$ GHz, and $E_m/h = 23.0$ GHz were taken from the experimental values in [1]. The 50 piecewise constant controls are shown as bars (uniform width $\Delta = t_k = 1.1$ ps); the trace fidelity is $\frac{1}{2^N} |\text{tr}\{U_{\text{target}}^\dagger U_T\}| > 1 - 10^{-9}$. Red lines give the analytic curves in Eqn. 3; the blue ones superimposed show a pulse synthesised by an LCR-filter (see below and Fig. 3).

control amplitudes for the intervals $t_1, t_2, \dots, t_k, \dots, t_M$ such as to maximise a quality function, here the overlap with the desired quantum gate or element of an algorithm U_{target} . Moreover, for the decomposition of $U_T = e^{-it_M H^M} e^{-it_{M-1} H^{M-1}} \dots e^{-it_k H^k} \dots e^{-it_1 H^1}$ into available controls $\{H_\nu^{(k)}\}$ to be timeoptimal, $T := \sum_{k=1}^M t_k$ has to be minimal. The gate fidelity is unity, if $\|U_T - U_{\text{target}}\|_2^2 = 0 = \|U_T\|_2^2 + \|U_{\text{target}}\|_2^2 - 2\text{Re tr}\{U_{\text{target}}^\dagger U_T\}$. Maximising $\text{Re tr}\{U_{\text{target}}^\dagger U_T\}$ can be solved by optimal control: set $h(U(t_k)) := \text{Re tr}\{\lambda^\dagger(t_k)(-i(H_d + \sum u_\nu H_\nu))U(t_k)\}$ with the Lagrange-type adjoint system $\lambda(t)$ following the equation of motion $\dot{\lambda}(t) = -i(H_d + \sum u_\nu H_\nu)\lambda(t)$. Pontryagin's maximum principle requires $\partial h/\partial u_\nu \equiv \text{Re tr}\{\lambda^\dagger(-iH_\nu)U\} = 0$ thus allowing to implement a gradient-flow based recursion. For the amplitude of the ν^{th} control in iteration $r + 1$ at time interval t_k one finds with ε as a suitably chosen step size $n_{g\nu}^{(r+1)}(t_k) = n_{g\nu}^{(r)}(t_k) + \varepsilon \frac{\partial h^{(r)}(t_k)}{\partial n_{g\nu}^{(r)}(t_k)}$ as explained in more detail in Refs. [13, 14]. T is the shortest fixed final time allowing for a given fidelity to be obtained numerically.

Throughout the work, we take the parameters from the experiment [1]. Fig. 1 shows the fastest decompositions obtained by numerical optimal control for the CNOT gate into evolutions under available controls (Eqns. 1 and 2). In contrast to the 255 ps in Ref. [1], $T = 55$ ps suffice to get $\|U_T - U_{\text{target}}\|_2 = 5.3464 \times 10^{-5}$ corresponding to a trace fidelity of $\frac{1}{2^N} |\text{tr}\{U_{\text{target}}^\dagger U_T\}| > 1 - 10^{-9}$.

The supplementary material illustrates how the sequence of controls (Fig. 1) acts on specific input states by representing the quantum evolution on local Bloch

spheres complemented by showing the coupling evolution in the Weyl chamber. These pictures trigger physical insight: for a CNOT, the duration $T = 55$ ps has to accommodate at least a $\frac{\pi}{2}$ rotation under the coupling Hamiltonian ($\frac{1}{2}\sigma_z \otimes \sigma_z$) lasting 21.7 ps concomitant to two $\frac{\pi}{2}$ x -rotations under the drift component ($\frac{1}{2}\sigma_x^{(2)}$) each requiring 25.3 ps. This is in contrast to NMR, where the coupling interactions are some 100 times slower than the local ones, so timeoptimal controls can be envisaged as Riemannian geodesics in the symmetric space $G/K = SU(4)/SU(2)^{\otimes 2}$ [8]. However, in our charge qubit system, the time scales of local and non-local interactions are comparable, and the local drifts in K generated by σ_x are even time-limiting, while phase shifts generated by σ_z via the gate charge are fast (*cf.* Eqns. 1-2). Assuming in a limiting simplification that *two* $\frac{\pi}{2}$ x -pulses are required, the total length cannot be shorter than 50.6 ps. A sigmoidal phase distortion from a geodesic state inversion is cheap timewise. While the duration of $T = 55$ ps of our controls is close to the simplifying infimum of 50.6 ps, the controls in Ref. [1] last 255 ps; they entail several closed great circles on the Bloch sphere and are far from geodesic (details in the supplement).

Note that the time course of controls in charge qubits turns out palindromic (Fig. 1). Self-inverse gates ($U_{\text{gate}}^2 = \mathbf{1}$) relate to the more general time-and-phase-reversal symmetry (TPR) observed in the control of spin systems [15]: for example, any sequence $e^{-it_x \sigma_x} e^{-it_y \sigma_y} e^{-it_z \sigma_z}$ is inverted by transposition concomitant to time reversal $t_\nu \mapsto -t_\nu$ and $\sigma_y \mapsto -\sigma_y$. Since the Hamiltonians in Eqns. 1-2 are real and symmetric, they will give the same propagator, no matter whether read forward or backward.

The pulses are not very complicated, as the time course of the controls on either qubit ($\nu = 1, 2$) can be written with high accuracy as a sum of 6(7) harmonic functions (coefficients in Tab. 1 of the supplement)

$$n_{g\nu}(t) = \sum_{j=0}^{5(6)} a_\nu(j) \cos\left(2\pi\omega_\nu(j)\frac{t}{T} + \phi_\nu(j)\right). \quad (3)$$

The limited bandwidth allows to maintain high fidelity even if leakage levels formed from higher charge states of the qubit system are taken into account: we now explicitly apply the pulses to the extended system obtained by mapping the full Hamiltonian [1] to the subspaces of $-1, \dots, 2$ extra charges per island. The two-qubit CNOT gate is thus embedded into the group $SU(16)$, still the full propagator generated by the above controls projects onto the CNOT gate giving a trace fidelity > 0.99 . Even the time courses starting with any of the four canonical two-qubit basis vectors hardly ever leave the state space of the working qubits: at no time do the projections onto the leakage space exceed 0.6%. Clearly, optimisation including explicit leakage levels would improve the quality even further as in other systems [16].

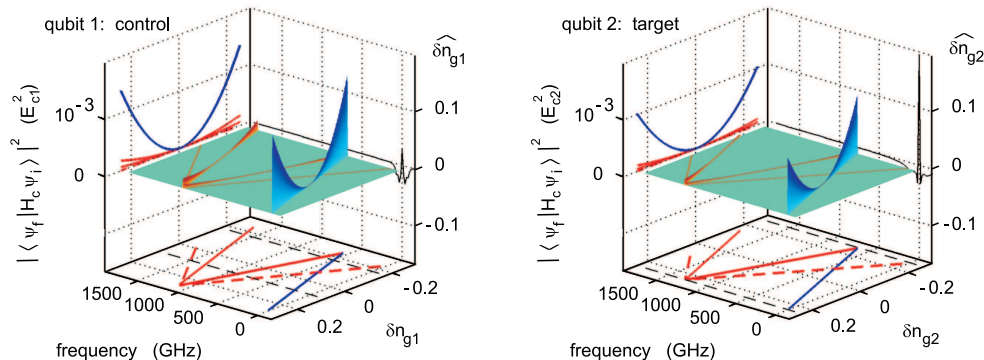


FIG. 2: (Colour online) Spectroscopic explanation of the high quality of the control sequences of Fig. 1: the spectral overlap of the Fourier-transforms (right walls) of the controls of Fig. 1 with the energy differences corresponding to the one-charge transitions into leakage levels (solid lines on the surface) is small at gate charges in the working range (within black dashed lines). In the 3D representation, intensities at allowed (solid lines) *vs* forbidden transitions (broken lines) into leakage levels are given in terms of the transition-matrix elements (normalised by the charging energies E_{c1}^2 , E_{c2}^2) with the control Hamiltonian of Eqn. 2 expressed as $H_c(\delta n_{g\nu})$ in $|\langle \Psi_f | H_c | \Psi_i \rangle|^2$: the working transitions (blue) are far more probable than the allowed ones into leakage levels (red) that have no overlap with the excitation bandwidth of the pulses; forbidden ones are extremely weak.

In simplified terms, the high quality can be understood by relating the limited bandwidth to the transitions between the eigenstates of the local parts of H_{drift} in Eqn. 1: while *one-charge* transitions to leakage levels like $|-1\rangle \leftrightarrow |0\rangle$ and $|2\rangle \leftrightarrow |1\rangle$ are allowed, *two-charge* transitions like $|-1\rangle \leftrightarrow |1\rangle$ and $|2\rangle \leftrightarrow |0\rangle$ are forbidden in terms of the transition-matrix elements $|\langle \Psi_{\text{final}} | H_{\text{control}} | \Psi_{\text{initial}} \rangle|^2$ as can be seen in Fig. 2. Note the charge control on gate 2 in Fig. 1 is around $\delta n_{g2} = 0.2$ thus driving the working transition $|0\rangle \leftrightarrow |1\rangle$, while the ‘spectral overlap’ of the Fourier-transform of the time course in both controls with energy differences corresponding to one-charge leakage transitions in Fig. 2 is small. Hence simple spectroscopic arguments underpin the high fidelity.

The actual pulse shape generation is a challenging but possible task. Note that the minimal length of the pulse is given by the coupling strength. In the pertinent time scale, however, there are no commercially available devices for generating arbitrary wave forms. Yet, high-end pulse generators [17, 18] or ultrafast classical Josephson electronics [19] are close to the necessary specifications.

As a proof of principle, it is important to note how to generate these pulses experimentally, which can readily be exemplified using the well-established technique of shaping in Laplace space: we start with an input current pulse $I_{\text{in}}(t)$ *shorter* than the desired one of a shape which is arbitrary as long as it contains enough spectral weight at the harmonics necessary for the desired pulse. Such pulses are easily generated optically or electrically [18]. This pulse is sent through an appropriately designed discrete electrical four-pole with transfer function Z_{12} . We have carried out this idea for a rectangular pulse of length $\tau_r = 1.1\text{ps}$ as an input and our two gate pulses as outputs. We have developed a transfer function in Laplace

space $Z_{12}(s)$ by fitting $V_g(s) = Z_{12}(s)I_{\text{in}}(s)$, see Fig. 3. Owing to causality, the poles of Z_{12} are either on the negative real axis or in conjugate pairs of poles on the left half plane. Each conjugate pair corresponds to an LCR-filter stage, whereas each real pole corresponds to an RC lowpass-filter [20]. With 8 LCR filters and two low-pass filters the pulses are very close to the desired ones, see Fig. 1, and a trace fidelity of 94 % can be achieved for the entire CNOT. Clearly, the quality could be further improved with more refined technology. This approach can also accommodate the generally frequency-dependent transfer function from the generator to the sample as shown in the Supplementary Material.

Note that our controls are fairly robust with regard to $\pm 5\%$ variation of the tunneling frequencies $E_{J_{1,2}}$ and the coupling term E_m as well as to Gaussian noise on the

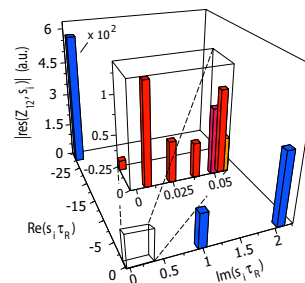


FIG. 3: (Colour online) Filter characteristic for shaping the pulse on the working gate. The bars show the poles s_i of the transfer function in the Laplace plane. Poles outside the negative imaginary axis also lead to the complex conjugate pole and can be implemented by an LCR-Filter. The height of the bar gives the modulus of the residue in this pole.

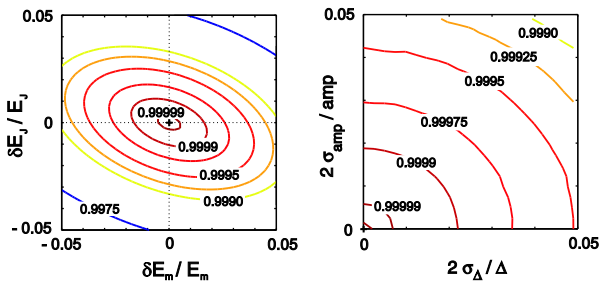


FIG. 4: (Colour online) Left: Trace fidelities resulting from the controls of Fig. 1 when the parameters E_m and E_J in Eqns. 1-2 vary by $\pm 5\%$. In this range, the quality profile can be fitted by a tilted 2D Gaussian (parameters in Supplement). Right: Fidelities under Gaussian noise on control amplitudes and time intervals parameterised by the standard deviations $2\sigma_{\Delta}/\Delta$ and $2\sigma_{\text{amp}}/\text{amp}$ ranging from 0 to 5%. (As in Fig. 1, $\Delta := t_k$; $\text{amp} := \delta n_{g\nu}$ with $\nu = 1, 2$.) Each data point is an average of 25'000 Monte-Carlo simulations.

control amplitudes and time-intervals as shown in Fig. 4.

Likewise, in a system of three linearly coupled charge qubits, we realised the TOFFOLI gate by experimentally available controls (Fig. 5), where the speed-up against a circuit of 9 CNOTs is by a factor of 2.8 with our CNOTs and by 13 with the CNOTs of Ref. [1]. Due to the comparatively strong qubit-qubit interactions in multiqubit setups, a direct generation of three-qubit gates is much faster than its composition by elementary universal gates. This also holds when developing simple algorithms [21] on superconducting qubit setups: a minimisation algorithm for searching control amplitudes in coupled Cooper pair boxes was applied in [22], where the optimisation was restricted to only very few values. In Ref. [23], an *rf*-pulse sequence for a CNOT with fixed couplings was introduced, which, however, is much longer and uses more of the available decoherence time.

In conclusion, we have shown how to provide optimal-control based fast high-fidelity quantum logic gates in pseudospin systems such as superconducting charge qubits, where the progress towards the error-correction threshold is by a factor of 100 (details in the Supplement). The simplicity of the pulse shape results in low bandwidth and remarkably low leakage to higher states, although the pulses are non-adiabatic. With the setup necessary to generate optimised pulses being of modest complexity, the approach will find wide application, in particular for the next generation of fast pulse-shaping devices. We expect the decoherence time scales dominated by $1/f$ contributions to T_2 will not change largely under the pulses, so time optimal controls provide a significant step towards the accuracy threshold for quantum computing, even if the optimisation of decoherence times reaches its intrinsic limits.

We are indebted to N. Khaneja for continuous stimulating scientific exchange. We thank M. Mariantoni

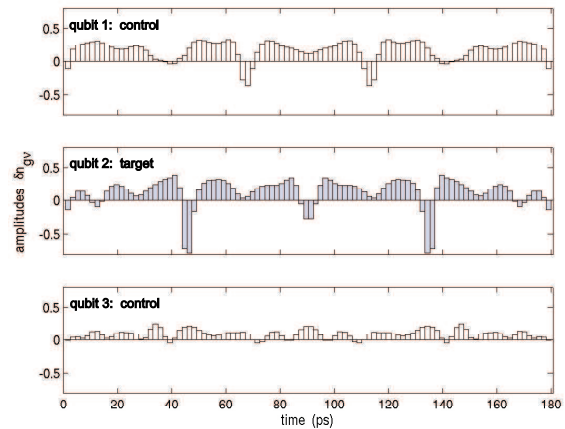


FIG. 5: Fastest gate charge controls obtained for realising a TOFFOLI gate on a linear chain of charge qubits coupled by nearest-neighbour interactions with a trace fidelity of $\frac{1}{2^N} |\text{tr}\{U_{\text{target}}^\dagger U_T\}| > 1 - 10^{-5}$. Parameters: $E_{c1}/h = 140.2$ GHz, $E_{c2}/h = 120.9$ GHz, $E_{c3}/h = 184.3$ GHz, $E_{J1}/h = 10.9$ GHz, $E_{J2}/h = 9.9$ GHz, $E_{J3}/h = 9.4$ GHz, $E_{m1,2}/h = 23$ GHz, $n_{g1}^0 = 0.24$, $n_{g2}^0 = 0.26$, $n_{g3}^0 = 0.28$.

for discussing experimental issues, as well as Y. Nakamura and the NEC group, J.M. Martinis, A. Ustinov, L.C.L. Hollenberg, T. Cubitt, and D. van der Weide. This work was supported by DFG in SPP 1078 (Gl 203/4-2) and SFB 631, by the Finnish Cultural Foundation, by ARDA and by NSA (ARO contract P-43385-PH-QC).

* Electronic address: tosh@ch.tum.de

† Electronic address: frank.wilhelm@physik.lmu.de

- [1] T. Yamamoto, Y. A. Pashkin, O. Astafiev, Y. Nakamura, and J. S. Tsai, *Nature (London)* **425**, 941 (2003).
- [2] Y. Makhlin, G. Schön, and A. Shnirman, *Rev. Mod. Phys.* **73**, 357 (2001).
- [3] R. McDermott, R. W. Simmonds, M. Steffen, K. B. Cooper, K. Cicak, K. D. Osborn, S. Oh, D. P. Pappas, and J. M. Martinis, *Science* **307**, 1299 (2005).
- [4] P. Bertet, I. Chiorescu, G. Burkard, K. Semba, C. Harmans, D. DiVincenzo, and J. Mooij, *cond-mat/0412485*.
- [5] O. Astafiev, Y. A. Pashkin, Y. Nakamura, T. Yamamoto, and J. S. Tsai, *Phys. Rev. Lett.* **93**, 267007 (2004).
- [6] A. G. Butkovskiy and Y. I. Samoilenko, *Control of Quantum-Mechanical Processes and Systems* (Kluwer, Dordrecht, 1990).
- [7] N. Khaneja, B. Luy, and S. J. Glaser, *Proc. Natl. Acad. Sci. USA* **100**, 13162 (2003).
- [8] N. Khaneja, R. W. Brockett, and S. J. Glaser, *Phys. Rev. A* **63**, 032308 (2001).
- [9] N. Khaneja, S. J. Glaser, and R. W. Brockett, *Phys. Rev. A* **65**, 032301 (2001).
- [10] S. J. Glaser, T. Schulte-Herbrüggen, M. Sieveking, O. Schedletsky, N. C. Nielsen, O. W. Sørensen, and C. Griesinger, *Science* **280**, 421 (1998).

- [11] T. Hayashi, T. Fujisawa, H. Cheong, Y. Yeong, and Y. Hirayama, *Phys. Rev. Lett.* **91**, 226804 (2003).
- [12] J. Majer, F. Paauw, A. ter Haar, C. Harmans, and J. Mooij, *Phys. Rev. Lett.* **94**, 090501 (2005).
- [13] N. Khaneja, T. Reiss, C. Kehlet, T. Schulte-Herbrüggen, and S. J. Glaser, *J. Magn. Reson.* **172**, 296 (2005).
- [14] T. Schulte-Herbrüggen, A. Spörl, N. Khaneja, and S. J. Glaser, [quant-ph/0502104](#).
- [15] C. Griesinger, C. Gemperle, O. W. Sørensen, and R. R. Ernst, *Molec. Phys.* **62**, 295 (1987).
- [16] S. Sklarz and D. Tannor, [quant-ph/0404081](#).
- [17] H. Kim, A. Kozrev, S. Ho, and D. van der Weide, *proc. IEEE Microwave Symp.* 2005, in press.
- [18] H. Qin, R. Blick, D. van der Weide, and K. Eberl, *Physica E* **13**, 109 (2002).
- [19] D. Brock, *Int. J. High Sp. El. Sys.* **11**, 307 (2001).
- [20] W. Rupprecht, *Netzwerksynthese* (Springer, Berlin, 1972).
- [21] J. Vartiainen, A. Niskanen, M. Nakahara, and M. Salomaa, *Int. J. Quant. Inf.* **2**, 1 (2004).
- [22] A. Niskanen, J. Vartiainen, and M. Salomaa, *Phys. Rev. Lett.* **90**, 197901 (2003).
- [23] C. Rigetti, A. Blais, and M. Devoret, *Phys. Rev. Lett.* **94**, 240502 (2005).

List of Figures

1.1	Equivalent circuit diagram of a Josephson junction	5
1.2	Circuit diagram of a three-junction flux qubit	7
1.3	SEM picture of a three-junction flux qubit	7
1.4	Energy landscape of a three junction qubit	8
1.5	Energy anticrossing for the flux qubit	9
2.1	Three qubits, enclosed by a common SQUID-loop	11
2.2	The design of the flux qubit triangle	16
2.3	Readout design with three SQUIDs	20
3.1	Eigenenergies vs. ϵ for several coupling strengths	23
4.1	Level diagram for the dressed states	35
5.1	3-tangle and GHZ witness for $ E_3\rangle$	41
5.2	3-tangle and Bell inequality for $ E_3\rangle$	41
5.3	3-tangle and GHZ witnesses for $ E_2\rangle$	42
5.4	3-tangle and Bell inequality for $ E_2\rangle$	42
5.5	3-tangle and W witness for $ \psi_{\max}^L\rangle$	43
5.6	3-tangle and Bell inequality for $ \psi_{\max}^L\rangle$	43
5.7	Expectation value of GHZ witness for several measurement fidelities for $ E_3\rangle$	47
5.8	Expectation value of Bell operator for several measurement fidelities for $ E_3\rangle$	47
5.9	Expectation value of GHZ witness for several measurement fidelities for $ E_2\rangle$	48
5.10	Expectation value of Bell operator for several measurement fidelities for $ E_2\rangle$	48
5.11	Expectation value of W witness for several measurement fidelities for $ \psi_{\max}^L\rangle$.	48
5.12	Expectation value of Bell operator for several measurement fidelities for $ \psi_{\max}^L\rangle$	49
6.1	Block diagram of a LTI system	53
6.2	Block diagram of a two terminal network	54
6.3	Block diagram of four terminal network	55
6.4	Pulses shaped by filter networks of varying complexity	58
6.5	Time course of the desired output and the pulses shaped by the filter networks	58
6.6	Pole configuration of the networks shaping the pulses and the associate residue	59
C.1	Amplitudes of the eigenstates vs. ϵ for $C = 0$	70
C.2	Amplitudes of the eigenstates vs. ϵ for $C = 0.2\Delta$	71
C.3	Amplitudes of the eigenstates vs. ϵ for $C = 1.4\Delta$	72

F.1	Realization of a RC-filter by iterative pole elimination	78
F.2	Serial connection of two four-poles	79

List of Tables

2.1	Mutual inductances for the common-loop-design	15
2.2	Mutual geometrical inductances for the qubit triangle	19
5.1	Local decomposition of entanglement witnesses	44
5.2	Explicit form of Bell operator \hat{M}_W for W state	46
5.3	Minimal detector fidelities for entanglement detection	49
F.1	Important time functions and the corresponding spectra	77

Bibliography

- [1] D. Deutsch, *Quantum Theory, the Church-Turing Principle and the Universal Quantum Computer*, Proc. Roy. Soc. Lond. A **400**, 97 (1985).
- [2] P. W. Shor, in *Proc. 35th Annual Symposium on the Foundations of Computer Science*, edited by S. Goldwasser (IEEE Computer Society Press, 1994), pp. 124–134.
- [3] C. Bennett and D. P. DiVincenzo, *Quantum Computing—Towards an engineering era?*, Nature **377**, 389 (1995).
- [4] L. K. Grover, *Quantum Mechanics Helps in Searching for a Needle in a Haystack*, Phys. Rev. Lett. **79**, 325 (1997).
- [5] D. P. DiVincenzo, *Quantum Computation*, Science **270**, 255 (1995).
- [6] F. Schmidt-Kaler, H. Häffner, M. Riebe, S. Gulde, G. P. T. Lancaster, T. Deuschle, C. Becher, C. F. Roos, J. Eschner, and R. Blatt, *Realization of the Cirac-Zoller controlled-NOT quantum gate*, Nature **422**, 408 (2003).
- [7] E. Knill, R. Laflamme, and G. J. Milburn, *A scheme for efficient quantum computation with linear optics*, Nature **409**, 46 (2001).
- [8] L. M. K. Vandersypen and I. L. Chuang, *Nmr techniques for quantum control and computation*, Rev. Mod. Phys. **76**, 1037 (2004).
- [9] S. J. Glaser, T. Schulte-Herbrüggen, M. Sieveking, O. Schedletsky, N. C. Nielsen, O. W. Sørensen, and C. Griesinger, *Unitary Control in Quantum Ensembles, Maximising Signal Intensity in Coherent Spectroscopy*, Science **280**, 421 (1998).
- [10] S. J. Glaser, *NMR Quantum Computing*, Angew. Chem. Int. Ed. **40**, 147 (2001).
- [11] L. M. K. Vandersypen, M. Steffen, G. Breyta, C. S. Yannoni, M. H. Sherwood, and I. L. Chuang, *Experimental realization of Shor’s quantum factoring algorithm using nuclear magnetic resonance*, Nature **414**, 883 (2001).
- [12] Y. Makhlin, G. Schön, and A. Shnirman, *Quantum-state engineering with Josephson-junction devices*, Rev. Mod. Phys. **73**, 357 (2001).
- [13] V. Cerletti, W. A. Coish, O. Gywat, and D. Loss, *Recipes for spin-based quantum computing*, Nanotechnology **16**, R27 (2005).

- [14] C. H. van der Wal, A. ter Haar, F. Wilhelm, R. Schouten, C. Harmans, T. Orlando, S. Lloyd, and J. Mooij, *Quantum Superposition of Macroscopic Persistent-Current States*, Science **290**, 773 (2000).
- [15] I. Chiorescu, Y. Nakamura, C. Harmans, and J. Mooij, *Coherent Quantum Dynamics of a Superconducting Flux Qubit*, Science **299**, 1869 (2003).
- [16] A. C. J. ter Haar, PhD thesis, TU Delft (2005).
- [17] Y. A. Pashkin, T. Yamamoto, O. Astafiev, Y. Nakamura, D. V. Averin, and J. S. Tsai, *Quantum oscillations in two coupled charge qubits*, Nature **421**, 823 (2003).
- [18] T. Yamamoto, Y. A. Pashkin, O. Astafiev, Y. Nakamura, and J. S. Tsai, *Demonstration of conditional gate operation using superconducting charge qubits*, Nature **425**, 941 (2003).
- [19] M. Tinkham, *Introduction to Superconductivity* (McGraw-Hill, 1996).
- [20] J. E. Mooij, T. P. Orlando, L. Levitov, L. Tian, C. H. van der Wal, and S. Lloyd, *Josephson Persistent-Current Qubit*, Science **285**, 1036 (1999).
- [21] C. H. van der Wal, PhD thesis, TU Delft (2001).
- [22] T. P. Orlando, J. E. Mooij, L. Tian, C. H. van der Wal, L. S. Levitov, S. Lloyd, and J. J. Mazo, *Superconducting persistent-current qubit*, Phys. Rev. B **60**, 15398 (1999).
- [23] P. Bertet, I. Chiorescu, G. Burkard, K. Semba, C. Harmans, D. DiVincenzo, and J. Mooij, *Relaxation and dephasing in a flux qubit*, cond-mat/0412485 (2004).
- [24] A. J. Leggett, S. Chakravarty, A. T. Dorsey, M. P. A. Fisher, A. Garg, and W. Zwerger, *Dynamics of the dissipative two-state system*, Rev. Mod. Phys. **59**, 1 (1987).
- [25] B. L. T. Plourde, J. Zhang, K. B. Whaley, F. K. Wilhelm, T. L. Robertson, T. Hime, S. Linzen, P. A. Reichardt, C.-E. Wu, and J. Clarke¹, *Entangling flux qubits with a bipolar dynamic inductance*, PRB **70**, 140501 (2004).
- [26] J. Clarke and A. I. Braginski, *The SQUID Handbook, Vol.1 : Fundamentals and Technology of SQUIDS and SQUID Systems* (John Wiley & Sons Inc, 2004).
- [27] A. Wallraff, D. I. Schuster, A. Blais, L. Frunzio, J. Majer, M. H. Devoret, S. M. Girvin, and R. J. Schoelkopf, *Approaching Unit Visibility for Control of a Superconducting Qubit with Dispersive Readout*, Phys. Rev. Lett. **95**, 060501 (2005).
- [28] A. Lupascu, C. J. Verwijs, R. N. Schouten, C. J. P. Harmans, and J. E. Mooij, *Nondestructive Readout for a Superconducting Flux Qubit*, Phys. Rev. Lett. **93**, 177006 (2004).
- [29] A. Lupascu, C. J. P. Harmans, and J. E. Mooij, *Quantum state detection of a superconducting flux qubit using a dc-SQUID in the inductive mode*, Phys. Rev. B **71**, 184506 (2005).
- [30] J. David Jackson, *Klassische Elektrodynamik* (De Gruyter, 2002).
- [31] *Fasthenry*, URL <http://www.wrcad.com/ftp/pub/fasthenry-3.0wr.tar.gz>.

- [32] M. Grifoni and P. Hänggi, *Driven quantum tunneling*, Phys. Reports **304**, 229 (1998).
- [33] C. Cohen-Tannoudji, J. Dupont-Roc, and G. Grynberg, *Atom-Photon Interactions* (Wiley, 1998).
- [34] D. Walls and G. Milburn, *Quantum Optics* (Springer, 1994).
- [35] E. Schrödinger, Proc. Cambridge Philos. Soc **31**, 555 (1935).
- [36] S. Popescu and D. Rohrlich, in *Introduction to Quantum Computation and Information* (World Scientific, 1998).
- [37] C. H. Bennett, G. Brassard, C. Crépeau, R. Jozsa, A. Peres, and W. K. Wootters, *Teleporting an unknown quantum state via dual classical and Einstein-Podolsky-Rosen channels*, Phys. Rev. Lett. **70**, 1895 (1993).
- [38] M. Riebe, H. Häffner, C. F. Roos, W. Hänsel, J. Benhelm, G. P. T. Lancaster, T. W. Körber, C. Becher, F. Schmidt-Kaler, D. F. V. James, et al., *Deterministic quantum teleportation with atoms*, Nature **429**, 734 (2004).
- [39] A. Ekert, *Quantum Cryptography Based on Bell's Theorem*, Phys. Rev. Lett. **67**, 661 (1991).
- [40] A. Einstein, B. Podolsky, and N. Rosen, *Can Quantum-Mechanical Description of Reality Be Considered Complete?*, Phys. Rev. **41**, 777 (1935).
- [41] J. Bell, *On the Einstein-Podolsky-Rosen Paradox*, Physics **1**, 195 (1964).
- [42] S. J. Freedman and J. F. Clauser, *Experimental Test of Local Hidden-Variable Theories*, Phys. Rev. Lett. **28**, 938 (1972).
- [43] C. Bennett and D. P. DiVincenzo, *Experimental Test of Bell's Inequalities Using Time-Varying Analyzers*, Phys. Rev. Lett. **49**, 1804 (1982).
- [44] G. Weihs, T. Jennewein, C. Simon, H. Weinfurter, and A. Zeilinger, *Violation of Bell's Inequality under Strict Einstein Locality Conditions*, Phys. Rev. Lett. **81**, 5039 (1998).
- [45] M. A. Rowe, D. Kielpinsky, V. Meyer, C. A. Sacket, W. M. Itano, C. Monroe, and D. J. Wineland, *Experimental violation of a Bell's inequality with efficient detection*, Nature **409**, 791 (2001).
- [46] A. Peres, *Separability Criterion for Density Matrices*, Phys. Rev. Lett. **77**, 1413 (1996).
- [47] W. Dür, G. Vidal, and J. Cirac, *Three qubits can be entangled in two inequivalent ways*, Phys. Rev. A **62**, 062314 (2000).
- [48] I. C. M. A. Nielsen, *Quantum Computation and Quantum Information* (Cambridge University Press, 2000).
- [49] D. M. Greenberger, M. Horne, and A. Zeilinger, in *Bell's Theorem, Quantum Theory and Conceptions of the Universe* (Kluwer Academic, 1989).
- [50] V. Coffman, J. Kundu, and W. K. Wootters, *Distributed entanglement*, Phys. Rev. A **61**, 052306 (2000).

- [51] B. M. Terhal, *Bell inequalities and the separability criterion*, Phys. Lett. A **271**, 319 (2000).
- [52] M. Lewenstein, B. Kraus, J. I. Cirac, and P. Horodecki, *Optimization of entanglement witnesses*, Phys. Rev. A **62**, 052310 (2000).
- [53] J. Eisert, P. Hyllus, O. Gühne, and M. Curty, *Complete hierarchies of efficient approximations to problems in entanglement theory*, Phys. Rev. A **70**, 062317 (2004).
- [54] F. G. S. L. B. ao, *Quantifying entanglement with witness operators*, Phys. Rev. A **72**, 022310 (2005).
- [55] O. Gühne and P. Hyllus, *Investigating Three Qubit Entanglement With Local Measurements*, Int. J. Theor. Phys. **42**, 1001 (2003).
- [56] M. Bourennane, M. Eibl, C. Kurtsiefer, S. Gaertner, H. Weinfurter, O. Gühne, P. Hyllus, D. Bruß, M. Lewenstein, and A. Sanpera, *Experimental Detection of Multipartite Entanglement using Witness Operators*, Phys. Rev. Lett. **92**, 087902 (2004).
- [57] G. Tóth and O. Gühne, *Detecting Genuine Multipartite Entanglement with Two Local Measurements*, Phys. Rev. Lett. **94**, 060501 (2005).
- [58] A. Acín, D. Bruß, M. Lewenstein, and A. Sanpera, *Classification of Mixed Three-Qubit States*, Phys. Rev. Lett. **87**, 040401 (2001).
- [59] D. M. Greenberger, M. A. Horne, A. Shimony, and A. Zeilinger, *Bell's theorem without inequalities*, Am. J. Phys. **58**, 1131 (1990).
- [60] N. D. Mermin, *Quantum mysteries revisited*, Am. J. Phys. **58**, 731 (1990).
- [61] N. D. Mermin, *Extreme Quantum Entanglement in a Superposition of Macroscopically Distinct States*, Phys. Rev. Lett. **65**, 1838 (1990).
- [62] A. V. Belinskii and D. N. Klyshko, *Interference of light and Bell's theorem*, Phys. Usp. **36**, 653 (1993).
- [63] D. N. Klyshko, *The Bell and GHZ theorems: a possible three-photon interference experiment and the question of nonlocality*, Phys. Lett. A **172**, 399 (1993).
- [64] J. Endrejat and H. Büttner, *Characterization of entanglement of more than two qubits with Bell inequalities and global entanglement*, Phys. Rev. A **71**, 012305 (2005).
- [65] C. Emary and C. W. J. Beenakker, *Relation between entanglement measures and Bell inequalities for three qubits*, Phys. Rev. A **69**, 032317 (2004).
- [66] J. Endrejat (2005), priv. comm.
- [67] J. F. Clauser, M. A. Horne, A. Shimony, and R. A. Holt, *Proposed Experiment to Test Local Hidden-Variable Theories*, Phys. Rev. Lett. **23**, 880 (1969).
- [68] M. J. Storcz, PhD thesis, LMU München (2005).

- [69] I. Siddiqi, R. Vijay, F. Pierre, C.M.Wilson, M. Metcalfe, C. Rigetti, L. Frunzio, and M. H. Devoret, *RF-Driven Josephson Bifurcation Amplifier for Quantum Measurement*, Phys. Rev. Lett. **93**, 20702 (2004).
- [70] O. Astafiev, Y. A. Pashkin, T. Yamamoto, Y. Nakamura, and J. S. Tsai, *Single-shot measurement of the Josephson charge qubit*, Phys. Rev. B **69**, 180507 (2004).
- [71] N. Khaneja, T. Reiss, C. Kehlet, T. Schulte-Herbrüggen, and S. J. Glaser, *Optimal control of coupled spin dynamics: design of NMR pulse sequences by gradient ascent algorithms*, J. Magn. Reson. **172**, 296 (2005).
- [72] R. Fazio, G. M. Palma, and J. Siewert, *Fidelity and Leakage of Josephson Qubits*, Phys. Rev. Lett. **83**, 5385 (1999).
- [73] Ohm and Lüke, *Signalübertragung* (Springer, 2004).
- [74] W. Rupprecht, *Netzwerksynthese* (Springer, 1972).
- [75] B. Ferguson and X.-C. Zhang, *Materials for terahertz science and technology*, Nature Review Article **1**, 26 (2002).
- [76] A. Zewail, in *Nobel Lectures, Chemistry 1996-2000*, edited by I. Grenthe (World Scientific Publishing Co., 2003).
- [77] T. Fließbach, *Quantenmechanik* (Spektrum Verlag, 1995).
- [78] G. Vidal, *Entanglement monotones*, J. Mod. Opt. **47**, 355 (2000).
- [79] C. H. Bennett, S. Popescu, D. Rohrlich, J. A. Smolin, and A. V. Thapliyal, *Exact and asymptotic measures of multipartite pure-state entanglement*, Phys. Rev. A **63**, 012307 (2001).
- [80] C. H. Bennett, D. P. DiVincenzo, J. A. Smolin, and W. K. Wootters, *Mixed-state entanglement and quantum error correction*, Phys. Rev. Lett. **54**, 3824 (1996).
- [81] S. Hill and W. K. Wootters, *Entanglement of a Pair of Quantum Bits*, Phys. Rev. Lett. **78**, 5022 (1997).
- [82] W. K. Wootters, *Entanglement of Formation of an Arbitrary State of Two Qubits*, Phys. Rev. Lett. **80**, 2245 (1998).